Oil & Natural Gas Technology

DOE Award No.: DE-FE0024297

Quarterly Research Performance

Progress Report (Period Ending 09/30/2018)

Marcellus Shale Energy and Environment Laboratory (MSEEL)

Project Period (October 1, 2014 – September 30, 2019)

Submitted by:
Samuel Taylor

Signature

West Virginia University Research Corporation
DUN's Number: 191510239
886 Chestnut Ridge Road,
PO Box 6845, Morgantown WV, 26505
Tim.Carr@mail.wvu.edu
304-293-9660

Prepared for:
United States Department of Energy
National Energy Technology Laboratory

10/30/2018

U.S. DEPARTMENT OF ENERGY | NATIONAL ENERGY TECHNOLOGY LABORATORY

Office of Fossil Energy

U.S. DEPARTMENT OF ENERGY | NATIONAL ENERGY TECHNOLOGY LABORATORY

Executive Summary

The objective of the Marcellus Shale Energy and Environment Laboratory (MSEEL) is to provide a long-term field site to develop and validate new knowledge and technology to improve recovery efficiency and minimize environmental implications of unconventional resource development.

Integration of fiber-optic data from the MIP 3H continued with the focus on processing and analysis. This included analysis of long-period long-duration (LPLD) seismic evens and artificial neuro-network analysis of well data. Work also focused on kerogen models in the MSEEL wells across the Appalachian basin.

While makeup water was characterized by low TDS (total dissolved solids) and a dominance of calcium and sulfate ions, produced water from initial flowback is essentially a sodium/calcium chloride water. Other than slight increases in the proportion of barium and strontium, the ionic composition of produced changed very little through 888 days post completion.

The total methane emissions were 106 grams per hour (g/hr). This was the second to lowest emissions rate to date and was similar to the emissions encountered in the previous July (Audit 3). The main source of variability in site emissions is due to the emissions from the uncontrolled produced water storage tank. Emissions from the water tank ranged from 22.5 g/hr during this audit to as high as 3731 g/hr during Audit 2. Multiple dump events from the separators occurred during Audit 2 and we will examine all variables to understand if there are any correlations between increased methane emissions and throughput, activity or other variables. Overall, the average MSEEL site emissions from all six audits were 1363 g/hr which is lower than the average emissions of Rella et. al. – 1740 g/hr.

Preliminary results suggest that sulfate is below detection in the produced water from well 3H. Sulfate additions (2000 mg/L) dramatically increased the precipitation of Ra226 from well 3H (Figure 6.1), this result was seen in two separate water samples (3 and 4) collected in the spring and summer. Nutrients did not reduce the precipitation of Ra 226 by sulfate as the Sulfate(2000)_CNP was similar to the Sulfate(2000) treatment. This suggests that microorganisms cannot immobilize sulfate before it reacts with Ra 226.

Three separate papers submitted for publication/accepted for publication are attached as appendices.

Initial plans developed for MSEEL Phase 3 will be presented to the technical advisory group at the end of October for discussion.

Quarterly Progress Report

July 1 – September 30, 2018

Project Performance

This report summarizes the activities of Cooperative Agreement DE-FE0024297 (Marcellus Shale Energy and Environment Laboratory – MSEEL) with the West Virginia University Research Corporation (WVURC) during the second quarter of FY2018 (April 1 through June 30, 2018).

This report outlines the approach taken, including specific actions by subtopic. If there was no identified activity during the reporting period, the appropriate section is included but without additional information.

A summary of major lessons learned to this point of the project are provided as bullet points and will be added to as research is completed. New lessons listed below are:

1) Developed a kerogen model for the Marcellus Shale in the MSEEL wells (MIP 3H and MIP-SW) and compare these models to material from more and less mature wells in the Appalachian basin.
2) Developed method to process distributed temperature sensing (DTS) data that highlights production differences along the horizontal wellbore by foot, cluster or stage.
3) Synthetic based drilling mud is ecofriendly as well as helps with friction which resulted in faster drilling and reduced costs while leading to drilling waste from both the vertical and horizontal portions of the wells that passed all toxicity standards.
4) Microseismic monitoring does not completely define propped fractures and the extent of stimulated reservoir volume from hydraulic fracture stimulation. Requires integration of data from core, logs and slow slip seismic monitoring.
5) Production logging documents significant variations in production between completion types, stages and even clusters. Variations in production provide the necessary data for robust reservoir simulation.
6) Complex geology in laterals can lead to intercommunication between stages and reduced fracture stimulation efficiency. This can be mitigated with limited entry (engineered completions) that significantly improves fracture stimulation efficiency. NNE has continued the practice in subsequent wells. Planned production logging will help to define production efficiency.
7) The significant part of air emissions are in truck traffic, not in drilling and fracture operations on the pad. Emissions from both the pad and trucking can be reduced with operational modifications such as reducing dust and truck traffic during fracture stimulation (e.g., Sandbox) from bifuel (natural gas-diesel) engine operations.
8) Dual fuel engines demonstrated lower carbon monoxide (CO) emissions than diesel only operation. Dual fuel operations could reduce onsite diesel fuel consumption by 19 to 63% for drilling and 52% for hydraulic stimulation.
9) Biologic activity cannot be eliminated with biocides, only delayed. The biologic activity results in a unique biota that may affect operations. There may be other methods to control/influence biologic activity.
10) Water production changes rapidly after fracture stimulation in terms of volume (500 bbl/day to less than 1 bbl/day) and total dissolved solids (TDS from freshwater, 100 to 150g/L). Radioactivity is associated with produced water, not drill cuttings.

11) Drill cutting radioactivity levels were within West Virginia DEP standards of 5 pCi/g above background. This was true of both vertical and horizontal (Marcellus) sections.
12) Using the green drilling fluid Bio-Base 365, all drill cutting samples, vertical and horizontal, passed the USEPA's method 1311 (Toxicity Characteristics Leaching Procedure or TCLP) for inorganic and organic contaminants. This indicates that under Federal and West Virginia solid waste rules, these solid wastes would not be considered hazardous.
13) The absence of hazardous TCLP findings suggest that drilling fluids, not the inherent properties of the Marcellus formation, play the dominant role in determining drill cutting toxicity.
14) Concerning produced water quality, hydraulic fracturing fluid was nearly identical to makeup (Monongahela River) water. Initial produced water underwent a radical change in ionic composition and a two order of magnitude increase in total dissolved solids (TDS).
15) Produced water is highly saline and total dissolved solids (TDS) rapidly increased to a maximum between 100 and 150 g/L. There was negligible change in ionic composition between the initially produced water and that sampled five years post completion.
16) Concentrations of both 226 Ra and 228 Ra increased rapidly through the produced water cycle to combined maximum concentrations of 20,000 pCi/L in the first year post completion. These radium isotopes are critical regulatory determinants.
17) The volume of produced water decreased rapidly from nearly 500 bbl/day to less than 1 bbl/day after one year. Over this cycle produced water averaged about 6 bbl/day.
18) Developed a new frequency attribute calculated from the DAS data that reveals cross-stage fluid communication during hydraulic fracturing.
19) New microorganisms have been recognized in the deep biosphere represented by the Marcellus Shale. Understanding these organisms could reduce downhole well damage and precipitation of Ra in surface facilities.
20) Developed two different neural-network and support vector regression models to identify key parameters predicting potential screen out events and ultimate well performance.
21) Developed a new process to better analysis long-term fiber-optic DTS data to better understand differences in production efficiency and relation to completion efficiency as displayed by microseismic and DAS data.
22) Marcellus fractures result in cross-flow between stages and reduced completion efficiency that appears to affect production efficiency.
23) Improved understanding on the propagation of microseismic indications of fracturing upward into the overlying Mahantango Formation.
24) Machine learning can be used to better predict production based on fiber-optic data and identify individual stages that contribute significant production.
25) The cross-flow can be detected using advanced seismic attributes applied to fiber-optic DAS data. This is the first instance of using this approach with DAS data and has resulted in the development of software and a patent discovery.
26) Geochemical data is providing insight into the structure and chemistry of kerogen in the Marcellus and its interaction with completion fluids.

Project Management Update

Approach

The project management team will work to generate timely and accurate reporting, and to maintain project operations, including contracting, reporting, meeting organization, and general oversight.

Results and Discussion

The project team is tracking eight (8) milestones in this budget period.

	Task	Milestone	Status	Due Date
1.	2.1.2	Develop kerogen models of shale from different zones of MSEEL well and compare them to shales from wells in other parts of the basin	Complete Kerogen samples extracted from sidewall cores covering the whole Marcellus formation (ranging from Marcellus Top to Marcellus-Onondaga transition) have been analyzed using 13C NMR. New schematic kerogen models are being developed using lattice parameters and being compared to models of kerogen derived from wells in less mature part of the basin. Plan to synthesize results and submit publications in Fall 2018.	9/30/2018
2.	2.1.8	Geostatistical Well Analysis	Complete A paper was presented at URTeC (July) on a predictive data-driven machine learning model to understand the MSEEL well's performance and forecast the gas production using DTS data and daily flowing time as dynamic inputs. Papers using image analysis and nitrogen adsorption to quantify nano-pores in the Marcellus have been submitted.	9/30/2018
3.	2.1.7	Improved Reservoir Simulation for field implementation	On Track An improved history match that incorporates the unconventional fracture model and how to use this knowledge to increase production, efficiently space laterals and reduce cost. A manuscript has been accepted for presentation to the Society of Petroleum Engineers Annual Meeting.	10/31/2018

4.	2.1.5	Create a Comprehensive Fracture Model	On Track A provisional patent application for analysis of fiber-optic data is moving forward. Papers are accepted for fall meetings of SPE (Eastern Regional and National) and AAPG.	11/30/2018
5.	2.2.1	Completion of four additional methane audits to further assess temporal variability in methane emissions	On Track Four previous audits have shown significant temporal variability. Four or more (up to 8 more over 2 years) audits well help us understand (by increasing sample size) if variability correlates with temporal production, cumulative production, age, water production, or seasonal variability. Results will be presented in reporting, publications are possible.	12/31/2018
6.	2.1.2	Understanding the type, amount and origin of natural gas	On Track Data analysis and interpretations of pyrolysis data are currently underway. We expect to generate some preliminary data and make some conference presentations in Fall 2018 and submit publications by Spring 2019	3/30/2019
7.	2.2.1	Successful deployment of an open path methane monitoring system during site audits	On Track Industry seeks to reduce costs of audits and streamline greenhouse gas reporting programs. This will teach us if near-field, indirect quantification or detection methods are applicable to the Appalachia region, versus the well-established research in relatively flat and calm Barnett and Fayetteville plays.	3/30/2019
8.	2.2.1	Characterize chemical transformations during produced water storage from well 3H	On Track Will complete characterization of changes in produced water chemistry (specifically Fe, Sr, Ba, Ra 226, Ra 228) and biological activity (CO_2 and CH_4 production) that occur during short term storage (20 days). Measures of Ra activity (Ra 226 and Ra 228) of the solid precipitate formed during short term storage of produced water will also be completed.	3/30/2019

Topic 1 – Geologic Engineering

Approach

Integration of fiber-optic data from the MIP 3H continued with the focus on processing and analysis. We presented several papers showing the importance of multidisciplinary and multi-institutional team undertaking integrated geoscience, engineering and environmental studies to develop new knowledge of subsurface geology and engineering, and surface environmental impact to identify best practices that can optimize hydraulic fracture stimulation to increase flow rates, estimated ultimate recovery in order to reduce the number of wells and environmental impact.

Results and Discussion

Analysis of distributed temperature sensing (DTS) used to record temperature from early 2016 to present in the MIP-3H was presented at the Eastern Region Society Petroleum Engineers annual meeting in Pittsburgh, PA and published (SPE-194814-18ERM-MS, Appendix 1). In addition, after wellbore clean-out with water and nitrogen a flow scanner production log was conveyed on March 02, 2017. The flow scanner provides one day of gas and water production from each of the 28 stages in MIP-3H and from each of the clusters. The DTS data provides an opportunity to inspect the reservoir for Joule-Thompson (JT) effect, a phenomenon that describes cooling of an non-ideal gas as it expands from high pressure to low pressure, and obtain a relative production attribute along the lateral of the MIP-3H. The original fiber-optic DTS data shows the temperature along the lateral; however, due to the geometry of the well with toe up and the presence of a small fault and minor water production at Stage 10 relative gas production of each stage cannot be directly determined from the raw DTS data. We present two methods to generate DTS attributes that can be used to better reveal relative gas and water production through time from each perforation cluster and each stage of the MIP-3H. The first attribute deals with the deviations of the DTS measurements from the calculated geothermal temperature, while the second attribute calculated the difference between DTS temperature and the average daily DTS temperature along the lateral of the MIP-3H. We show that the latter DTS attribute provides a more robust image of temperature variations regime along the lateral than the former attribute. Negative values of the DTS attributes reveals JT cooling, resulting from stages of the MIP-3H with higher natural gas production. A correlation analysis of the production log with the calculated DTS attributes suggests that the production log is not representative of the entire production life of MIP-3H well. Temporal correlation with the DTS attributes is highest close to the production log recording day (March 2, 2017) decrease rapidly and the weak correlation switches from positive to negative.

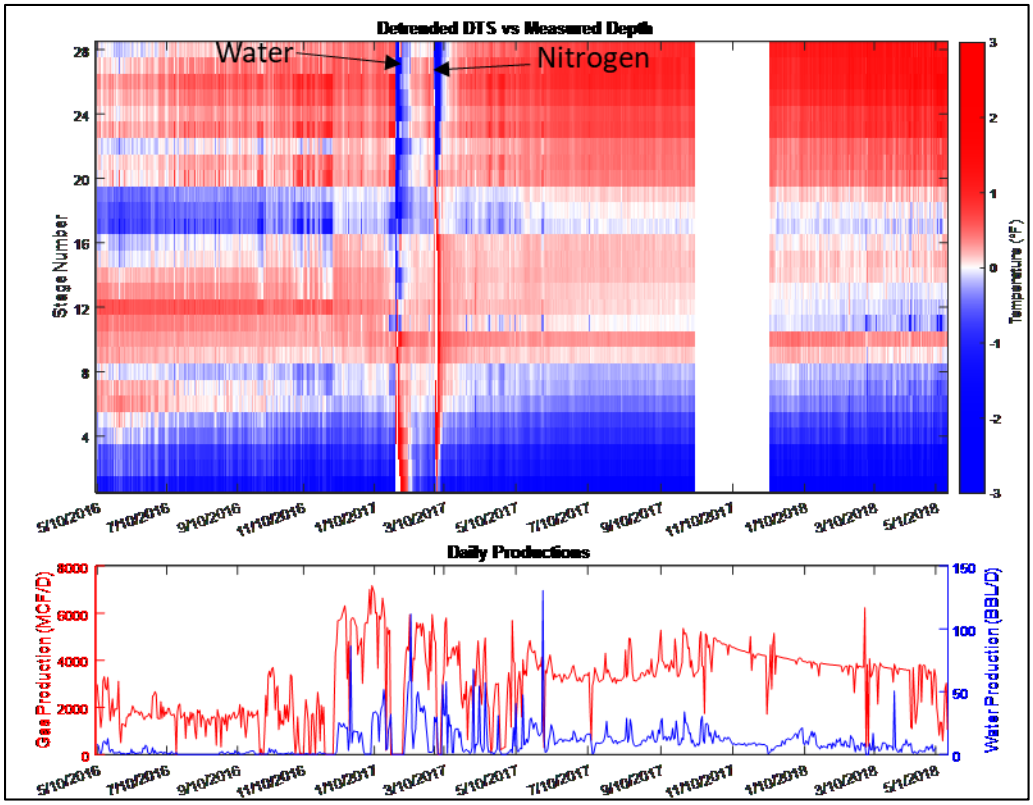

Figure 1.1: The processed DTS attribute data averaged to the stage scale. The arrows show the time that MIP-3H was washed with water and then with nitrogen foam prior to production logging. The warmer temperatures in stages 9 and 10 indicate less gass production and/or more water production. Relatively cooler temperatures in engineered stage 16-20 indicated higher gas production.

Completed work using the recorded data of a distributed temperature sensing (DTS) and distributed acoustic sensing (DAS) fiber-optic system from the MIP 3H to develop a predictive data-driven model to understand the well's performance and forecast the gas production using DTS data and daily flowing time as dynamic inputs, from May 2016 to May 2018. A total of 1320 DTS measurements along the lateral of the well MIP-3H for each day were upscaled to a stage scale by an averaging method. A multi-layer perceptron neural network (MLPNN) was trained with stage-based daily DTS data and daily flowing time to predict gas production for the next day (Figure 1.2). We carried out a sensitivity analysis by removing each stage DTS attribute from the input dataset to identify the most influential stages in predicting gas production. The sensitivity analysis (SA) shows that several stages carry higher weights in predicting gas production, while several stages have less impact on prediction accuracy. DAS data was only recorded during hydraulic fracturing of the well. DAS energy variance attribute may be inversely related to stage stimulation efficiency, was computed for each stage and compared with the results of the neural network SA. Stages with higher variance in DAS energy (less efficient stimulation) have less effect on neural network accuracy. This relationship is more significant for stages that are completed with limited entry approach in zones with similar minimum horizontal stress. The results of the sensitivity analysis was also compared with flow scanner production logging data. Results suggests that DAS data is more correlated with sensitivity analysis results than production logging data and a better predictor of well performance.

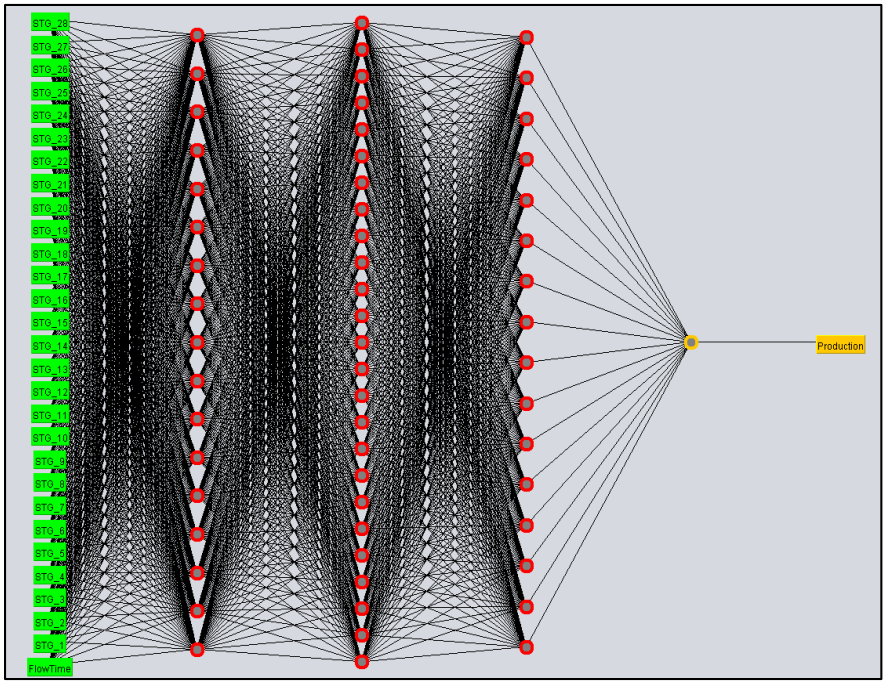

Figure 1.2: ANN structure with three hidden layers used for daily gas production prediction in this study. Note that input parameters are from previous days of the predicted productions.

Plan for Next Quarter

Continue to monitor DTS from MIP 3H and submit a manuscript on the processing and integration of DTS and DAS data as a solicited chapter in a book on fiber-optic data through the American Geophysical Union (AGU).

Topic 2 – Geophysical & Geomechanical

Approach

Geophysical and Geomechanical

Analysis of microseismic monitoring, fiber-optic distributed acoustic sensing (DAS), and distributed temperature sensing (DTS) observations made during the hydraulic fracture stimulation of the MIP-3H have been integrated with log data to develop a paper submitted to the journal *Interpretation* (Appendix 3). DAS and DTS data measure strain and temperature, respectively, along a fiber optic cable located behind the casing of the well. The presence of long-period long-duration (LPLD) events, similar in appearance to tectonic tremors, were documented in the borehole geophone data of one of the stimulated stages in the MIP-3H (Figure 2.1). In addition, low frequency events were recorded by the surface seismograms. LPLD events generally overlooked during the conventional processing of microseismic data represent significant non-brittle deformation produced during hydraulic fracture stimulation. 160 pre-existing fractures and two faults of suboptimal orientation are noted in the image logs of the studied stage. We identified two low-frequency events of large time duration (several hundred seconds) by comparing the borehole geophone data and DAS amplitude spectra of one of the stages at MIP-3H. These low frequency events have low amplitudes, lack of clear impulsive arrivals, and noise-like characteristics and are interpreted as LPLD events. The spatial and temporal similarities of these events indicate that DAS data could be used to identify LPLD events during hydraulic fracture stimulation.

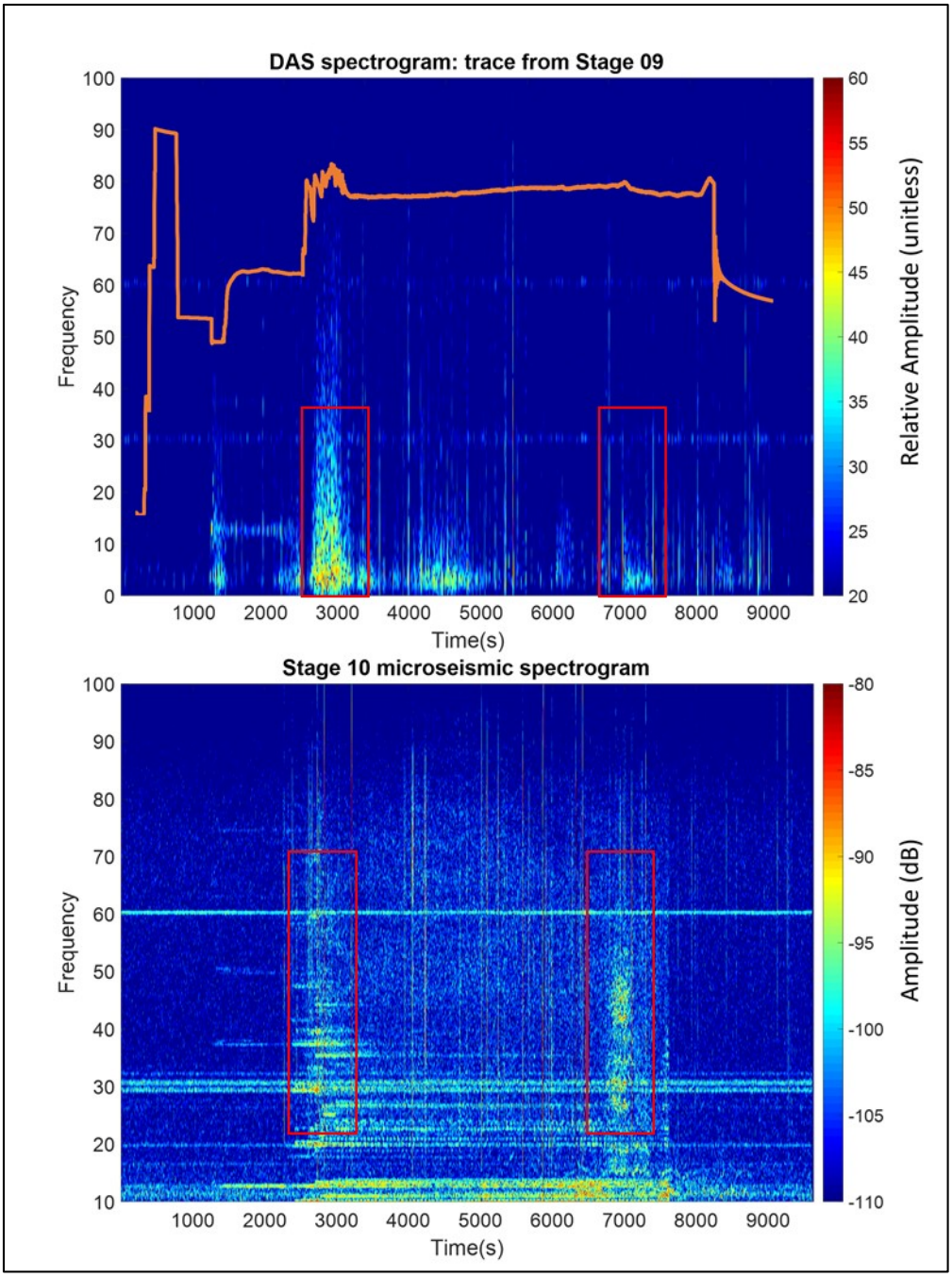

Figure 2.1: a) Stage 10 stimulation cause low frequency time intervals in DAS trace#371, which is in Stage 9. The orange curve shows the treatment pressure b) Spectrogram of sum of the z-components of Stage 10 microseismic. The low frequency strips around 10Hz, 30Hz and 60Hz appear to be noises picked by the interrogator at the surface.

Results & Discussion

Geophysical

Traditional fracture analysis continues. Table 2.1 shows the computed hydraulic fracture geometries for numerically modeled MIP-5H stage 21 through stage 25. Figure 2.2 shows the hydraulic fracture geometry for one of the primary induced hydraulic fractures in stage 25 of well MIP-5H. Figure 2.3 shows the cumulative proppant mass versus time (calculated and measured), Figure 2.4 shows the slurry volume injected versus time (calculated and measured),

and Figure 2.5 shows the surface pressure versus time (calculated and measured) for stage 25 of well MIP-5H.

Microseismic data was available for all stages numerically modeled during this quarterly period for well MIP-5H. Microseismic, well, and hydraulic fracture geometry data were visualized in three dimensions. Figure 2.6 through Figure 2.10 show side views of numerically modeled hydraulic fracture geometries and available measured microseismic events and magnitudes for stage 21 through stage 25, respectively, for well MIP-5H. Figure 2.11 shows an overview of the hydraulic fractures numerically modeled this quarter, as well as available microseismic event data and the entire MIP-5H wellbore. Figure 2.12 shows a top view of all numerically modeled hydraulic fracture geometries this quarter with available microseismic event data and the nearby section of the MIP-5H wellbore. Figure 2.13 shows an orthogonal projection of the numerically modeled hydraulic fracture geometries this quarter with available microseismic event data and the nearby section of the MIP-5H wellbore.

Vertical hydraulic fracture growth information was available from the Schlumberger presentation available on the MSEEL website (MSEEL_Microseismic_Evaluation_Schlumberger.pdf) and was compared with numerical model predictions. Figure 2.14 through Figure 2.18 show side views of calculated primary hydraulic fractures, measured microseismic events and magnitudes, and estimates of vertical fracture growth reported in Schlumberger's presentation (see MSEEL website) for stage 2, stage 5, stage 6, stage 7, and stage 8 of well MIP-5H. The upper red line indicates the estimate provided in the Schlumberger presentation of the extent of microseismic upward height growth, while the lower red line indicates the estimate of the extent of microseismic downward height growth.

Table 2.1: Computed Hydraulic Fracture Geometries – Stage 21 through Stage 25 – MIP-5H

STAGE	Fracture Half-Length (ft)	Fracture Height (ft)	Average Fracture Width (in)
21	598.6	316.6	0.027016
22	620.5	319.5	0.027759
23	540.2	297.8	0.02795
24	583.6	312.4	0.027346
25	590.1	316.1	0.026846

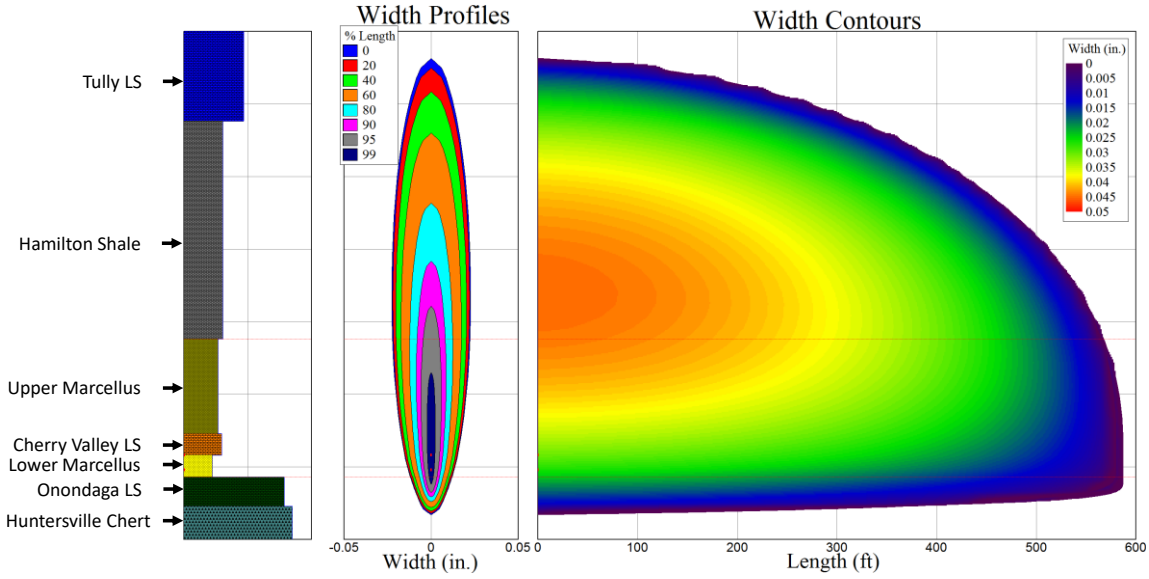

Figure 2.2: Primary Hydraulic Fracture Geometry for Stage 25 – MIP-5H

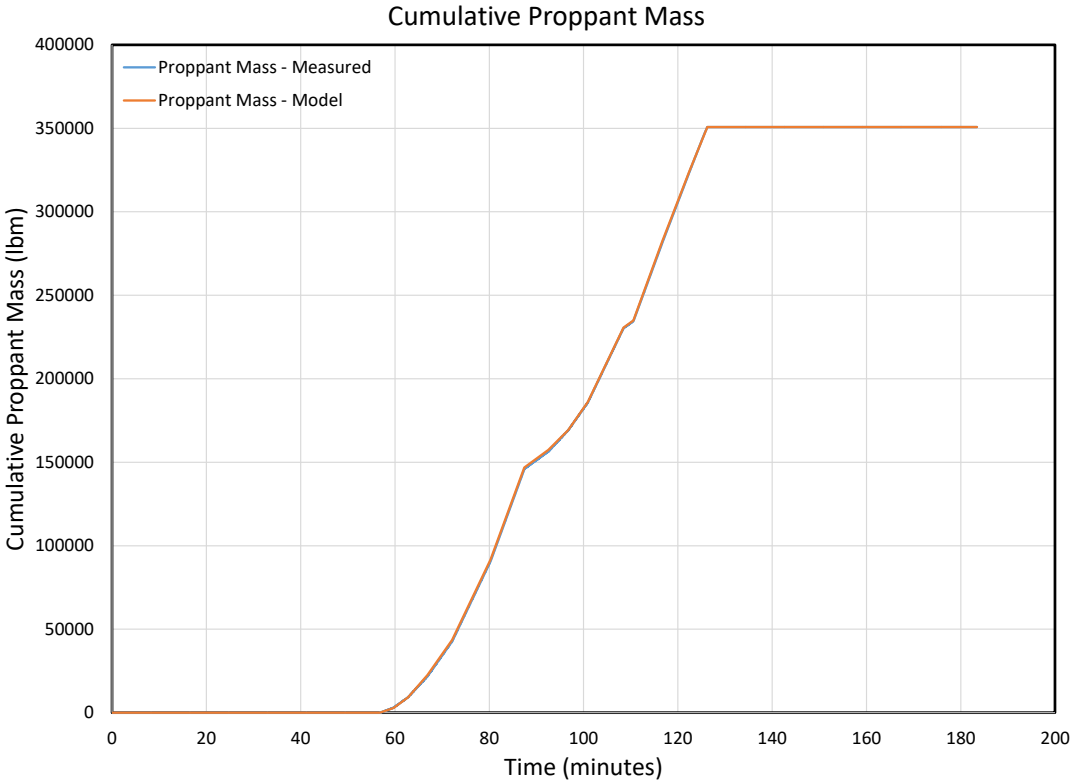

Figure 2.3: Cumulative Proppant Mass Injected for Stage 25 – MIP-5H

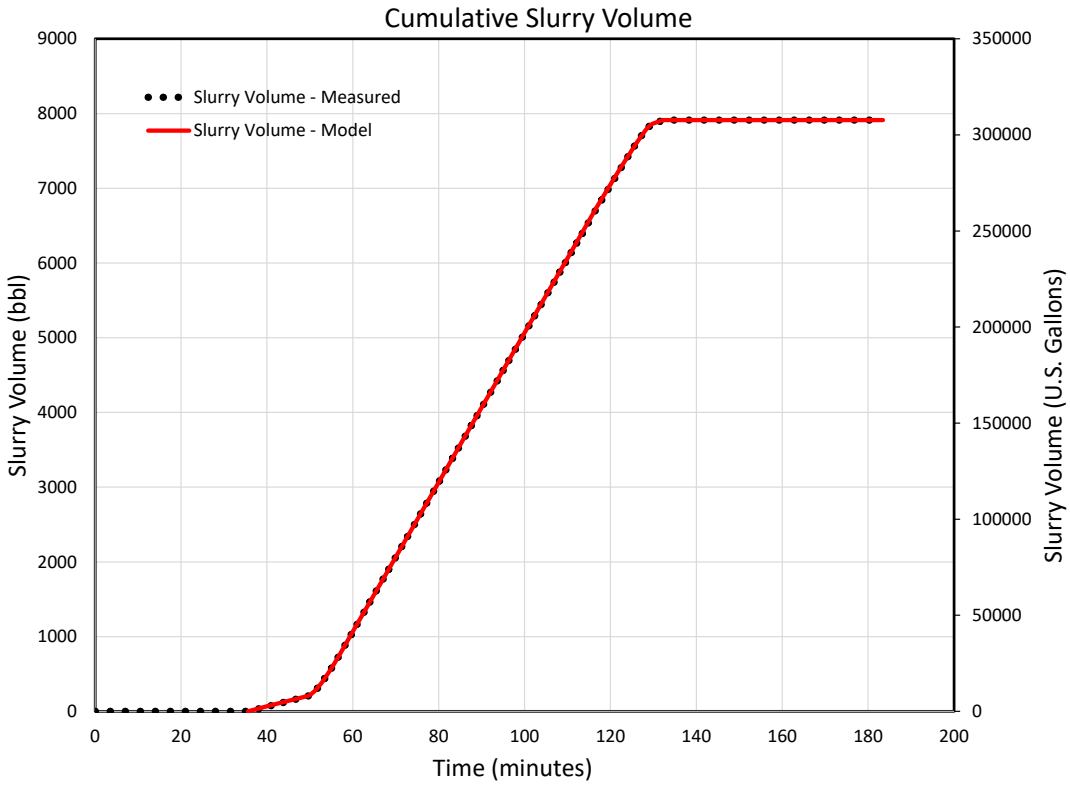

Figure 2.4: Cumulative Slurry Volume Injected for Stage 25 – MIP-5H

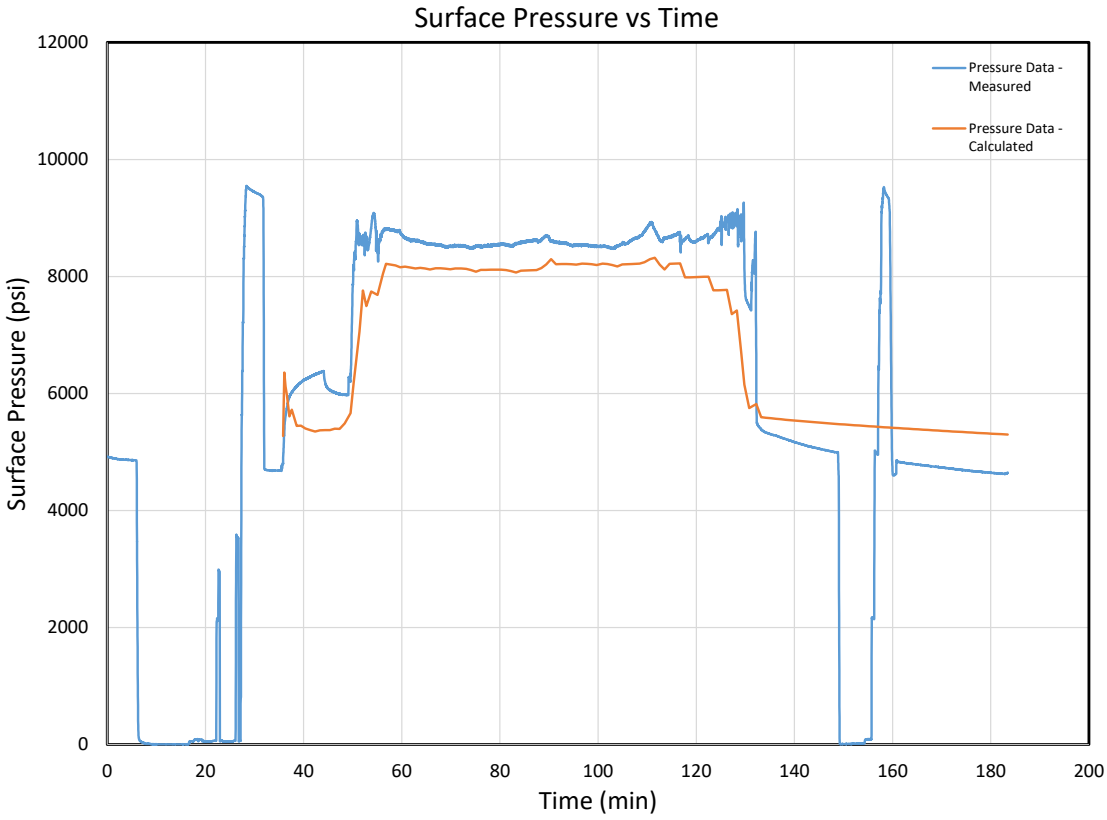

Figure 2.5: Surface Pressure versus Time for Stage 25 – MIP-5H

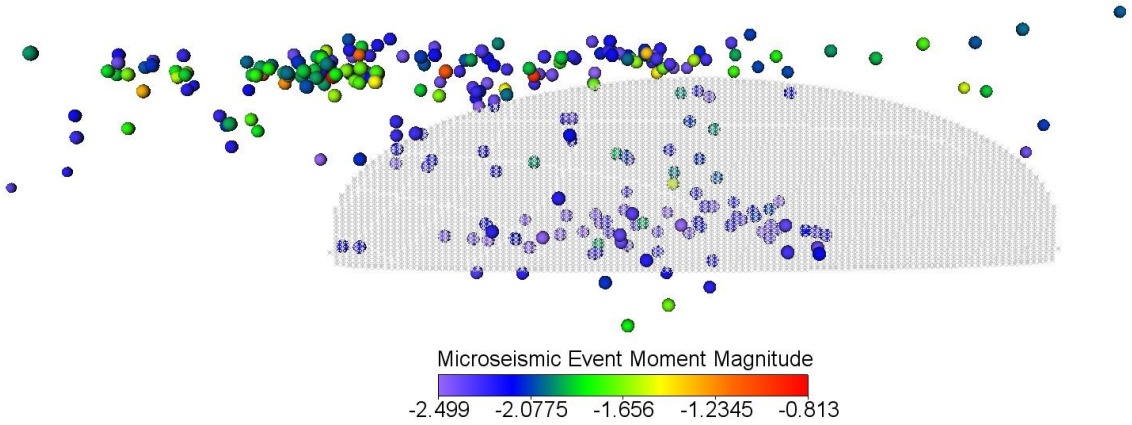

Figure 2.6: Side View of Calculated Primary Hydraulic Fracture and Measured Microseismic Events and Magnitudes for Stage 21 – MIP-5H

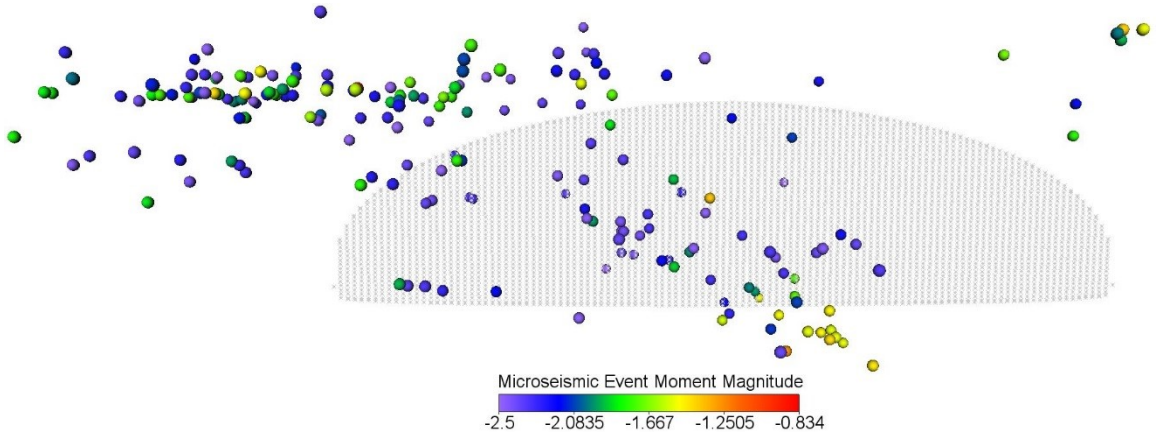

Figure 2.7: Side View of Calculated Primary Hydraulic Fracture and Measured Microseismic Events and Magnitudes for Stage 22 – MIP-5H

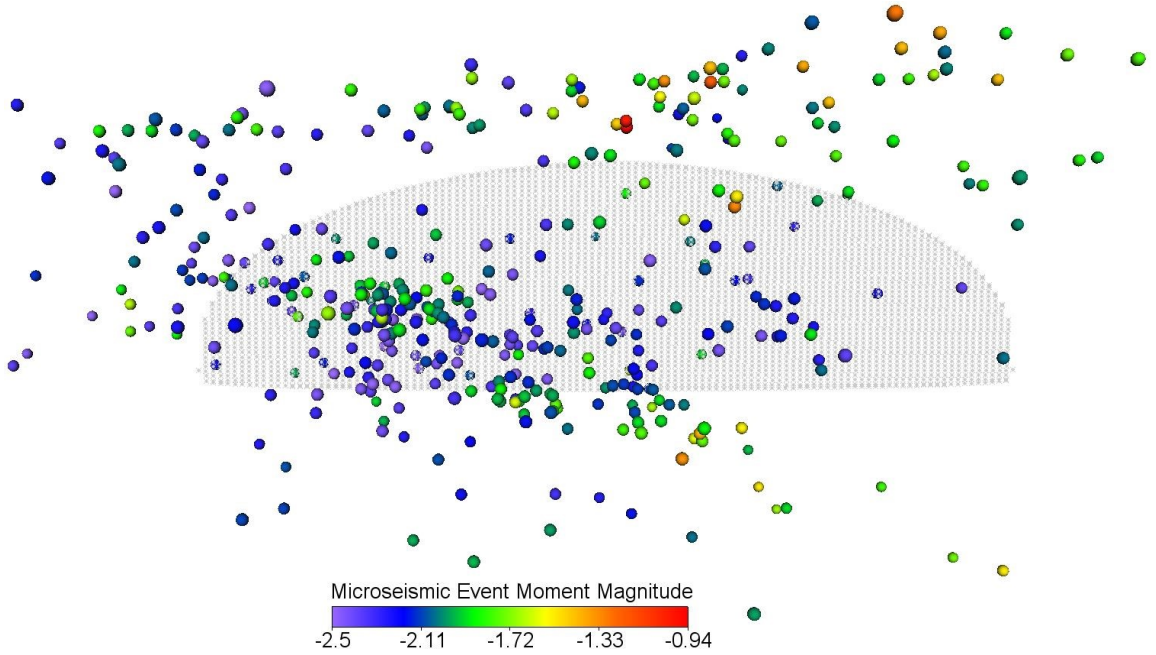

Figure 2.8: Side View of Calculated Primary Hydraulic Fracture and Measured Microseismic Events and Magnitudes for Stage 23 – MIP-5H

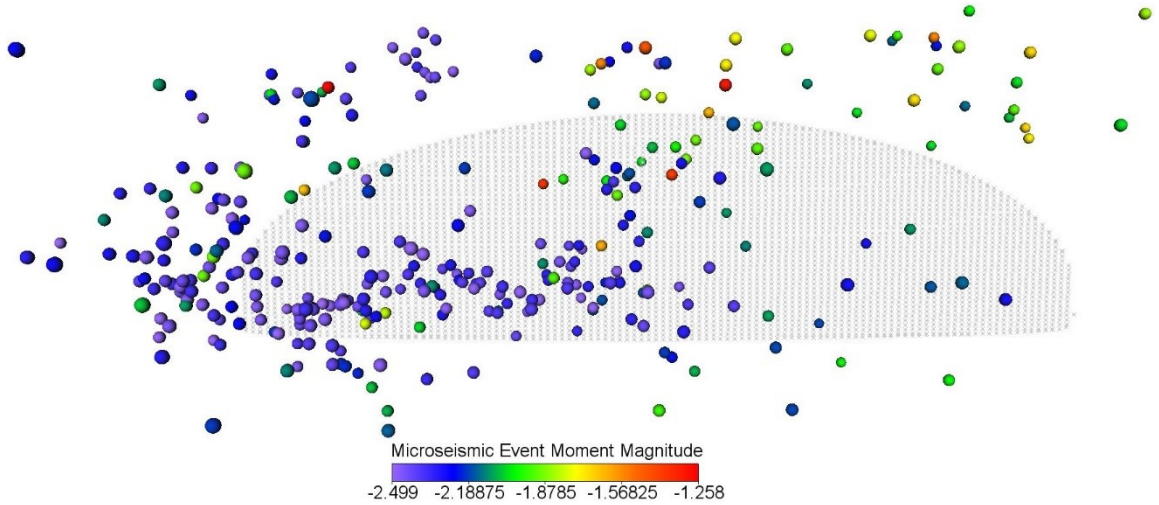

Figure 2.9: Side View of Calculated Primary Hydraulic Fracture and Measured Microseismic Events and Magnitudes for Stage 24 – MIP-5H

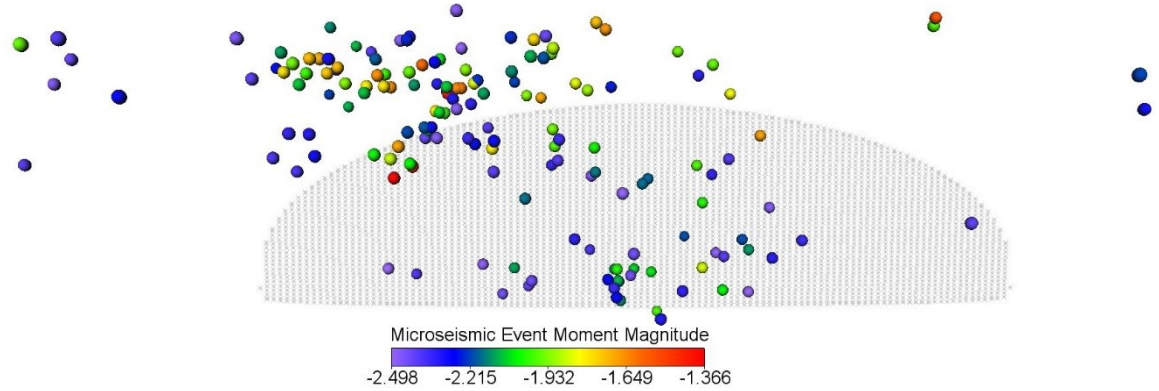

Figure 2.10: Side View of Calculated Primary Hydraulic Fracture and Measured Microseismic Events and Magnitudes for Stage 25 – MIP-5H

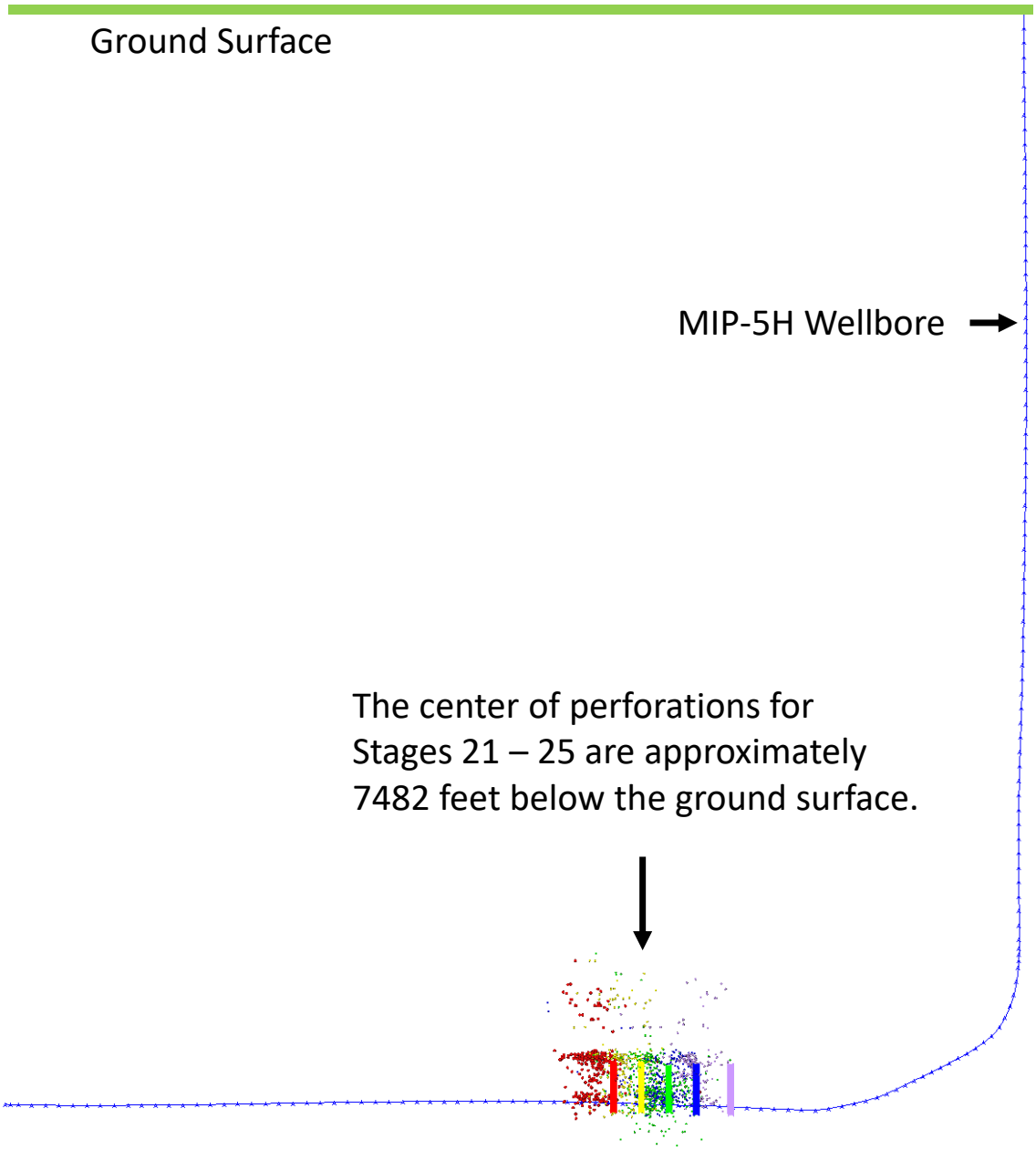

Figure 2.11: Overview of Calculated Primary Hydraulic Fracture Geometries, Available Measured Microseismic Events, and Entire Wellbore for Stage 21 through Stage 25 – MIP-5H

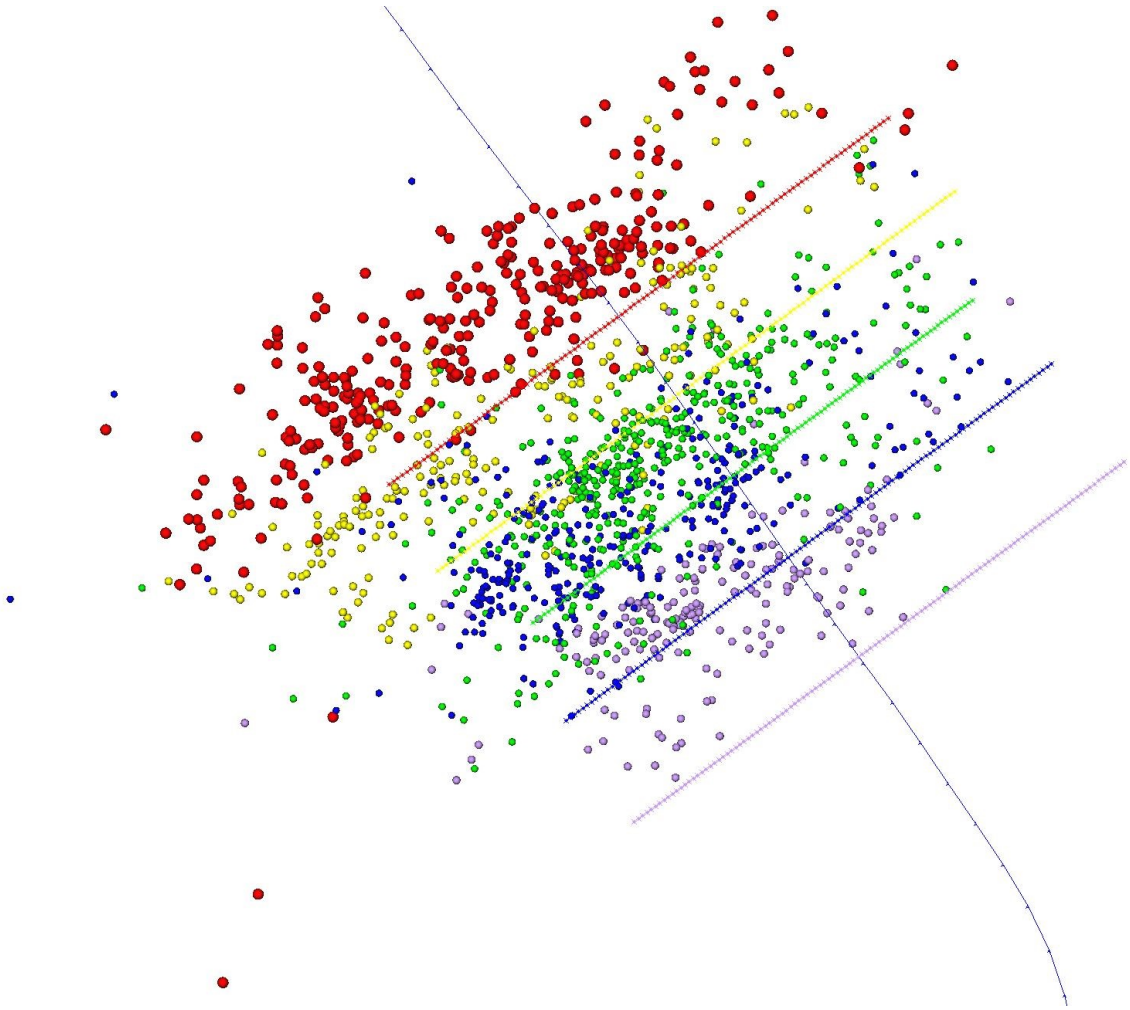

Figure 2.12: Top View of Calculated Primary Hydraulic Fracture Geometries, Available Measured Microseismic Events, and Nearby Wellbore for Stage 21 through Stage 25 – MIP-5H

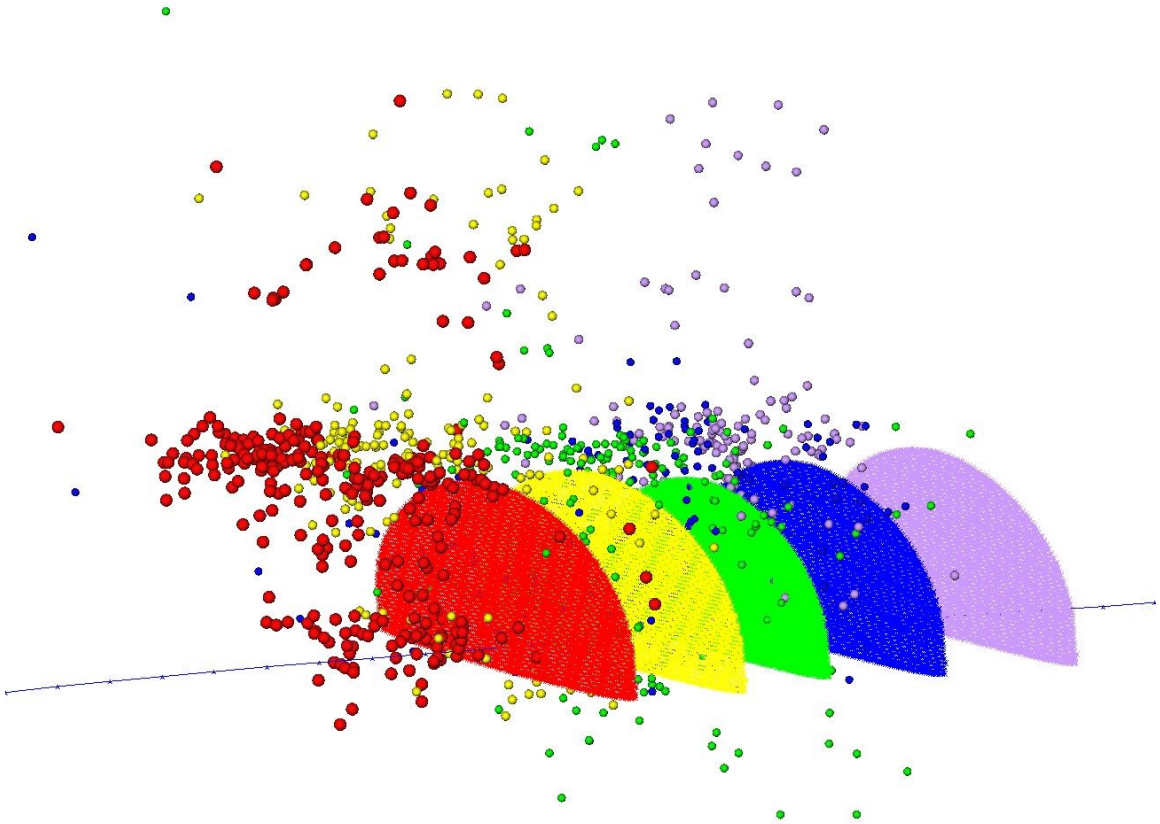

Figure 2.13: Orthogonal View of Calculated Primary Hydraulic Fracture Geometries, Available Measured Microseismic Events, and Nearby Wellbore for Stage 21 through Stage 25 – MIP-5H

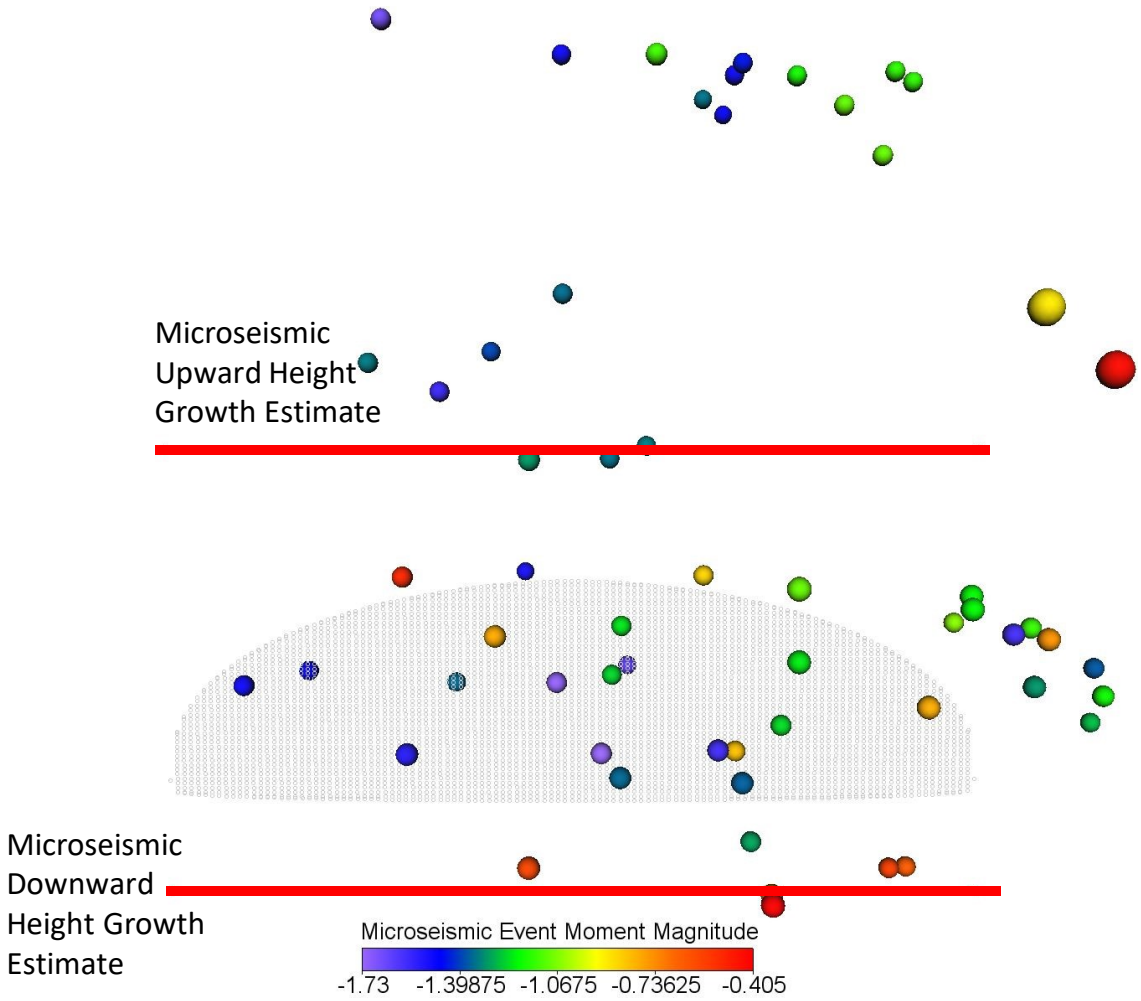

Figure 2.14: Side View of Calculated Primary Hydraulic Fracture, Measured Microseismic Events and Magnitudes, and Schlumberger Height Growth Estimates for Stage 2 – MIP-5H

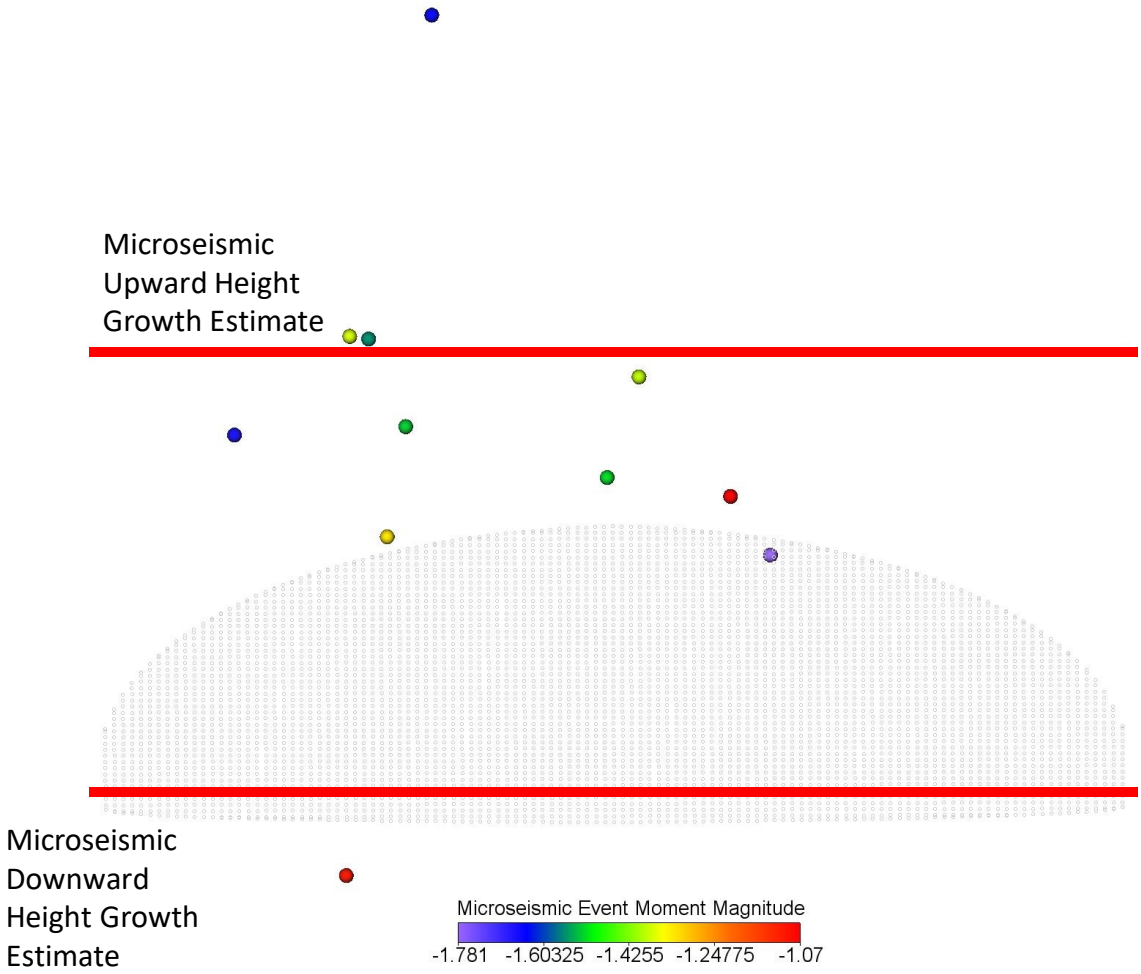

Figure 2.15: Side View of Calculated Primary Hydraulic Fracture, Measured Microseismic Events and Magnitudes, and Schlumberger Height Growth Estimates for Stage 5 – MIP-5H

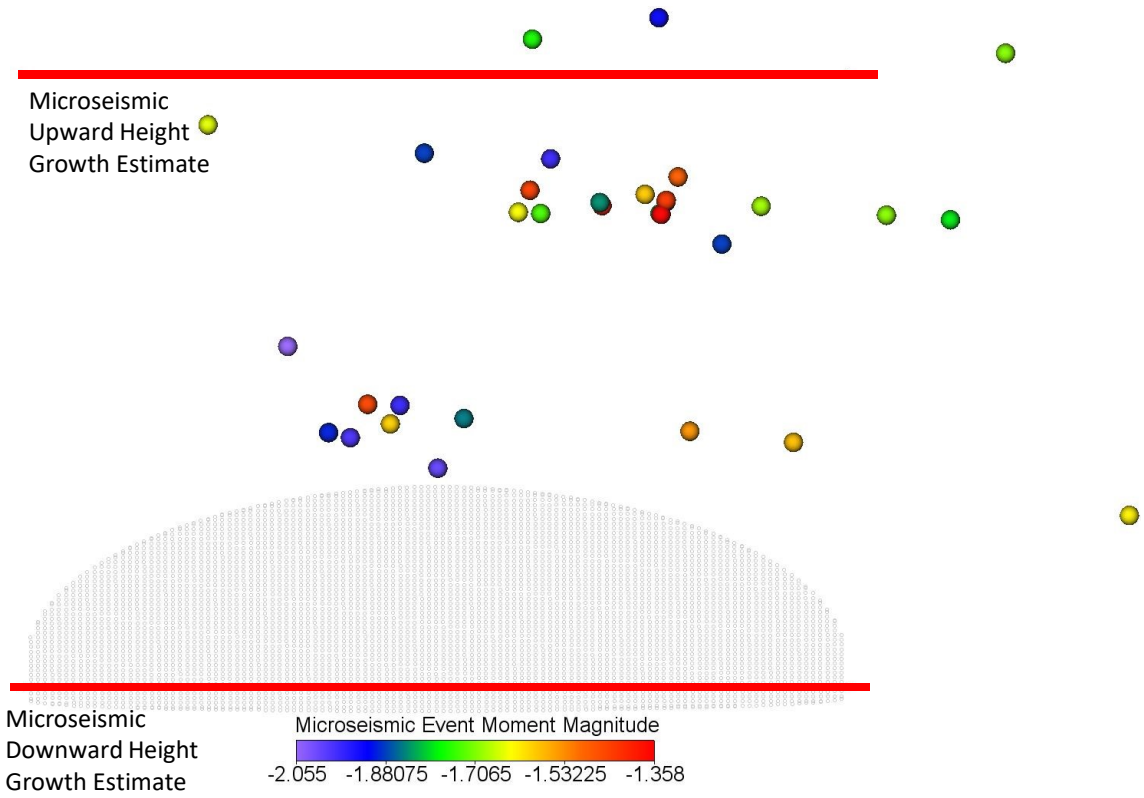

Figure 2.16: Side View of Calculated Primary Hydraulic Fracture, Measured Microseismic Events and Magnitudes, and Schlumberger Height Growth Estimates for Stage 6 – MIP-5H

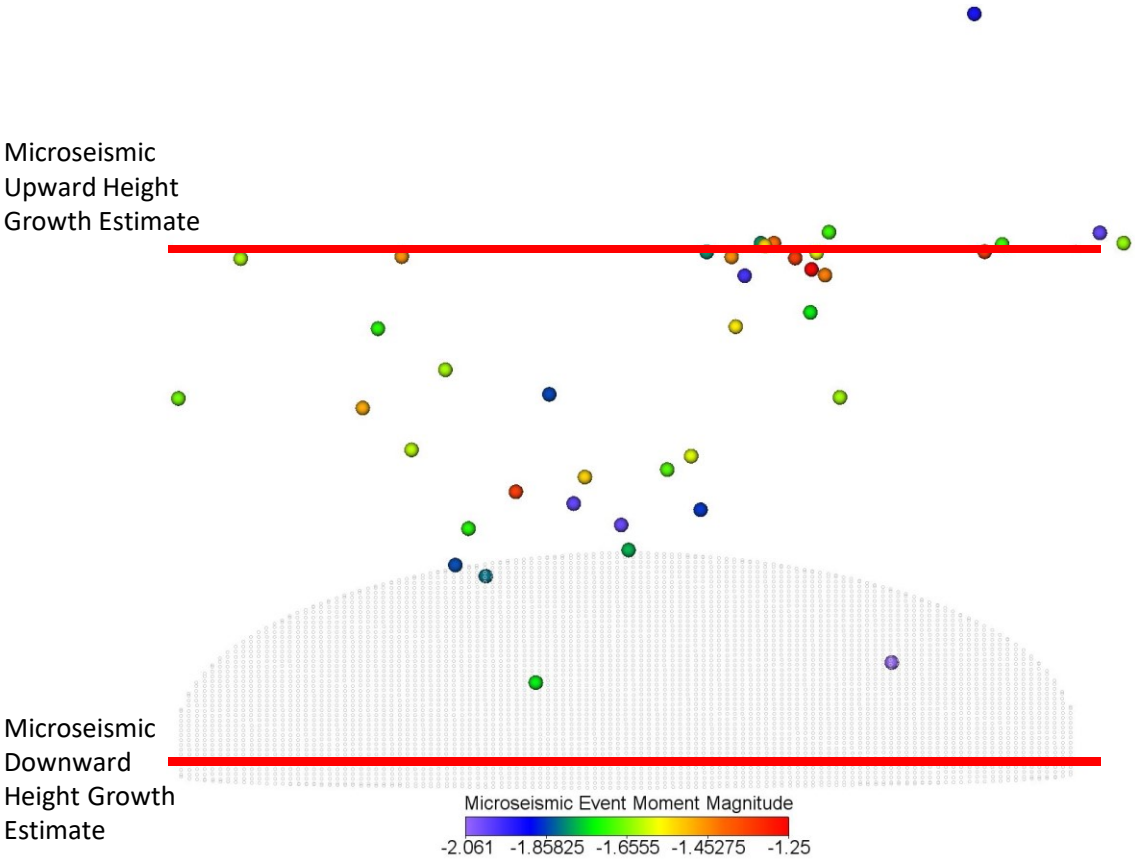

Figure 2.17: Side View of Calculated Primary Hydraulic Fracture, Measured Microseismic Events and Magnitudes, and Schlumberger Height Growth Estimates for Stage 7 – MIP-5H

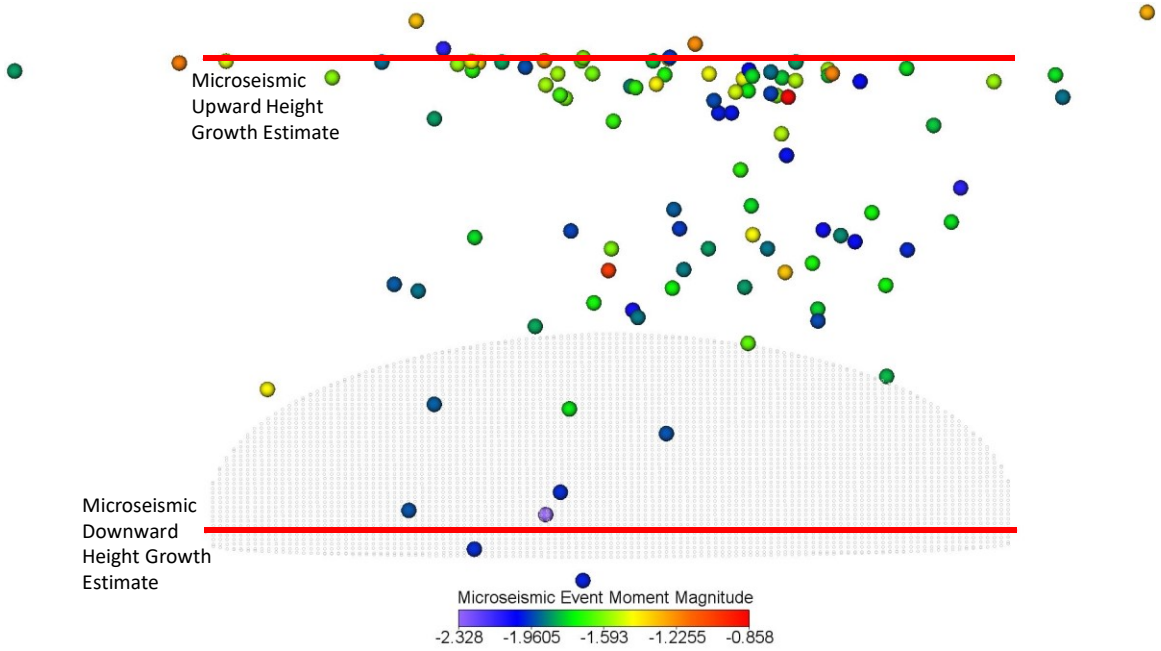

Figure 2.18: Side View of Calculated Primary Hydraulic Fracture, Measured Microseismic Events and Magnitudes, and Schlumberger Height Growth Estimates for Stage 8 – MIP-5H

Products

Several papers submitted or published.

Plan for Next Quarter

Geophysical and Geomechanical

Finish integration of log, fiber-optic and microseismic data.

The modeling study will be continued to investigate additional stimulation stages at well MIP-5H through the use of available information on the hydraulic fracturing field parameters (fluid volumes, pumping rate, proppant schedule, and geophysical data). The analysis of microseismic data will be continued and a comparison of hydraulic fracture geometries will be made with available microseismic data. Hydraulic fracture numerical modeling results will be compared with reported microseismic height growth estimates.

Topic 3 – Deep Subsurface Rock, Fluids, & Gas

Approach

The main focus of the subsurface team led by Sharma this quarter was to analyze core, fluid and gas samples collected from the MSEEL site. Members of Sharma's lab group (Dr. Warrier and Mr. Wilson) and Dr. Hanson from Mouser's lab group continue to coordinate and supervise all sample collections. Samples were also distributed to the research team at OSU and NETL for analysis under different sub-tasks. Several talks and presentations were given at local and regional conferences /universities.

Results & Discussion

Sharma's Lab

Milestone 1: Understanding spatial heterogeneity of kerogen across the entire Marcellus basin

Kerogen unit structures were developed by V. Agrawal across the entire Marcellus basin to understand the controls on sources of organic matter, depositional conditions of environment and thermal history on kerogen molecular structure.

Deliverables:

1) Manuscript currently under review in the journal *Scientific Reports*
2) Present the results in upcoming GSA conference in Indianapolis, Indiana.

Milestone 2: Developing new regression models for kerogen extracted including MSEEL well.

New linear and multiple regression models have been developed by V. Agrawal to accurately predict hydrocarbon potential and thermal maturity is Shale samples using kerogen structural parameters.

Deliverables:

1) A manuscript summarizing key finding is currently under review in the journal *Scientific Reports*.
2) The results will be presented at in AAPG 2019, San Antonio, Texas.

Milestone 3: Experiments to understand kerogen-frac fluid and interaction

The experiments, analysis and interpretations on understanding and shale-frac fluid interaction experiments were completed.

Deliverables:

1) A manuscript summarizing key finding is currently under review in journal *Environmental Science: Processes & Impacts.*
2) Present the results upcoming GSA conference in Indianapolis, Indiana
3) Finish analysis of all kerogen samples using ^{13}C solid state NMR by early spring 2019
4) Develop schematic kerogen models to understand any change on interaction with fracturing fluids.

Milestone 4: Understanding the type, amount and origin of gas.

Results from the open and closed pyrolysis experiments have been analyzed and quantified by V. Agrawal.

Deliverable: Submit a manuscript to the journal *AAPG bulletin* by Spring- Summer 2019.

Milestone 5: Microbial lipid analysis of sidewall cores from MSEEL

Ph.D. student Rawlings Akondi examined diversity and concentrations of the phospholipid fatty acids (PLFAs) and diglyceride fatty acids (DGFAs) to interpret environmental conditions and stress indicators on the MSEEL side wall cores.

Deliverable: A manuscript reporting the results is presently under review in the *Environmental Science: Processes & Impacts*.

Milestone 6: Analyzing the effect of storage on microbial community structure in subsurface cores. Ph.D. student Rawlings Akondi is presently working on a manuscript focused on the effects of long term storage on the lipid biomarker distribution in deep subsurface Marcellus Shale cores. The paper also highlights the adaptive ability of microbial life to physical and chemical changes in their environmental conditions. The sample used were fresh sidewall cores collected from the MSEEL and an old Marcellus core stored in Geological Survey for several years.

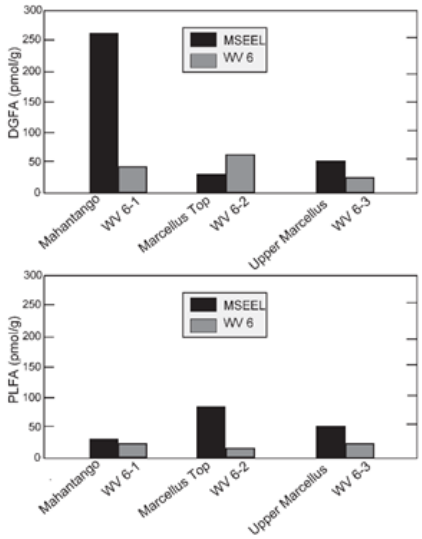

Figure 3.1: DGFA and PLFA yields in the WV 6 (WV 6-1, WV-2, and WV 6-3) and corresponding MSEEL (Mahantango, Marcellus Top, and upper Marcellus) core samples.

Apart from the WV 6-2 samples, the microbial lipid concentrations were higher in the MSEEL samples compared to the corresponding WV 6 samples of similar depth (Figure 3.1). A possible explanation as to why we observed decrease in lipid concentration with storage could be the inability of some of the subsurface adapted microbial species to adapt to exposure to surface conditions. It is also likely that the process of handling and storage like temperature/pressure variations created lethal effects for other microbial species through cell lysis and disaggregation of cells.

The variety of PLFA and DGFA biomarkers were also higher in the MSEEL core samples compared to the WV 6 samples (Figure 3.2). We observed that stress indicative biomarkers like oxiranes, keto, and dimethyl lipid fatty acids were only present in the MSEEL core samples. In contrast, other lipid profiles such as normal saturates, monounsaturates, and polyunsaturates were shared across the WV 6 and MSEEL core samples. The absence of some of the stress indicative biomarkers in the WV 6 core samples could suggest plausible changes in microbial due to changes in environmental conditions associated with sampling, handling, and storage. Our study highlights the adaptive ability of microbial life to physical and chemical changes in their environmental conditions.

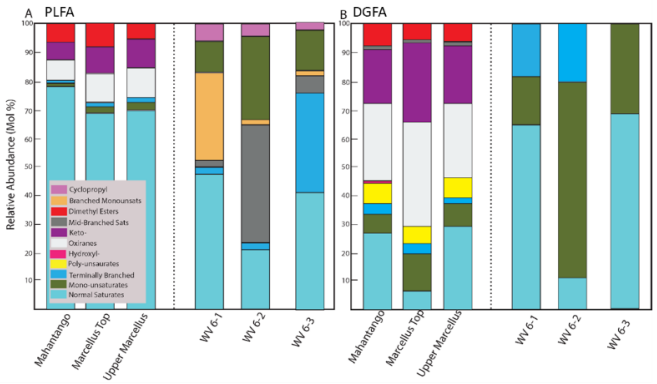

Figure 3.2: Relative abundances of PLFA and DGFA lipid biomarkers in the MSEEL (Mahantango, Marcellus Top, and upper Marcellus) and WV 6 (WV 6-1, WV-2, and WV 6-3) core samples.

Deliverable: The manuscript summarizing results will be ready for submission to the *Frontiers in Microbiology* in the late phases of Fall 2018.

Wrighton's Lab (OSU-CSU); Wilkins Lab (OSU-CSU)

Milestone 1: Characterization of all viruses that infect dominant *Halanaerobium* strains across shales.

Deliverable: This publication has been reviewed at Nature Microbiology, and is currently being revised. We anticipate submission of the edited document by end of October. Reb Daly is the first author with Mike Wilkins corresponding author.

The revised manuscript ('Viruses control dominant bacteria colonizing the terrestrial deep biosphere after hydraulic fracturing') for Nature Microbiology has been submitted and accepted for publication. (Deliverable 1). Figure 3.3 below is taken from the paper and shows viruses associated with a dominant shale bacterium, *Halanerobium*.

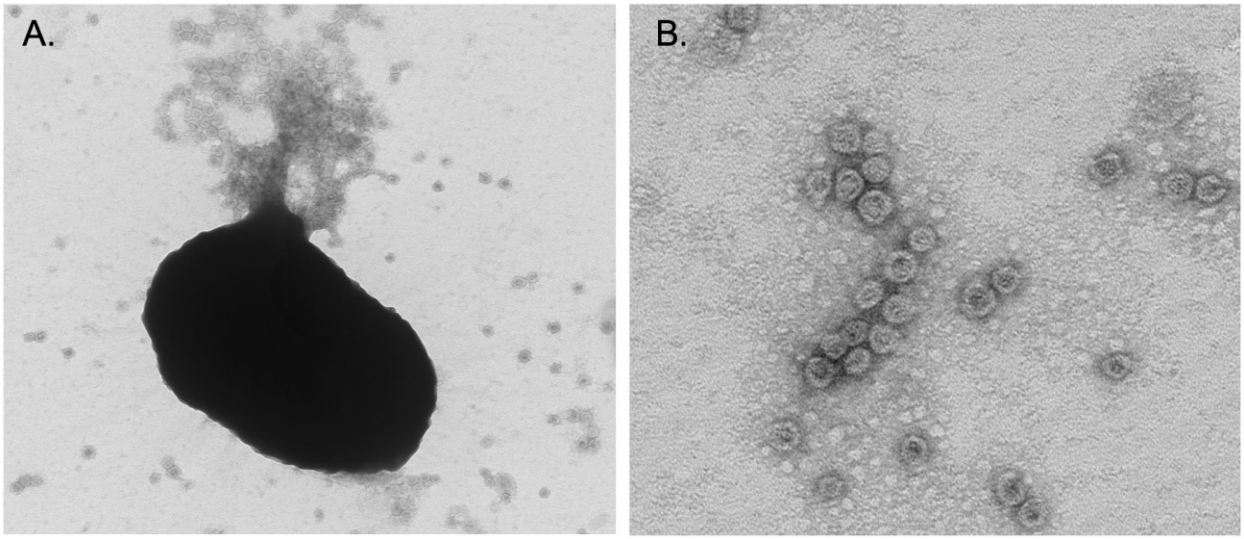

Figure 3.3: (A) Transmission electron micrograph of a Halanaerobium cell being lysed by viral activity. Viral particles, along with labile cellular metabolites, are released into the extracellular media as the cell bursts. (B) Viral particles in the extracellular media. This viral-mediated cell lysis and release of labile carbon compounds is thought to contribute to the persistence of biomass within the fractured shale network.

Since the last report, researchers have finalized biomass-visualizing experiments to complete another paper that will be drafted and submitted in the next quarter. Figure 3.4 shows high pressure conditions characteristic of deep fractured shales drive clumping behavior in dominant *Halanaerobium* microorganisms and synthesis of extracellular polymeric substances (EPS, or 'slime'). The accumulation of such biomass in narrow fractures could have implications for reservoir performance.

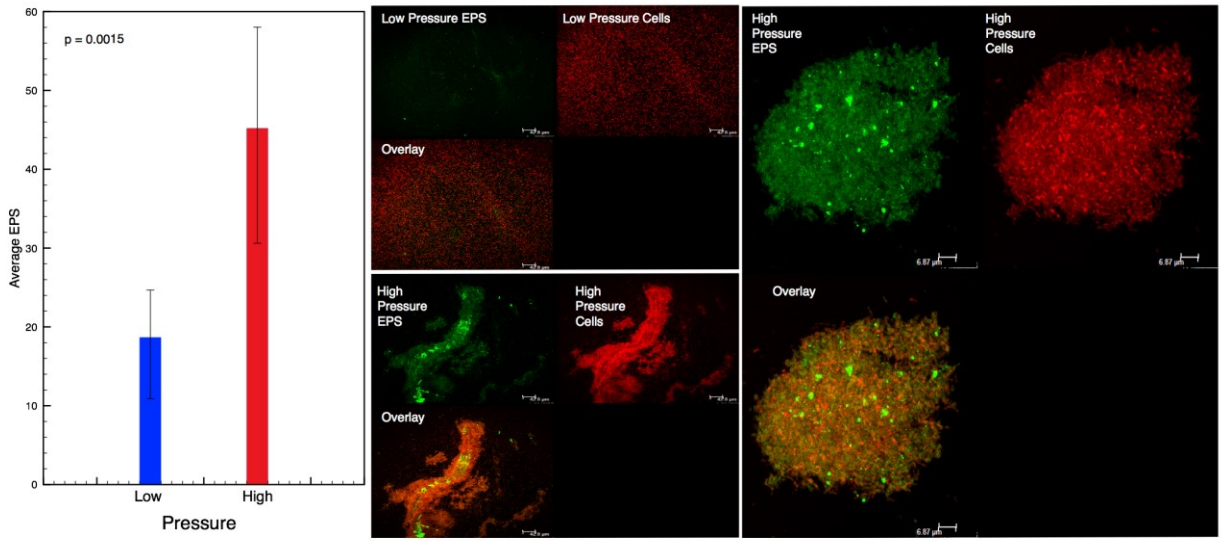

Figure 3.4: Confocal scanning laser microscopy analysis of *Halanaerobium* grown at high (35 MPa) and low (0.1 MPa) pressure. Bar graph represents average amount of extracellular polymeric substance measured from three biological replicates grown at high and low pressure (p-value < 0.05, student t-test). Confocal image panel represents *Halanaerobium* dispersed growth at low pressure and floating biofilms at high pressure. Styo59 (red) used to stain nucleic acids, Alexa488-ConA (green) used to stain α-mannopyranosyl and α-glucopyranosyl residues within the EPS matrix. The plotted average EPS values represent the corrected total fluorescence which is the [image integrated density – (area of selected cell x average fluorescence of background readings)]

Mouser Lab (OSU-UNH)

Milestone 1: Characterization of Arcobacter/Marinobacter bacterial isolate metabolic potential, MSEEL metagenomes, and trends in N, S, C biogeochemistry for MSEEL fluid samples.

This manuscript was accepted for publication on October 17, 2018 (see Products below):

Hydraulic fracturing is the prevailing method for enhancing recovery of hydrocarbon resources from unconventional shale formations, yet little is understood regarding the microbial impact on biogeochemical cycling in natural-gas wells. Although the metabolisms of certain fermentative bacteria and methanogenic archaea that dominate in later produced fluids have been well studied, few details have been reported on microorganisms prevelant during the early flowback period, when oxygen and other surface-derived oxyanions and nutrients become depleted. Here, we report the isolation and genomic characterization of Marinobacter and Arcobacter bacterial species from natural-gas wells producing from the Utica, Point Pleasant, and Marcellus formations coupled to supporting geochemical and metagenomic analyses of produced fluid samples. These shale-derived Marinobacter sp. are capable of utilizing a diversity of organic carbon sources including aliphatic and aromatic hydrocarbons, amino acids, and carboxylic acids. Marinobacter and Arcobacter can metabolize organic nitrogen sources and have the capacity for denitrification and dissimilatory nitrate reduction to ammonia (DNRA) respectively; with nitrate ammonification processes partially explaining high concentrations of ammonia measured in shale produced fluids. Arcobacter is capable of chemosynthetic sulfur oxidation, which could fuel metabolic processes for other heterotrophic, fermentative, or sulfate-reducing community members. Our analysis revealed mechanisms for growth of these taxa across a broad range of salinities (up to 14% salt), which explains their enrichment during early production. These results demonstrate the prevalence of Marinobacter and Arcobacter during a key maturation phase of hydraulically fractured natural-gas wells, and highlight the significant role these genera play in biogeochemical cycling for this economically important energy system.

Milestone 2: Complete analysis of volatile fatty acids and alcohols of MSEEL produced fluids. Evans will travel to UNH on Aug 12-18 to use the GC-FID and GC-MS in the Mouser lab for analysis of aldehydes; alcohols, acetone, glycols, etc.

Samples were analyzed at UNH during this quarter. Summary of preliminary results related to the analysis of volatile fatty acids and alcohol analysis via GC-FID. Samples were prepared/analyzed by Morgan Volker and Jenna Luek.

Method

1. Sample Preparation

Source fluids used to make up the fracturing fluid, fracture fluids, flowback fluids, and produced water samples were collected in clean HDPE sampling containers with minimal headspace and stored on ice for transport. Fluid samples were filtered with 0.22 μM polyethersulfone filters then transferred to clean glass containers and frozen at -20°C. Immediately prior to analysis, fluid samples were thawed, shaken, and a 1.5 mL aliquot transferred to a 2 mL Eppendorf centrifuge tube. Fluid samples were centrifuged for 1 minute at 20°C/10,000 x *g* to remove particulates (additional precipitate formed after freezing), and 750 μL carefully aliquoted into new 2 mL GC vials for analysis.

2. Sample Analysis

Fluid samples were analyzed using a TRACE 1300 Gas Chromatograph with flame ionization detection (FID) (Thermo Fisher Scientific) equipped with a Zebron ZB-WAX$_{PLUS}$ column (Phenomonex) (30m, 0.25 mm ID, 0.25 μM film thickness). Using an AI 1310 autosampler, 1 μL of sample was injected to the inlet (225°C, splitless) with a column flow rate of 1.5 mL min^{-1} He and the following oven parameters applied: 30°C 5 min, ramp to 200°C at 10°C min^{-1}, hold 2 min, ramp to 250°C at 25°C min^{-1}, hold 2 min, for a total run time of 30.8 min. The FID detector temperature was set to 225°C. Data was processed using Chromeleon 7 software (Thermo Scientific) and all peaks manually checked for proper integration.

3. Quality Assurance

A stock standard solution of acetaldehyde, acetone, methanol, propanol, and ethylene glycol was prepared at 6.25 mM each and diluted to make a calibration curve between 50 μM and 6.25 mM. We were unable to obtain adequate separation in retention time for ethanol and propanol (similar response factors), so values are reported as ethanol+propanol against the propanol standard. The following R^2 values for linear fit were obtained: acetaldehyde 0.9994, acetone 0.9996, methanol 0.9978, propanol 0.9953, and ethylene glycol 0.9944. Between each injection, the needle was washed with hexane and deionized water. Between each sample, two deionized water blanks were run to limit carryover, and a 625 μM check standard was analyzed approximately every 12 samples. The check standard revealed a decrease in ethylene glycol retention time (16.6 min – 15.9 min) over the sample run; consequently, ethylene glycol retention peaks was therefore confirmed against the nearest check standard in the sample run. Samples were diluted and re-run if one or more peaks fell outside of the calibration. A field blank and a lab blank were analyzed to investigate possible sources of contamination. Ten deionized water blanks were analyzed to calculate the limit of detection (average$_{blank}$ + 3 standard deviations) and are given in Table 3.1. No distinguishable peaks were detected in the blanks so the LOD was set to the lowest point on the calibration curve for acetaldehyde, acetone, and methanol.

Table 3.1: Limit of detection, field blank, Monongahela River aqueous concentrations for selected analytes analyzed using GC-FID.

	LOD (□M)	River Water (n=2)	Field Blank
Acetaldehyde	50	ND	ND
Acetone	50	ND	ND
Methanol	50	ND	237
Ethanol+Propanol	306	179	182
Ethylene Glycol	308	161	139

Acetaldehyde was detected on in the 5H well at two time points, both below the limit of detection. Other analytes are shown in Figure 3.5.

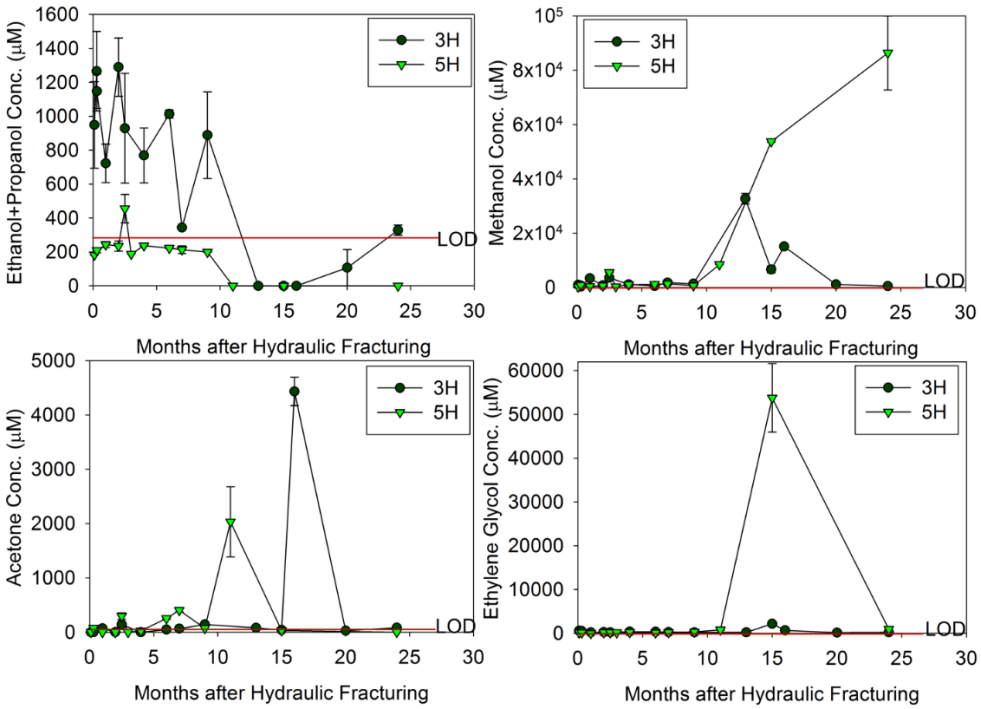

Figure 3.5: Hydraulic fracturing flowback and produced water concentrations of ethanol+propanol, methanol, acetone, and ethylene glycol from the MSEEL MIP3H and MIP5H field sites. Limits of detection (LOD) shown as a red line in each plot. Error bars represent the standard error of analytical replicates. Individual data points are provided at the end of this report.

Alcohols relevant both to fracturing operations and microbial pathways were detected in both the 3H and 5H wells. Initially, the FracFocus report for both 3H and 5H indicate the injection of ethanol during fracturing (FracFocus). Ethanol+propanol, which co-eluted and were not possible to separate under the current method, were present in concentrations below the LOD up to 1289 µM. In the 3H well, concentrations were initially between 723 and 1289 µM but quickly decreased to below the LOD by 12 months after fracturing. These losses are likely due to dilution through time as formation waters mix with injected fluids. Interestingly, except for two time points during early flowback (2.5 months after fracturing, 456 µM), ethanol+propanol

concentrations were below the LOD in the 5H well. These trends stand in contrast to ethanol+propanol trends previously reported from other wells (Borton et al. 2018), where production of alcohols from fermentation is thought to contribute to high ethanol concentrations in later produced fluids. The low and erratic ethanol+propanol trends may be due to an error in the method, or it may be that these species are unusually low in MIP3H and 5H compared to other wells.

Methanol, like ethanol, was listed as an additive in the FracFocus reports for the 3H and 5H wells (FracFocus). Methanol concentrations were initially low (291-939 µM) but reached concentrations between 15,000-86,000 µM 12 months or more after fracturing. Methanol may be a byproduct of microbial fermentation, or may also be added in later production stages. The accumulation of methanol at later time points supports the previously tested hypothesis that methylotrophic methanogenesis does not take place in shale ecosystems (Daly et al. 2016, Borton et al. 2018).

Acetone was present in a few early flowback samples for both wells, but was largely below detection until 3-17 months after fracturing occurred, where acetone concentrations reached 2033 µM in the 5H well and 4433 µM in the 3H well. Acetone can be produced through several different microbial pathways, including the degradation of polypropylene glycols, acetoacetate, and via a unique pyruvate fermentation mechanism utilized by certain Clostridium *spp* (Caspi et al. 2014). Acetone is not disclosed as an additive in either FracFocus report (FracFocus). Interestingly, the FracFocus report for the 5H well disclosed polypropylene glycols as an injected additive (FracFocus), which may produce acetone as a product during degradation. Despite this possible pathway, a clear explanation for the high concentration of acetone more than a year after fracturing needs to be discerned and identified.

Ethylene glycol was disclosed as an injected additive in both the 3H and 5H wells, and was detected in varying concentrations in produced fluid samples. Initial input samples for both wells contained concentrations between the LOD (308 µM) and 572 µM, but concentrations quickly diminished in subsequent flowback samples. This decrease may be in part due to dilution but may also be explained by microbial transformation as previously reported (Daly et al. 2016, Borton et al. 2018). Ethylene glycol concentrations increase 15 months after fracturing, spiking as high as 53700 µM in the 5H well and 2164 µM in the 3H well. The high concentrations of ethylene glycol observed may be due to its addition by operators as a weatherizer to prevent freezing, as this coincides with cold winter months at the well site in West Virginia.

Citations

Borton, M. A., Hoyt, D. W., Roux, S., Daly, R. A., Welch, S. A., Nicora, C. D., et al. (2018). Coupled laboratory and field investigations resolve microbial interactions that underpin persistence in hydraulically fractured shales. *PNAS*, 201800155. doi:10.1073/pnas.1800155115.

Caspi, R., Altman, T., Billington, R., Dreher, K., Foerster, H., Fulcher, C. A., et al. (2014). The MetaCyc database of metabolic pathways and enzymes and the BioCyc collection of Pathway/Genome Databases. *Nucleic Acids Research* 42, D459–D471. doi:10.1093/nar/gkt1103.

Daly, R. A., Borton, M. A., Wilkins, M. J., Hoyt, D. W., Kountz, D. J., Wolfe, R. A., et al. (2016). Microbial metabolisms in a 2.5-km-deep ecosystem created by hydraulic fracturing in shales. *Nature Microbiology* 1, nmicrobiol2016146. doi:10.1038/nmicrobiol.2016.146.

Cole's Lab (OSU)

Milestone 1: Complete XRF analyses of solids from key core samples (Tully Limestone, Mahantango, Marcellus Top, Middle Marcellus, and Lower Marcellus) to quantify major and trace element chemistry of splits from the same core analyzed by Wilkins and Darrah Labs.

Deliverable 1: Compilation of the XRF data on rock composition for MSEEL rock samples listed above.

Five core samples from the MSEEL well MIP-3H were analyzed with X-ray fluorescence (XRF) to determine whole rock major and trace element compositions. In addition, two of the same five samples were analyzed for trace element geochemistry at the same laboratory using laser ablation ICP-MS. The hydraulic fracturing target for the MSEEL study, the Lower Marcellus, is among those selected for determining elemental information, but sample selection was also guided in part by collaboration with other research groups for which whole-rock quantitative elemental compositions for specific sample depths is advantageous. The samples targeted include the Tully Limestone (depth 7200′), The Mahantango Formation (7440′), Marcellus Top (7451.5′), Middle Marcellus (7509′), and Lower Marcellus (7543′).

XRF results for major oxides are presented in Table 3.2, with total iron expressed as FeO, and element concentrations listed unnormalized. During the preparation of glass beads for XRF analysis, fusion of powdered rock sample plus flux at 1000 degrees C drives off volatile components such as CO_2 in carbonates, OH and H_2O in hydrous phases, and organic compounds. These volatiles are reported as loss on ignition (LOI). Table 3.3 presents these data normalized without considering the volatile components. Trace element concentrations, and totals for major, trace and LOI are given in Table 3.4.

Table 3.2: Unnormalized Major Elements and LOI (weight percent)

	Tully	Mah	Marc Top	Marc Mid	Lower Marc
	M-7200	**M-7440**	**M-7451.5**	**M-7509**	**M-7543**
SiO2	40.82	59.93	57.26	58.11	48.14
TiO2	0.566	0.688	0.615	0.515	0.334
Al2O3	12.92	17.19	15.31	12.06	8.36
FeO	3.34	5.14	7.97	3.97	5.77
MnO	0.104	0.019	0.022	0.012	0.014
MgO	1.62	1.36	1.30	1.17	0.85
CaO	19.20	0.50	0.67	1.51	9.29
Na2O	0.36	0.45	0.39	0.45	0.40
K2O	2.98	4.07	3.56	2.99	2.25
P2O5	0.134	0.062	0.078	0.109	0.084
Sum	82.06	89.41	87.16	80.88	75.49
LOI %	16.86	9.80	11.65	18.08	19.47

Table 3.3: Normalized Major Elements (weight percent)

	Tully	Mah	Marc Top	Marc Mid	Lower Marc
	M-7200	**M-7440**	**M-7451.5**	**M-7509**	**M-7543**
SiO2	49.74	67.03	65.69	71.84	63.77
TiO2	0.69	0.77	0.71	0.64	0.44
Al2O3	15.75	19.23	17.56	14.91	11.08
FeO*	4.07	5.75	9.14	4.91	7.64
MnO	0.13	0.02	0.03	0.01	0.02
MgO	1.98	1.52	1.49	1.45	1.13
CaO	23.40	0.56	0.76	1.86	12.30
Na2O	0.44	0.51	0.45	0.55	0.52
K2O	3.64	4.55	4.09	3.70	2.98
P2O5	0.16	0.07	0.09	0.13	0.11
Total	100.00	100.00	100.00	100.00	100.00

Table 3.4: Trace Elements (ppm)

	Tully	Mah	Marc Top	Marc Mid	Lower Marc
	M-7200	**M-7440**	**M-7451.5**	**M-7509**	**M-7543**
Ni	26	238	48	53	126
Cr	70	100	73	60	59
Sc	11	18	17	16	18
V	117	417	288	441	786
Ba	721	1097	992	930	1046
Rb	128	192	165	134	89
Sr	246	130	112	125	353
Zr	96	116	108	112	77
Y	19	29	26	57	65
Nb	10.0	13.0	11.6	10.9	6.7
Ga	17	23	20	18	14
Cu	15	128	35	27	67
Zn	29	295	113	387	300
Pb	10	7	14	2	2
La	29	35	33	30	40
Ce	58	71	64	68	64
Th	8	12	10	7	6
Nd	25	34	30	40	42
U	4	9	6	64	68
sum tr.	1641	2962	2167	2584	3228
in %	0.16	0.30	0.22	0.26	0.32
sum m+tr	82.22	89.71	87.38	81.14	75.81
M+Toxides	82.25	89.77	87.43	81.20	75.89
w/LOI	99.11	99.58	99.08	99.29	95.36
if Fe3+	99.48	100.15	99.96	99.73	96.00

Major and trace element data for the MSEEL MIP-3H samples will complement ongoing studies that involve interpreting the distribution of elements among individual mineral and organic matter (OM) constituents. For example, energy dispersive X-ray spectroscopy (EDS) and QEMSCAN mineral mapping show clay and silt-sized barite in fine-grained matrix lamellae of organic-rich Lower Marcellus. Combining elemental measurements at the bulk rock (several

grams for XRF) and the microtextural (thin section, 1 to 10s of microns) scales can help inform studies involving fluid rock interactions.

Darrah's Lab (OSU)

Milestone 1: Characterization of remaining water and gas samples for noble gas (He, Ne, Ar, Kr, and Xe), fixed gas (N_2, H_2, CO_2) and hydrocarbon gas (C1-C5, C6+) composition (11 samples remain).

Deliverable: Data report for remaining noble gas, hydrocarbon, and fixed gas measurements.

Table 3.5: Samples Analyzed to Date.

Sample Name	Sample Type	Analyzed		Sample Name	Sample Type	Analyzed
MIP 3H 12/14/15	GAS	YES		MIP-6H-072915	WATER	YES
3H 12/13/15 8:30am	GAS	YES		MIP-4H-072915 RAD	WATER	YES
MIP 5H 02/17/2016	GAS	YES		MIP 3H input (river) H2O 11-11-15 RAD	WATER	YES
5H 12/22/15 9:00am	GAS	YES		MIP 5H 121015 RAD	WATER	YES
MIP 3H 02/17/2016	GAS	YES		MIP 3H - 121015 RAD	WATER	YES
3H 12/22/15 9:00am	GAS	YES		MIP 5H 121115 8 PM	WATER	YES
MIP 4H dup 9/9/15	GAS	YES		MIP 3H 121115 RAD	WATER	YES
MIP 6H 9/9/15	GAS	YES		MIP 3H - 121215 RAD	WATER	YES
3H 1/14/2016	GAS	YES		MIP 5H - 121215 RAD	WATER	YES
MIP 4H 9/9/15	GAS	YES		MIP 3H - 12-13-15 RAD	WATER	YES
MIP 5H 12/11/15 8:30am	GAS	YES		MIP 3H - 121415 RAD	WATER	YES
MIP 5H 12/10/15 9pm	GAS	YES		MIP 3H - 121515 RAD	WATER	YES
MIP 3H 12/11/15 8pm	GAS	YES		MIP 3H - 121615 RAD	WATER	YES
MIP 5H 12/11/15 8pm	GAS	YES		MIP 5H - 121815 RAD	WATER	YES
MIP 3H 12/11/15 8pm	GAS	YES		MIP 3H - 121815 RAD	WATER	YES
5H 12/11/15 2pm	GAS	YES		MIP 3H - 121915 RAD	WATER	YES
MIP 3H 12/11/15 8:15am	GAS	YES		MIP 5H - 121915 RAD	WATER	YES
MIP 3H 03/02/16	GAS	YES		MIP 3H - 122015 RAD	WATER	YES
MIP 5H 03/02/16	GAS	YES		MIP 3H - 122115 RAD	WATER	YES
MIP 5H 02/03/16	GAS	YES		MIP 5H - 122115 RAD	WATER	YES
MIP 3H 02/03/16	GAS	YES		MIP 3H - 122215 RAD	WATER	YES
3H 4/6/16	GAS	YES		MIP 5H - 122215 RAD	WATER	YES
5H 4/6/16	GAS	YES		MIP 3H - 011416 RAD	WATER	YES
5H 01/14/16	GAS	YES		MIP 5H -011416 RAD	WATER	YES
MIP 6H dup 9/9/15	GAS	YES		MIP 5H 020316 RAD	WATER	YES
5H 11/16/15	GAS	YES		MIP 3H 020316 RAD	WATER	YES
MIP 5H 121215 8:15AM	GAS	YES		MIP 3H - 021716 RAD	WATER	YES
3H 12-19-15 9 AM	GAS	YES		MIP 5H - 021716 RAD	WATER	YES
5H 12-19-15 9 AM	GAS	YES		MIP 5H 03-02-16	WATER	YES
3H July 13, 2016	GAS	YES		MIP 3H 040616 RAD	WATER	YES
5H July 13, 2016	GAS	YES		MIP 3H 040616 RAD	WATER	YES
5H 1/18/17	GAS	YES		MIP 3H - 060816 RAD	WATER	YES
3H 1/18/2017	GAS	YES		MIP 5H - 060816 RAD	WATER	YES
3H 03/15/17	GAS	YES		MIP 3H - 071316 - Raw AJH	WATER	YES
5H 03/15/17	GAS	YES		MIP 5H - 071316 - Raw AJH	WATER	YES
3H 091416	GAS	YES		MIP 3H - 091416 AJH Raw	WATER	YES
5H 091416	GAS	YES		MIP 5H - 091416 Raw AJH	WATER	YES
3H 060816	GAS	YES		MIP-5H-111616 AJH	WATER	YES
5H 060816	GAS	YES		MIP-6H-011817 AJH	WATER	YES
				MIP-4H-011817 AJH	WATER	YES
				MIP 3H 1-18-17	WATER	YES
				MIP-3H-031517 AJH Raw	WATER	YES
				MIP-5H-031517 AJH	WATER	YES
				MIP-3H-041217 AJH	WATER	YES
				MIP 5H 11-16-16 AJH	WATER	YES
				MIP - field blank 122215 RAD	WATER	YES
				He-1176 3H 4/6/16	WATER	YES, Need to Process
				He-1177 5H 4/6/16	WATER	YES, Need to Process
				He-1178 5H 01/14/16	WATER	YES, Need to Process
				He-1180 MIP 6H dup 9/9/15	WATER	YES, Need to Process

Table 3.6: Major and Noble Gas Compositional Data.

	CH_4 ccSTP/cc	C_2H_6 ccSTP/cc	C3 ccSTP/cc	Ci-4 ccSTP/cc	Cn-4 ccSTP/cc	Ci-5 ccSTP/cc	C-5 ccSTP/cc	C-6 ccSTP/cc	N_2 ccSTP/cc	O_2 ccSTP/cc
3H 03/15/17	0.913	3.07E-02	1.83E-03	3.70E-05	1.33E-04	9.74E-06	1.08E-05	3.00E-06	0.04	b.d.l.
3H 091416	0.916	3.03E-02	1.80E-03	3.73E-05	1.31E-04	9.25E-06	8.38E-06	2.44E-06	0.04	b.d.l.
3H 1/18/2017	0.921	2.79E-02	1.64E-03	3.53E-05	1.20E-04	6.43E-06	9.26E-06	2.36E-06	0.04	b.d.l.
3H 12-19-15 9 AM	0.946	8.86E-03	6.59E-04	3.70E-04	5.72E-04	2.55E-04	1.90E-04	8.03E-05	0.03	b.d.l.
3H 4/6/16	0.948	1.10E-02	5.90E-04	2.31E-05	0.00E+00	3.58E-04	1.05E-03	0.00E+00	0.03	b.d.l.
3H July 13, 2016	0.901	1.73E-02	7.66E-03	3.64E-03	4.27E-03	1.72E-03	1.53E-03	8.49E-04	0.03	b.d.l.
5H 01/14/16	0.926	1.03E-02	5.17E-04	0.00E+00	1.06E-04	3.78E-04	7.22E-04	8.88E-05	0.03	b.d.l.
5H 03/15/17	0.910	3.09E-02	1.85E-03	3.87E-05	1.36E-04	1.00E-05	7.66E-06	2.36E-06	0.04	b.d.l.
5H 060816	0.928	2.67E-02	1.48E-03	2.66E-05	1.01E-04	2.02E-05	1.27E-05	4.11E-06	0.04	b.d.l.
5H 091416	0.929	2.55E-02	1.36E-03	2.77E-05	9.45E-05	1.23E-05	1.62E-05	3.59E-06	0.04	b.d.l.
5H 1/18/17	0.953	1.30E-02	1.35E-03	4.33E-04	4.94E-04	3.27E-04	2.89E-04	1.13E-04	0.04	b.d.l.
5H 11/16/15	0.932	1.03E-02	5.39E-04	0.00E+00	9.19E-05	3.40E-04	0.00E+00	9.75E-05	0.04	b.d.l.
5H 12-19-15 9 AM	0.935	1.02E-02	5.55E-04	6.94E-05	9.24E-05	6.03E-04	1.49E-03	7.93E-05	0.04	b.d.l.
5H 4/6/16	0.943	9.99E-03	5.04E-04	0.00E+00	0.00E+00	4.76E-04	3.12E-04	0.00E+00	0.03	b.d.l.
5H July 13, 2016	0.934	1.07E-02	5.66E-04	0.00E+00	0.00E+00	1.32E-03	5.49E-04	7.87E-05	0.04	b.d.l.
MIP 3H - 011416 RAD	0.922	1.02E-02	5.15E-04	0.00E+00	1.06E-04	3.76E-04	7.18E-04	8.84E-05	0.03	b.d.l.
MIP 3H - 121815 RAD	0.932	2.42E-02	1.29E-03	2.01E-05	8.40E-05	2.51E-05	4.74E-05	5.75E-05	0.04	b.d.l.
MIP 3H - 121915 RAD	0.930	2.59E-02	1.39E-03	2.22E-05	8.91E-05	5.27E-06	1.26E-05	3.99E-06	0.04	b.d.l.
MIP 3H - 122015 RAD	0.951	9.07E-03	4.80E-04	1.60E-04	1.68E-04	1.42E-04	8.81E-05	6.43E-05	0.03	b.d.l.
MIP 3H - 122215 RAD	0.944	1.09E-02	5.87E-04	2.30E-05	0.00E+00	3.56E-04	1.05E-03	0.00E+00	0.03	b.d.l.
MIP 3H 02/03/16	0.933	1.05E-02	5.57E-04	0.00E+00	1.28E-04	1.77E-04	2.78E-04	6.41E-05	0.04	b.d.l.
MIP 5H - 121815 RAD	0.935	2.43E-02	1.32E-03	2.38E-05	8.83E-05	1.74E-05	1.05E-05	1.75E-05	0.04	b.d.l.
MIP 5H - 121915 RAD	0.538	7.29E-03	1.55E-03	6.24E-04	6.19E-04	3.21E-04	3.87E-04	2.11E-04	0.40	0.04
MIP 5H - 122115 RAD	0.929	1.04E-02	5.55E-04	0.00E+00	1.27E-04	1.76E-04	2.77E-04	6.38E-05	0.04	b.d.l.
MIP 5H - 122215 RAD	0.939	9.94E-03	5.01E-04	0.00E+00	0.00E+00	4.73E-04	3.11E-04	0.00E+00	0.03	b.d.l.
MIP 5H -011416 RAD	0.940	9.91E-03	5.69E-04	7.18E-05	1.23E-04	1.58E-04	7.18E-05	6.85E-05	0.03	b.d.l.
MIP 5H 020316 RAD	0.928	1.02E-02	5.36E-04	0.00E+00	9.14E-05	3.39E-04	0.00E+00	9.70E-05	0.04	b.d.l.
MIP 5H 121215 8:15AM	0.935	9.12E-03	1.43E-03	8.88E-04	8.53E-04	5.46E-04	3.75E-04	3.74E-04	0.03	b.d.l.
MIP 6H dup 9/9/15	0.944	9.96E-03	5.72E-04	7.21E-05	1.24E-04	1.58E-04	7.21E-05	6.88E-05	0.03	b.d.l.

	CO ccSTP/cc	CO_2 ccSTP/cc	TOTAL	GROSS BTU (BEFORE CO_2 REMOVAL)	NET BTU (BEFORE CO_2 REMOVAL)	GROSS BTU (AFTER CO_2 REMOVAL)	NET BTU (AFTER CO_2 REMOVAL)	^3He pcc/cc	^4He µcc/cc	^{20}Ne µcc/cc
3H 03/15/17	b.d.l.	0.00	0.99	984.20	886.88	987.51	889.86	2.25	149.12	0.01
3H 091416	b.d.l.	0.00	0.99	986.01	888.50	989.21	891.38	2.10	137.98	0.02
3H 1/18/2017	b.d.l.	0.00	0.99	986.60	888.95	989.90	891.93	1.97	152.40	0.01
3H 12-19-15 9 AM	b.d.l.	0.02	1.01	979.26	881.88	995.51	896.52	2.19	136.31	0.04
3H 4/6/16	b.d.l.	0.01	1.01	984.68	886.83	996.01	897.03	2.52	149.78	0.01
3H July 13, 2016	b.d.l.	0.01	0.98	998.08	900.11	1008.14	909.18	2.21	164.35	0.01
5H 01/14/16	b.d.l.	0.02	1.00	960.49	865.01	983.26	885.51	2.71	153.56	0.01
5H 03/15/17	b.d.l.	0.00	0.99	981.24	884.22	984.61	887.25	1.54	143.91	0.01
5H 060816	b.d.l.	0.00	1.00	990.59	892.51	993.61	895.22	1.83	155.20	0.01

5H 091416	b.d.l.	0.00	1.00	989.11	891.14	992.00	893.74	1.94	150.45	0.01
5H 1/18/17	b.d.l.	0.00	1.01	995.51	896.67	1000.09	900.79	2.20	169.98	0.04
5H 11/16/15	b.d.l.	0.02	1.00	963.44	867.60	984.34	886.42	2.06	169.59	0.04
5H 12-19-15 9 AM	b.d.l.	0.02	1.00	972.20	875.63	989.33	891.05	1.92	158.03	0.01
5H 4/6/16	b.d.l.	0.02	1.00	974.98	877.99	992.12	893.43	2.73	163.10	0.00
5H July 13, 2016	b.d.l.	0.02	1.00	968.65	872.35	985.56	887.57	2.05	161.29	0.04
MIP 3H - 011416 RAD	b.d.l.	0.02	0.99	956.08	861.03	978.74	881.44	2.70	152.85	0.01
MIP 3H - 121815 RAD	b.d.l.	0.00	1.00	990.44	892.30	993.24	894.82	2.24	150.99	0.01
MIP 3H - 121915 RAD	b.d.l.	0.00	1.00	991.85	893.61	994.70	896.18	2.06	158.43	0.01
MIP 3H - 122015 RAD	b.d.l.	0.01	1.01	981.96	884.26	996.84	897.66	1.87	146.27	0.04
MIP 3H - 122215 RAD	b.d.l.	0.01	1.00	980.15	882.75	991.43	892.90	2.50	149.10	0.01
MIP 3H 02/03/16	b.d.l.	0.02	1.00	966.46	870.35	985.37	887.38	1.58	147.40	0.01
MIP 5H - 121815 RAD	b.d.l.	0.00	1.00	992.95	894.56	995.77	897.10	1.38	154.07	0.01
MIP 5H - 121915 RAD	b.d.l.	0.01	1.00	567.84	511.58	573.49	516.68	5.76	45.97	10.82
MIP 5H - 122115 RAD	b.d.l.	0.02	1.00	962.02	866.35	980.84	883.30	1.57	146.72	0.01
MIP 5H - 122215 RAD	b.d.l.	0.02	1.00	970.49	873.95	987.56	889.32	2.71	162.35	0.00
MIP 5H -011416 RAD	b.d.l.	0.02	1.00	971.17	874.56	987.67	889.42	1.72	157.66	0.01
MIP 5H 020316 RAD	b.d.l.	0.02	1.00	959.01	863.61	979.81	882.34	2.05	168.81	0.03
MIP 5H 121215 8:15AM	b.d.l.	0.02	1.00	974.76	877.99	994.03	895.34	2.67	158.92	0.02
MIP 6H dup 9/9/15	b.d.l.	0.02	1.01	975.66	878.60	992.24	893.53	1.73	158.39	0.01

	^{21}Ne µcc/cc	^{22}Ne µcc/cc	^{20}Ne ncc/cc	^{21}Ne ncc/cc	^{22}Ne ncc/cc	Ne µcc/cc	^{36}Ar µcc/cc	^{38}Ar µcc/cc	Ar µcc/cc	^{84}Kr ncc/cc
3H 03/15/17	0.00	0.00	9.26	0.03	0.88	0.01	0.04	0.01	16.83	0.08
3H 091416	0.00	0.00	17.22	0.05	1.78	0.02	0.06	0.01	22.07	0.03
3H 1/18/2017	0.00	0.00	8.87	0.03	0.88	0.01	0.05	0.01	18.35	0.04
3H 12-19-15 9 AM	0.00	0.00	36.60	0.12	3.81	0.04	0.04	0.01	15.27	0.03
3H 4/6/16	0.00	0.00	9.02	0.03	0.86	0.01	0.04	0.01	15.33	0.19
3H July 13, 2016	0.00	0.00	9.48	0.03	0.88	0.01	0.03	0.01	11.83	0.01
5H 01/14/16	0.00	0.00	8.99	0.03	0.86	0.01	0.03	0.01	13.49	0.20
5H 03/15/17	0.00	0.00	9.86	0.03	0.90	0.01	0.06	0.01	22.70	0.03
5H 060816	0.00	0.00	9.66	0.03	0.92	0.01	0.04	0.01	16.78	0.03
5H 091416	0.00	0.00	6.92	0.03	0.70	0.01	0.04	0.01	18.22	0.04
5H 1/18/17	0.00	0.00	38.13	0.11	3.96	0.04	0.08	0.02	24.58	0.06
5H 11/16/15	0.00	0.00	35.14	0.11	3.63	0.04	0.05	0.01	18.12	0.03
5H 12-19-15 9 AM	0.00	0.00	8.51	0.03	0.77	0.01	0.04	0.01	14.37	0.02
5H 4/6/16	0.00	0.00	4.70	0.02	0.42	0.01	0.02	0.00	10.47	0.02
5H July 13, 2016	0.00	0.00	43.25	0.13	4.52	0.05	0.07	0.01	24.10	0.03
MIP 3H - 011416 RAD	0.00	0.00	8.95	0.03	0.85	0.01	0.03	0.01	13.43	0.20
MIP 3H - 121815 RAD	0.00	0.00	10.28	0.03	0.95	0.01	0.05	0.01	19.24	0.04
MIP 3H - 121915 RAD	0.00	0.00	6.82	0.02	0.67	0.01	0.04	0.01	15.50	0.02
MIP 3H - 122015 RAD	0.00	0.00	40.42	0.12	4.12	0.04	0.05	0.01	17.46	0.02
MIP 3H - 122215 RAD	0.00	0.00	8.98	0.03	0.86	0.01	0.04	0.01	15.26	0.18
MIP 3H 02/03/16	0.00	0.00	5.82	0.02	0.51	0.01	0.03	0.01	13.86	0.21
MIP 5H - 121815 RAD	0.00	0.00	9.44	0.03	0.94	0.01	0.04	0.01	16.44	0.04

MIP 5H - 121915 RAD	0.03	1.11	10816.53	31.96	1105.93	11.95	11.90	2.26	3533.01	28.21
MIP 5H - 122115 RAD	0.00	0.00	5.80	0.02	0.51	0.01	0.03	0.01	13.80	0.21
MIP 5H - 122215 RAD	0.00	0.00	4.68	0.02	0.42	0.01	0.02	0.00	10.42	0.02
MIP 5H -011416 RAD	0.00	0.00	5.99	0.02	0.52	0.01	0.03	0.01	12.23	0.02
MIP 5H 020316 RAD	0.00	0.00	34.98	0.11	3.62	0.04	0.05	0.01	18.04	0.03
MIP 5H 121215 8:15AM	0.00	0.00	19.87	0.06	1.91	0.02	0.03	0.01	12.56	0.02
MIP 6H dup 9/9/15	0.00	0.00	6.02	0.02	0.53	0.01	0.03	0.01	12.29	0.02

	^{40}Ar µcc/cc	Kr ncc/cc	^{132}Xe ncc/cc	Xe ncc/cc	R/R_A	R_C/R_A	(He/Ne)	$(He/Ne)_{AIR}$	$\frac{^{20}Ne}{^{22}Ne}$	$\frac{^{21}Ne}{^{22}Ne}$
3H 03/15/17	16.78	0.14	0.00	0.01	0.01	0.01	14600.00	63478.26	10.53	0.03
3H 091416	22.00	0.05	0.00	0.02	0.01	0.01	7210.65	31350.63	9.64	0.03
3H 1/18/2017	18.29	0.07	0.00	0.02	0.01	0.01	15510.97	67438.98	10.08	0.03
3H 12-19-15 9 AM	15.22	0.05	0.00	0.01	0.01	0.01	3347.45	14554.13	9.56	0.03
3H 4/6/16	15.28	0.33	0.02	0.08	0.01	0.01	15041.73	65398.85	10.41	0.03
3H July 13, 2016	11.79	0.02	0.00	0.01	0.01	0.01	15747.01	68465.24	10.73	0.03
5H 01/14/16	13.45	0.36	0.01	0.06	0.01	0.01	15481.29	67309.96	10.43	0.03
5H 03/15/17	22.62	0.06	0.01	0.02	0.01	0.01	13283.70	57755.20	10.90	0.03
5H 060816	16.73	0.05	0.00	0.01	0.01	0.01	14557.62	63293.99	10.48	0.03
5H 091416	18.17	0.08	0.00	0.02	0.01	0.01	19595.20	85196.53	9.83	0.04
5H 1/18/17	24.49	0.10	0.01	0.02	0.01	0.01	4009.84	17434.07	9.59	0.03
5H 11/16/15	18.06	0.05	0.00	0.01	0.01	0.01	4341.24	18874.96	9.63	0.03
5H 12-19-15 9 AM	14.32	0.03	0.00	0.01	0.01	0.01	16899.80	73477.40	11.03	0.04
5H 4/6/16	10.44	0.03	0.00	0.01	0.01	0.01	31595.49	137371.71	11.01	0.04
5H July 13, 2016	24.01	0.05	0.01	0.02	0.01	0.01	3351.82	14573.13	9.52	0.03
MIP 3H - 011416 RAD	13.38	0.36	0.01	0.06	0.01	0.01	15410.08	67000.34	10.39	0.03
MIP 3H - 121815 RAD	19.18	0.08	0.00	0.01	0.01	0.01	13354.59	58063.44	10.80	0.03
MIP 3H - 121915 RAD	15.45	0.03	0.00	0.01	0.01	0.01	20991.14	91265.82	10.14	0.03
MIP 3H - 122015 RAD	17.40	0.03	0.00	0.02	0.01	0.01	3259.86	14173.33	9.77	0.03
MIP 3H - 122215 RAD	15.21	0.32	0.02	0.08	0.01	0.01	14972.54	65098.01	10.36	0.03
MIP 3H 02/03/16	13.82	0.37	0.02	0.07	0.01	0.01	23083.15	100361.50	11.28	0.04
MIP 5H - 121815 RAD	16.38	0.07	0.00	0.02	0.01	0.01	14725.07	64022.05	10.02	0.03
MIP 5H - 121915 RAD	3518.85	49.58	1.57	5.85	0.09	0.03	3.83	16.64	9.74	0.03
MIP 5H - 122115 RAD	13.76	0.37	0.02	0.07	0.01	0.01	22976.96	99899.84	11.23	0.04
MIP 5H - 122215 RAD	10.39	0.03	0.00	0.01	0.01	0.01	31450.15	136739.80	10.96	0.04
MIP 5H -011416 RAD	12.19	0.04	0.00	0.01	0.01	0.01	23910.51	103958.72	11.32	0.04
MIP 5H 020316 RAD	17.97	0.05	0.00	0.01	0.01	0.01	4321.27	18788.14	9.59	0.03
MIP 5H 121215 8:15AM	12.52	0.04	0.00	0.01	0.01	0.01	7241.94	31486.71	10.35	0.03
MIP 6H dup 9/9/15	12.25	0.04	0.00	0.01	0.01	0.01	24021.00	104439.14	11.38	0.04

	$\frac{^{38}Ar}{^{36}Ar}$	$\frac{^{40}Ar}{^{36}Ar}$	$\frac{^{4}He}{^{20}Ne}$	$\frac{^{20}Ne}{^{36}Ar}$	$\frac{^{4}He}{^{36}Ar}$	$\frac{^{84}Kr}{^{36}Ar}$	$\frac{^{132}Xe}{^{84}Kr}$	$\frac{^{4}He}{^{21}Ne^*}$	$\frac{^{4}He}{^{40}Ar^*}$	$\frac{CO_2}{^{3}He}$
3H 03/15/17	0.20	376.97	16024.88	0.21	3350.43	0.00	0.05	48.07	40.27	3.34E+09
3H 091416	0.19	348.40	7976.83	0.27	2185.39	0.00	0.16	-349.83	40.09	3.22E+09
3H 1/18/2017	0.19	366.69	17093.77	0.18	3055.89	0.00	0.11	36.23	41.93	3.32E+09
3H 12-19-15 9 AM	0.19	343.03	3706.65	0.83	3072.56	0.00	0.11	22.53	62.56	1.62E+10

3H 4/6/16	0.19	395.75	16528.34	0.23	3878.42	0.00	0.12	36.94	38.00	1.13E+10
3H July 13, 2016	0.19	354.74	17256.28	0.29	4945.36	0.00	0.29	39.19	81.24	9.94E+09
5H 01/14/16	0.19	383.79	17007.41	0.26	4382.96	0.01	0.07	40.76	48.67	2.30E+10
5H 03/15/17	0.19	362.68	14533.99	0.16	2307.18	0.00	0.15	103.54	33.51	3.40E+09
5H 060816	0.19	382.43	15989.22	0.22	3548.15	0.00	0.14	27.88	40.00	3.02E+09
5H 091416	0.19	405.48	21650.48	0.15	3357.27	0.00	0.09	28.91	30.02	2.90E+09
5H 1/18/17	0.20	317.14	4437.92	0.49	2201.39	0.00	0.11	251.24	95.26	4.56E+09
5H 11/16/15	0.20	334.14	4803.35	0.65	3138.35	0.00	0.11	42.07	78.11	2.11E+10
5H 12-19-15 9 AM	0.19	385.17	18478.29	0.23	4249.14	0.00	0.19	31.53	46.47	1.72E+10
5H 4/6/16	0.20	438.79	34557.75	0.20	6856.67	0.00	0.13	44.76	47.18	1.72E+10
5H July 13, 2016	0.20	319.08	3712.32	0.57	2143.53	0.00	0.20	-50.55	85.55	1.71E+10
MIP 3H - 011416 RAD	0.19	382.02	16929.17	0.26	4362.80	0.01	0.07	40.58	48.44	2.29E+10
MIP 3H - 121815 RAD	0.19	349.32	14625.15	0.19	2750.56	0.00	0.08	42.55	49.62	2.80E+09
MIP 3H - 121915 RAD	0.19	390.64	23116.04	0.17	4006.24	0.00	0.19	84.60	41.33	2.85E+09
MIP 3H - 122015 RAD	0.19	320.47	3602.02	0.74	2694.12	0.00	0.21	40.08	101.84	1.49E+10
MIP 3H - 122215 RAD	0.19	393.93	16452.31	0.23	3860.58	0.00	0.12	36.77	37.82	1.13E+10
MIP 3H 02/03/16	0.20	416.18	25199.53	0.18	4437.33	0.01	0.09	27.29	36.19	1.91E+10
MIP 5H - 121815 RAD	0.19	375.22	16237.03	0.22	3528.31	0.00	0.10	35.86	43.32	2.82E+09
MIP 5H - 121915 RAD	0.19	294.22	4.23	0.90	3.84	0.00	0.06	59.10	49.27	9.82E+09
MIP 5H - 122115 RAD	0.19	414.27	25083.61	0.17	4416.92	0.01	0.09	27.16	36.03	1.90E+10
MIP 5H - 122215 RAD	0.20	436.77	34398.78	0.20	6825.13	0.00	0.13	44.55	46.97	1.71E+10
MIP 5H -011416 RAD	0.19	406.18	26079.55	0.20	5251.75	0.00	0.13	37.80	45.89	1.66E+10
MIP 5H 020316 RAD	0.20	332.60	4781.25	0.65	3123.91	0.00	0.11	41.88	77.75	2.10E+10
MIP 5H 121215 8:15AM	0.19	370.23	7959.24	0.59	4697.87	0.00	0.14	62.55	61.46	1.93E+10
MIP 6H dup 9/9/15	0.19	408.06	26200.07	0.20	5276.02	0.00	0.13	37.97	46.10	1.66E+10

	CH_4 / ^3He	CH_4 / ^4He	^4He / CH_4	CH_4 / ^{36}Ar	N_2 / Ar	CH_4 / C_2H_6+	CH_4 / CO_2
3H 03/15/17	4.05E+11	6.10E+03	1.63E+02	2.05E+07	2.34E+02	27.77	272.12
3H 091416	4.33E+11	6.61E+03	1.50E+02	1.45E+07	1.72E+02	28.22	283.25
3H 1/18/2017	4.65E+11	6.02E+03	1.65E+02	1.85E+07	2.11E+02	30.89	275.80
3H 12-19-15 9 AM	4.30E+11	6.91E+03	1.43E+02	2.13E+07	2.03E+02	85.74	57.96
3H 4/6/16	3.75E+11	6.30E+03	1.57E+02	2.45E+07	2.25E+02	72.65	83.37
3H July 13, 2016	4.06E+11	5.46E+03	1.82E+02	2.71E+07	2.47E+02	24.25	90.24
5H 01/14/16	3.40E+11	6.00E+03	1.65E+02	2.64E+07	2.57E+02	76.43	40.00
5H 03/15/17	5.86E+11	6.29E+03	1.57E+02	1.46E+07	1.85E+02	27.53	266.15
5H 060816	5.06E+11	5.95E+03	1.67E+02	2.12E+07	2.13E+02	32.52	306.08
5H 091416	4.77E+11	6.14E+03	1.61E+02	2.07E+07	2.10E+02	34.23	318.77
5H 1/18/17	4.32E+11	5.58E+03	1.78E+02	1.23E+07	1.49E+02	59.17	208.09
5H 11/16/15	4.50E+11	5.47E+03	1.81E+02	1.72E+07	1.93E+02	81.73	43.90
5H 12-19-15 9 AM	4.84E+11	5.89E+03	1.68E+02	2.51E+07	2.51E+02	71.21	54.00
5H 4/6/16	3.44E+11	5.76E+03	1.72E+02	3.97E+07	2.94E+02	83.23	54.58
5H July 13, 2016	4.53E+11	5.77E+03	1.72E+02	1.24E+07	1.48E+02	70.34	54.47
MIP 3H - 011416 RAD	3.38E+11	5.98E+03	1.64E+02	2.63E+07	2.56E+02	76.07	39.82
MIP 3H - 121815 RAD	4.14E+11	6.15E+03	1.61E+02	1.70E+07	1.99E+02	36.14	331.30

MIP 3H - 121915 RAD	4.49E+11	5.85E+03	1.69E+02	2.35E+07	2.29E+02	33.73	324.76
MIP 3H - 122015 RAD	5.08E+11	6.47E+03	1.53E+02	1.75E+07	1.76E+02	93.05	63.73
MIP 3H - 122215 RAD	3.73E+11	6.27E+03	1.57E+02	2.44E+07	2.24E+02	72.32	82.99
MIP 3H 02/03/16	5.89E+11	6.30E+03	1.57E+02	2.81E+07	2.61E+02	79.68	48.64
MIP 5H - 121815 RAD	6.74E+11	6.04E+03	1.64E+02	2.14E+07	2.16E+02	36.09	329.64
MIP 5H - 121915 RAD	9.29E+10	1.16E+04	8.51E+01	4.50E+04	8.35E+01	48.69	54.54
MIP 5H - 122115 RAD	5.86E+11	6.27E+03	1.56E+02	2.80E+07	2.59E+02	79.31	48.41
MIP 5H - 122215 RAD	3.43E+11	5.73E+03	1.71E+02	3.95E+07	2.93E+02	82.85	54.33
MIP 5H -011416 RAD	5.40E+11	5.90E+03	1.66E+02	3.13E+07	2.63E+02	84.82	56.22
MIP 5H 020316 RAD	4.48E+11	5.44E+03	1.80E+02	1.72E+07	1.92E+02	81.35	43.70
MIP 5H 121215 8:15AM	3.49E+11	5.86E+03	1.69E+02	2.76E+07	2.42E+02	68.50	48.23
MIP 6H dup 9/9/15	5.43E+11	5.93E+03	1.67E+02	3.14E+07	2.64E+02	85.21	56.48

Products

Sharma's Lab

1. Agrawal, V. & Sharma, S. 2018. Improved Kerogen models for determining hydrocarbon potential and thermal maturity of shales. *Scientific Reports* (in review)
2. Agrawal, V. & Sharma, S. 2018. Pitfalls in modeling physicochemical properties of Shale using kerogen type. Scientific Reports (in review)
3. Pilewski. J, Sharma, S., Agrawal, V., Hakala,A., Stuckman, M., 2018. Effect of Maturity and Mineralogy on Fluid-Rock reactions in the Marcellus Shale. Environmental Science: Processes & Impacts (in review)
4. Akondi R, Sharma S, Trexler R, Mouser PJ, Pfiffner SM, 2018. Microbial Lipid Biomarkers Detected in Deep Subsurface Black Shales *Environmental Science: Processes & Impacts*. (in review)
5. Agrawal, V., Sharma, S., 2018. New models for determining thermal maturity and hydrocarbon potential in Marcellus Shale. Eastern Section AAPG 47th Annual Meeting in Pittsburgh, WV

Wrighton's Lab (OSU-CSU); Wilkins Lab (OSU-CSU)

Daly RA, Roux S, Borton MA, Morgan DM, Johnston MD, Booker AE*, Hoyt DW, Meulia T, Wolfe RA, Hanson AJ, Mouser PJ, Sullivan MB, Wrighton KC, and **Wilkins MJ** (2018) Viruses control dominant bacteria colonizing the terrestrial deep biosphere after hydraulic fracturing. *Nature Microbiology*. Accepted.

Mouser's Lab

Peer Reviewed Publications associated with MSEEL:

1. Luek JL, Hari M, Schmitt-Kopplin P, **Mouser PJ,** Gonsior M. (2018). Organic sulfur fingerprint indicates continued injection fluid signature 10 months after hydraulic fracturing. *Environmental Science: Processes & Impacts*. Available in advance at doi: 10.1039/C8EM00331A.

Notes: The journal has chosen to highlight this paper on the back cover of their forthcoming volume. In addition, we are competing for the cover photo involving an MSEEL related photograph.

2. Evans MV, Panescu J, Hanson AJ, Sheets J, Welch SA, Nastasi N, Daly RA, Cole DR, Darrah TH Wilkins MJ, Wrighton KC, **Mouser PJ.** (*in press*, 2018), Influence of *Marinobacter* and *Arcobacter* taxa on system biogeochemistry during early production of hydraulically fractured shale gas wells in the Appalachian Basin. *Frontiers of Microbiology*.

Invited Seminars

1. *Tufts University, Dept. of Civil and Environmental Engineering*. Microbial Survival and Sustenance in Fractured Shale 10/2018.

2. *University of New Hampshire, Dept. of Earth Science*. Microbial Survival and Sustenance in Fractured Shale 09/2018.

Papers in Preparation

1. The following paper is currently under review:
Akondi R. Sharma S, Trexler R, Mouser PJ, Pfiffner S. Microbial Lipid Biomarkers Detected in Deep Subsurface Black Shales, Submitted to *Environmental Sciences: Processes & Impacts*.

Three more papers are in preparation that involve MSEEL related samples/topics and will be submitted in the next quarter.

Plan for Next Quarter

Sharma's Lab

Milestone 3: Researchers are in the process of extracting kerogen from all the shale samples used in these high P-T experiments to understand the effect on frac fluid interaction on kerogen molecular structure. They will develop schematic kerogen models to understand any change on interaction with fracturing fluids.

Milestone 4: Researchers are in the process of interpreting the results and preparing a manuscript.

Milestone 6: The manuscript summarizing results will be ready for submission to the *Frontiers in Microbiology* in the late phases of Fall 2018.

Wrighton's Lab (OSU-CSU); Wilkins Lab (OSU-CSU)

Milestone 1: This effort will compare the methane-generating *Methanohalophilus* strains across shales, many isolated from the MSEEL project. Genomics will be used to identify what makes persisting strains "unique" physiologically and then demonstrating this in the laboratory

Deliverable 1: A publication is being prepped, and is expected it to be submitted by the end of October. Borton (Wrighton) will lead this effort. Booker (Wilkins) will be a co-author, while Wrighton and Wilkins will be co-corresponding. MSEEL team members are co-authors.

Mouser's Lab (OSU-UNH)

Milestone 1: Characterization of intact polar lipids in MSEEL core and fluid samples

Deliverable 1: Complete publication associated with intact polar lipids. This manuscript is in the final stages of editing by corresponding author Mouser with Hanson first author. It will go out for co-author this quarter, with a target submission to *Nature Geoscience* or *Science*.

Milestone 2: Characterization of dehalogenation pathways in MSEEL fluid samples.

Deliverable 2: Complete publication associated with dehalogenation. Evans is currently working in the Wrighton lab to analyze metagenome data and reconstruct pathways. She will finalize a manuscript associated with this data during this quarter, corresponding author Mouser with Evans first author. Target submission will be December 2018.

Cole's Lab

Milestone 1: Complete analysis of trace metal composition of flowback fluid samples.

Deliverable 1: Compilation of the flowback fluid chemistry.

Deliverable 2: Produce a draft of a manuscript comparing geochemistry of flowback fluids between Utica and Marcellus wells.

Darrah's lab (OSU)

Milestone 1. Characterization of remaining mineral samples from cores.

Deliverable 1. Data report for remaining noble gas and hydrocarbon composition of fluid inclusions.

Milestone 2: Compile information for a publication from fluid (gas and water) samples through time.

Deliverable 2: Submit manuscript about changes in the hydrocarbon, fixed, and noble gas composition throughout time.

Topic 4 – Environmental Monitoring – Surface Water & Sludge

Approach

Almost three years into the post completion part of the program, the water and solid waste component of MSEEL has continued to systematically sample flowback and produced water volumes. During year one of the study, hydraulic fracturing fluid, flowback, produced water, drilling muds and drill cuttings were characterized by their inorganic, organic and radio chemistries. In addition, surface water in the nearby Monongahela River was monitored upstream and downstream of the MSEEL drill pad. Toxicity testing per EPA method 1311 (TCLP) was conducted on drill cuttings in both the vertical and horizontal (Marcellus) sections to evaluate their toxicity potential. Sampling frequency has been slowly scaled back following well development. Table shows an "X" for sample collection dates. Wells 4H and 6H were brought back online in late 2016. Other blank sample dates in Table indicate that samples were not collected, due to lack of availability of produced water from the well(s).

Table 4.1: MIP sampling events are indicated with an "X".

Year	2015			2016												
Day/Month	10-Dec	17-Dec	22-Dec	6-Jan	20-Jan	3-Feb	2-Mar	23-Mar	20-Apr	18-May	2-Jul	17-Aug	21-Jun	19-Oct	16-Nov	14-Dec
3H	X		X	X	X	X		X	X	X	X	X	X	X		X
4H															X	X
5H	X	X	X	X	X	X	X	X	X	X	X	X	X	X	X	
6H															X	X

Year	2017									2018			
Day/Month	13-Jan	14-Feb	13-Mar	7-Apr	5-May	12-Jul	20-Dec	3-Nov	20-Dec	22-Jan	23-Feb	16-May	2-Aug
3H	X	X	X	X	X	X	X	X	X	X	X	X	X
4H	X	X	X	X	X					X	X	X	X
5H		X			X				X	X		X	
6H	X	X	X	X	X							X	X

Results & Discussion

Trends in produced water chemistry

Major ions

While makeup water was characterized by low TDS (total dissolved solids) and a dominance of calcium and sulfate ions, produced water from initial flowback is essentially a sodium/calcium chloride water (Figure 4.1). Other than slight increases in the proportion of barium and strontium, the ionic composition of produced changed very little through 888 days post completion.

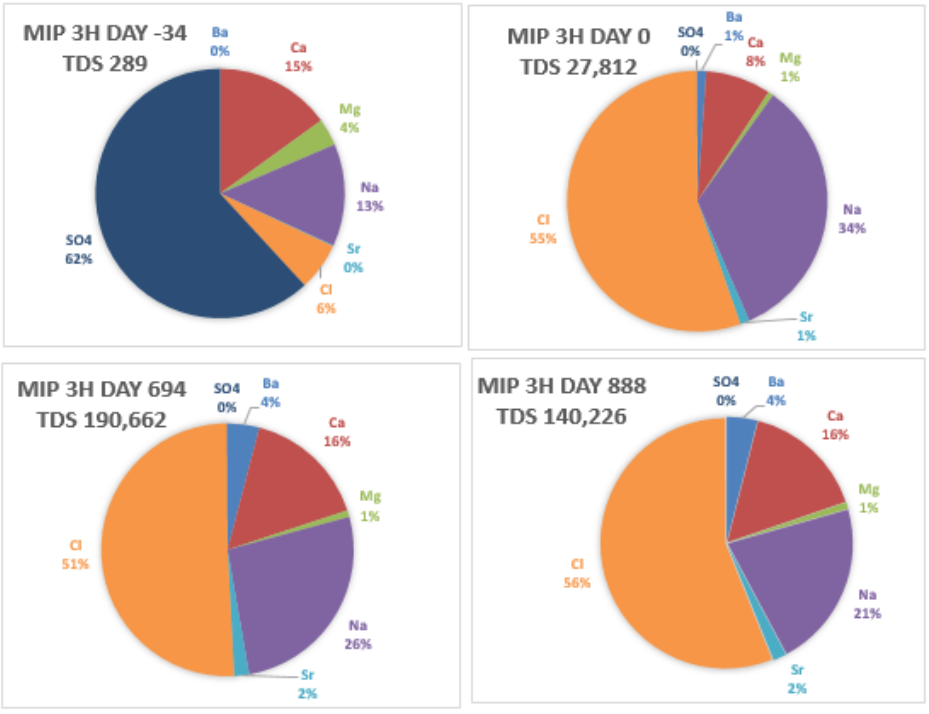

Figure 4.1: Changes in major ion concentrations in produced water from well MIP 3H. From left to right the charts represent makeup water from the Monongahela River, produced water on the first day of flowback and produced water on the 888th day post completion.

Regarding the newer wells at 3H and 5H, TDS increased rapidly over the initial 90 days post completion values had been consistently between 100,000 and 150,000 mg/L through day 966(3H), with a few outliers (Figure 4.2). Recent values indicate a downward trend at 3H.

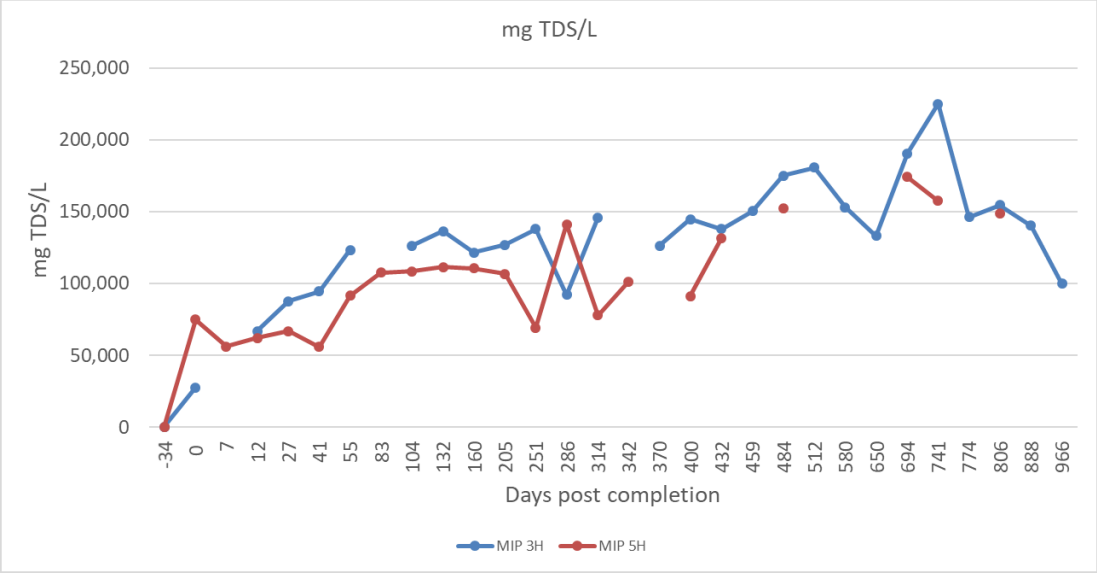

Figure 4.2. Changes in produced water TDS sdc (sum of dissolved constituents) through the first 966 days post completion (3,5H).

The older 4H and 6H wells offer insight into the longer-term TDS trend. Those wells only came back on line during this quarter after a shut-in period of 315 days and those results vary but they are much lower than the current values for wells MIP 3H and 5H. Both 4H and 6H were shut down during late 2017. TDS was very low at MIP 4H during the first sampling event of early 2018. Calculated TDS was 2,455 mg/L and lab reported TDS was 2,300 mg/L. A similar low TDS trend was noted when wells went back online around 1,793 days post-completion (after being shut-in for 315 days). A rise in TDS subsequently follows the initial return to online status with TDS on an upward trend, reaching around 140,000 for MIP 4H and 120,000 for 6H (Figure 4.3).

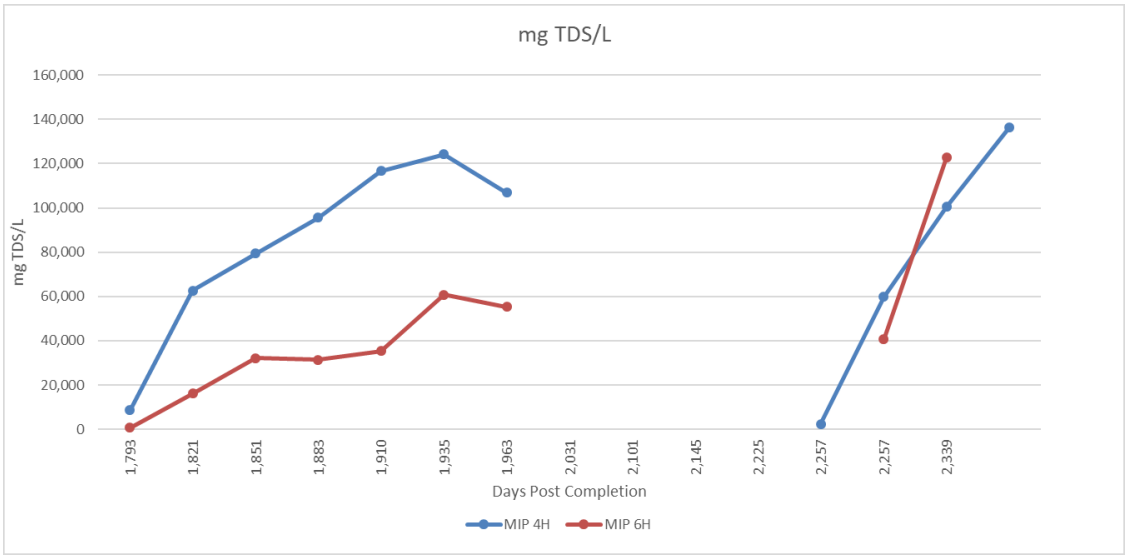

Figure 4.3: Changes in produced water TDS sdc (sum of dissolved constituents) through the days 1793 to 2417 post completion (4,6H).

Water soluble organics

The water soluble aromatic compounds in produced water: benzene, toluene, ethylbenzene and xylene were never high. With two exceptions at post completion day 321 and 694, benzene has remained below 30 µg/L (Figure 4) (we are awaiting confirmation from the analytical lab for this reported value of 41 µg/L for day 694). Apart from the spikes, this seems to be a characteristic of dry gas geologic units. After five years, benzene has declined below the drinking water standard of 5 µg/L.

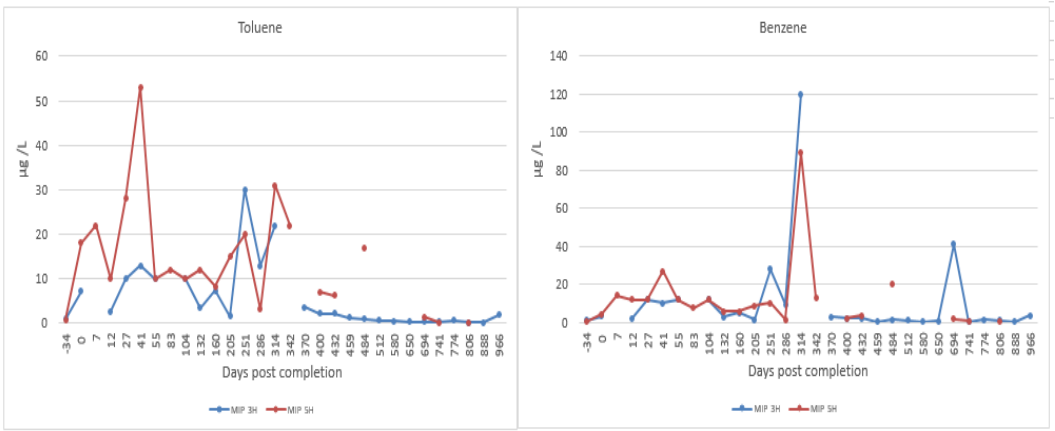

Figure 4.4: Changes in benzene and toluene concentrations. The figure shows data from well both 3H and 5H.

Radium isotopes

Radium concentrations generally increased through 800 days post completion at wells MIP 3H and 5H. Maximum levels of the radium isotopes reached about 20,000 pCi/L at the unchoked

3H well and about half that amount at 5H (Figure 4.5). Both wells appear to be on a downward trend post 800 days.

Radioactivity in produced water

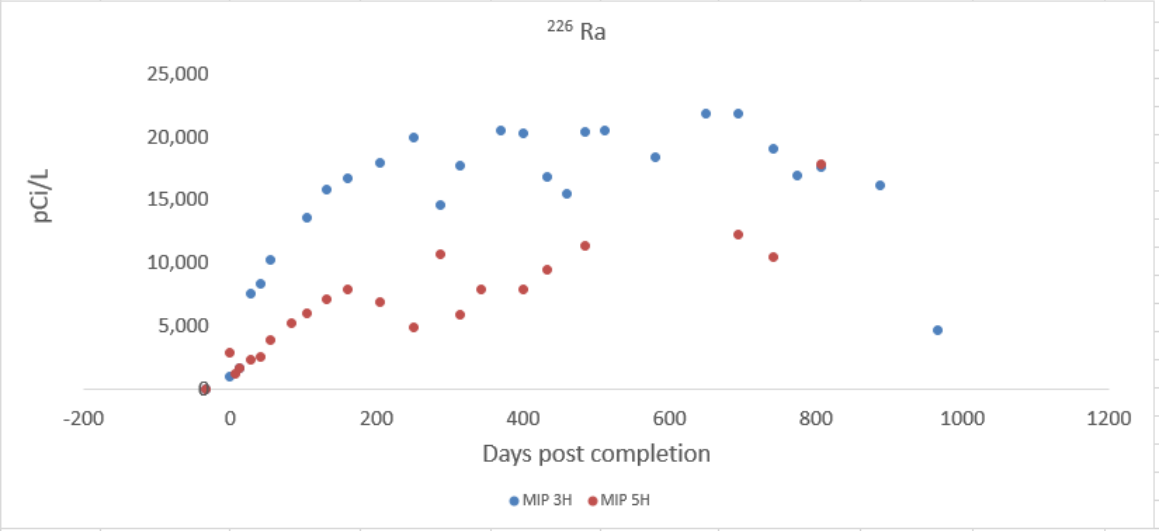

Figure 4.5: The radium isotopes are plotted against days post well completion. Well 5H was choked periodically. It produced less water and lower concentrations of radium.

Radium concentrations at wells 4H and 6H were below 9,000 pCi/L during all sampling periods. Both wells were choked at day 1963. Well 4H was reopened at day 2225, radium was 58 pCi/L on the first sampling after the reopening and 3719 pCi/L at day 2257, a month later (Figure 4.6) peaked at 5,127 pCi/L then returned to 3,892 pCi/L. Additional data is needed to capture long-term trends.

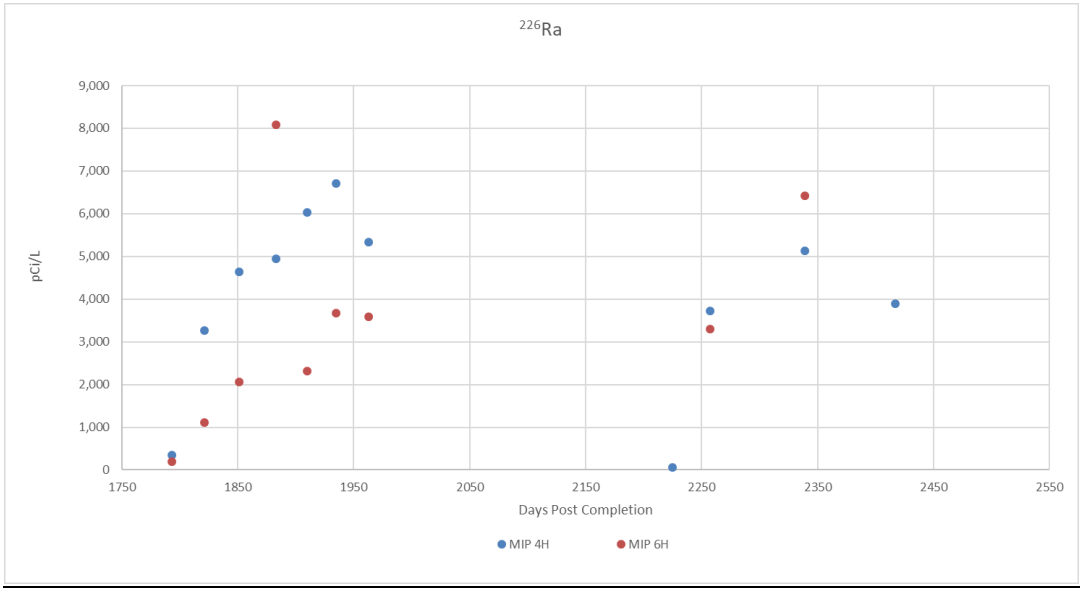

Figure 4.6: The radium isotopes are plotted against days post well completion. Well 4H and 6H were choked at day 1963. At day 2225, 4H was reopened showing a value of 58 pCi/L.

The radiochemical concentrations were determined by Pace Analytical in Greensburg PA, a state certified analytical lab. Figure 4.7 and 4.8 show the relationship between gross alpha and ^{226}Ra at 3H and 5H.

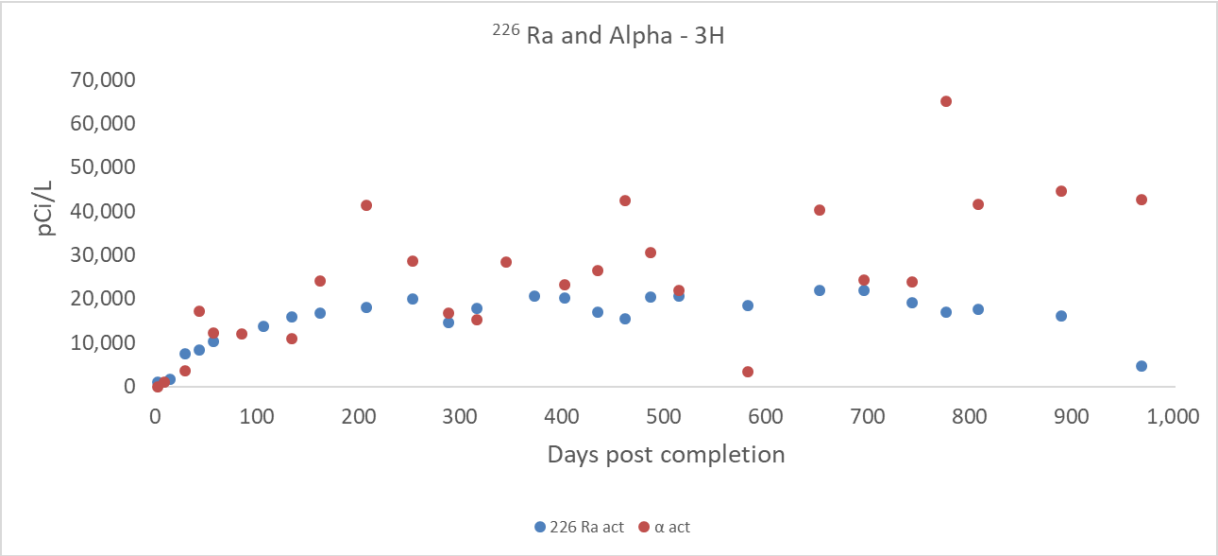

Figure 4.7: The relationship between gross alpha and 226Ra as a function of time post completion at 3H.

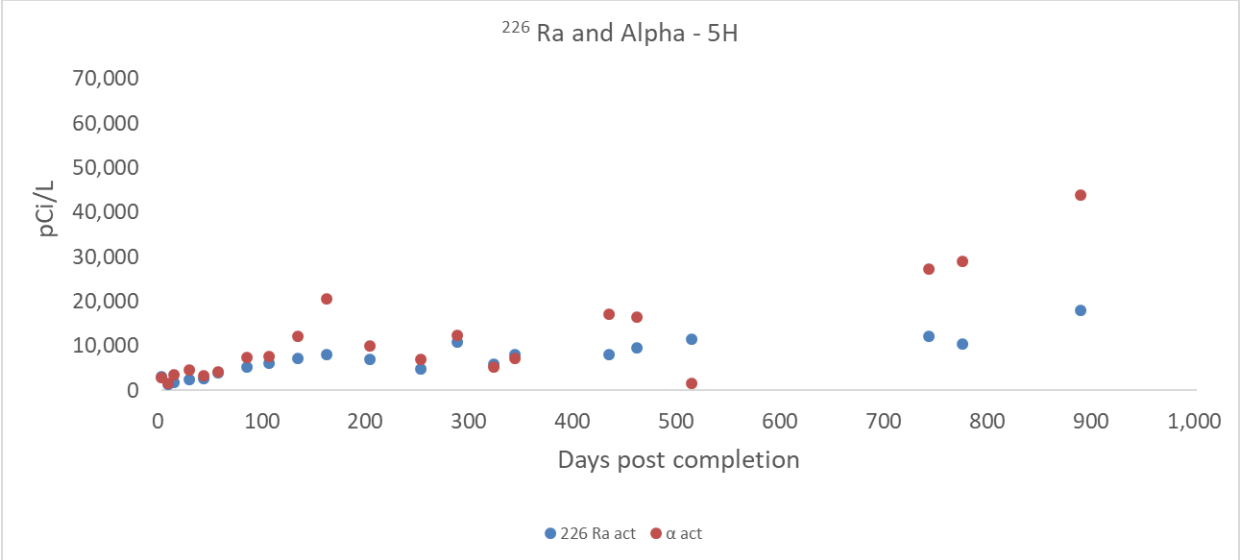

Figure 4.8: The relationship between gross alpha and 226Ra as a function of time post completion at 5H.

The highest values reported in the older wells at 4H and 6H were 15,080 pCi/L gross alpha and 8,078 pCi/L ^{226}Ra. The relationship between gross alpha and ^{226}Ra for wells 4H and 6H are shown in Figure 4.9 and 4.10.

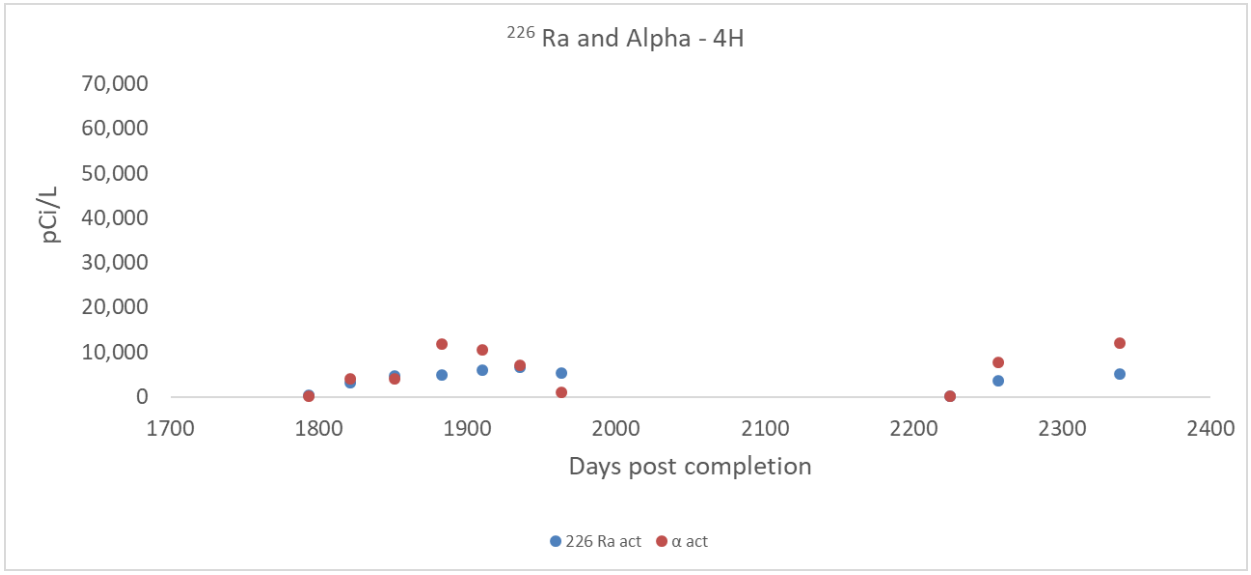

Figure 4.9: The relationship between gross alpha and 226Ra as a function of time post completion at 4H.

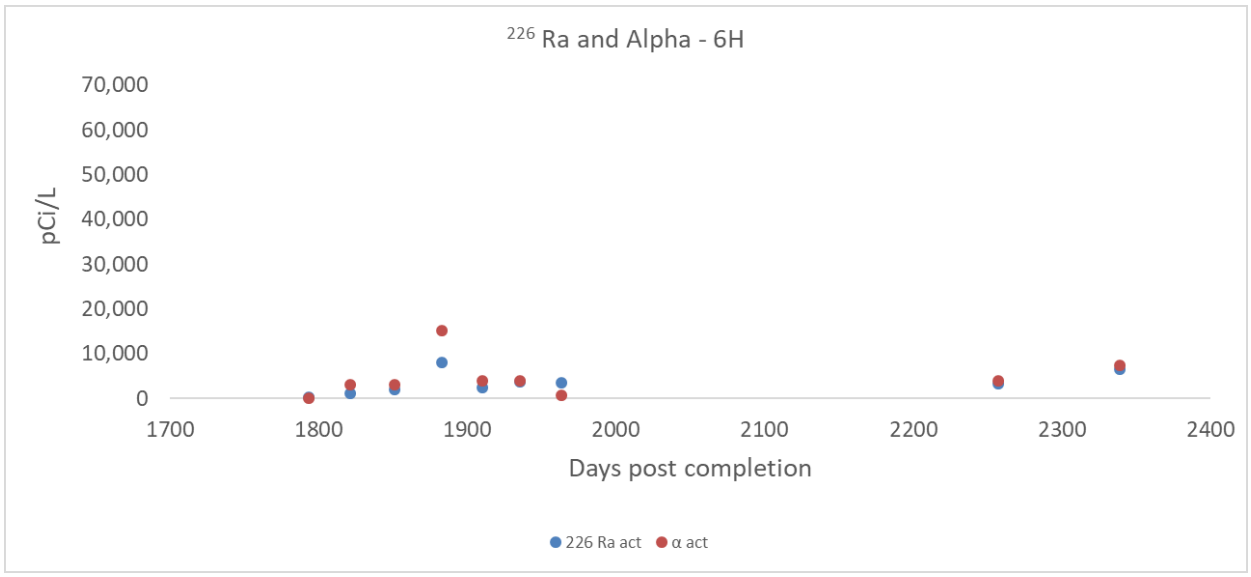

Figure 4.10: The relationship between gross alpha and 226Ra as a function of time post completion at 6H.

Products

None this quarter.

Plan for Next Quarter

Researchers will continue to sample and analyze flowback/produced water (FPW) from MIP 3H, 4H, 5H and 6H if they are online.

Topic 5 – Environmental Monitoring: Air & Vehicular

Approach

The WVU MAE team completed the sixth methane audit of the active MSEEL site. In addition, the team members held a kick-off meeting with colleagues for the additional work to be completed at MSEEL through the newly funded NSF project. As part of this project, the team will expand beyond direct quantification methods to examine indirect quantification schemes using a combination of Eddy Covariance and Gaussian Dispersion methods. As previously discussed, most of the required hardware is in-house and has been deployed in a mobile vehicle platform during the most recent audits. The most recent upwind and downwind data are presented in Figure 5.3. Researchers are currently designing and will then purchase a solar power system so that analyzers can be mounted at MSEEL for extended durations – before, during, and after audits. In discussions with NNE the system will likely be designed for mounting on an unused utility pole located at the edge of the well pad. Additional results and discussion follow.

Results & Discussion

The results from the sixth audit have been analyzed and are included in summary in Figure 5.1. As previously discussed, the researchers are working on a journal publication focused on examination of the temporal variability of methane emissions from the site. The total methane emissions were 106 grams per hour (g/hr). This was the second to lowest emissions rate to date and was similar to the emissions encountered in the previous July (Audit 3). The main source of variability in site emissions is due to the emissions from the uncontrolled produced water storage tank. Emissions from the water tank ranged from 22.5 g/hr during this audit to as high as 3731 g/hr during Audit 2. Multiple dump events from the separators occurred during Audit 2 and we will examine all variables to understand if there are any correlations between increased methane emissions and throughput, activity or other variables. Overall, the average MSEEL site emissions from all six audits were 1363 g/hr which is lower than the average emissions of Rella et. al. – 1740 g/hr.

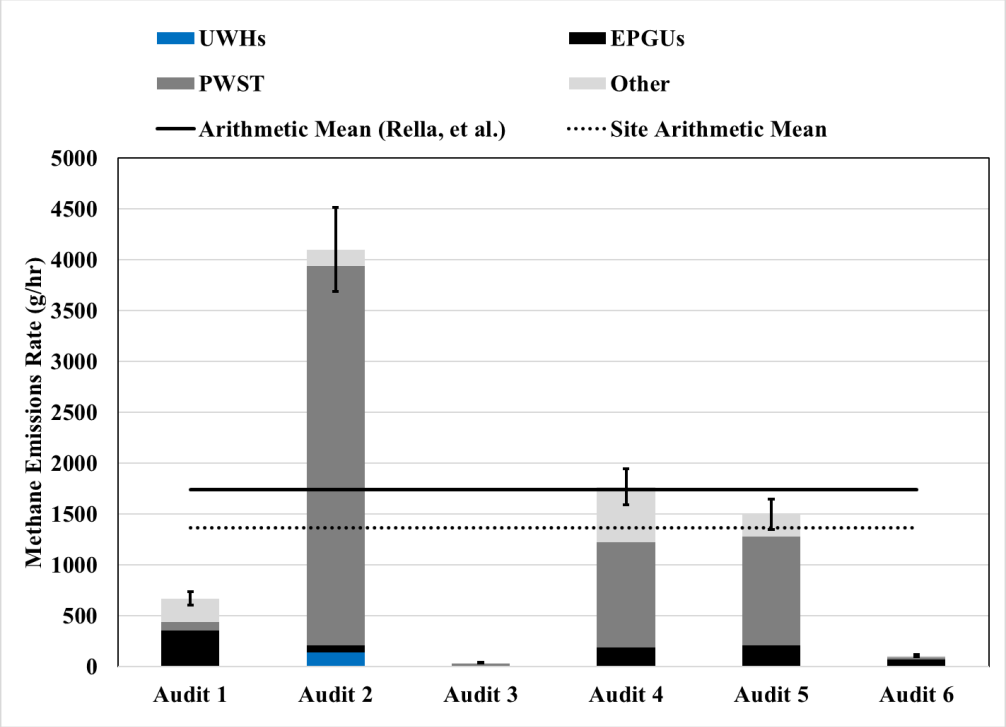

Figure 5.1: Summary of methane emissions from all six audits.

In addition to the direct quantification data, the research team collected upwind and downwind data using the mobile methane monitoring system, which included the LI-COR open path methane analyzer and 3-D anemometer. Figure 5.2 shows the layout for this audit noting that the generalized wind direction was opposite that from the previous audit. Also note that P represents the location of the utility pole that will likely serve as the location for long-term monitoring equipment. The upwind locations is labeled as A and three downwind locations are labeled as B1-B3.

Figure 5.2: General layout of indirect methane monitoring during Audit 6.

Figure 5.3 shows the methane enhancements above the minimum background of the site as collected at site A. Peak background enhancements at this upwind location were less than 160 ppb. Figures 5.4, 5.6, and 5.7 show the downwind enhancements from locations B1, B2, and B3,

respectively. Data collected at location B1 showed the highest methane enhancements (around 350 ppb) with a weak Gaussian distribution centered around 180 degrees. Data collected at location B2 showed no significant enhancements and data at B3 were similar to those data collected at location A (upwind).

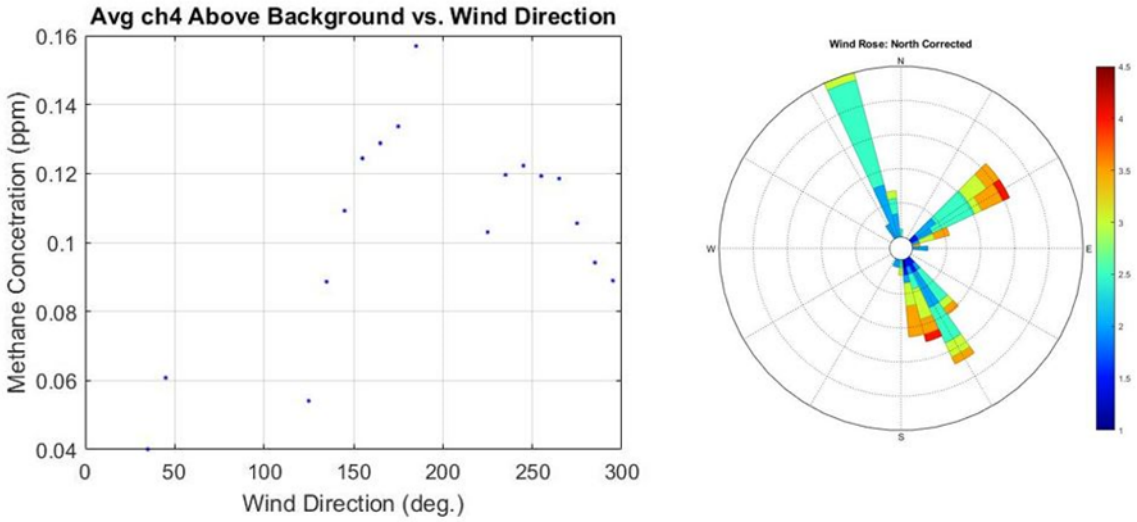

Figure 5.3: Upwind methane concentration enhancements (location A).

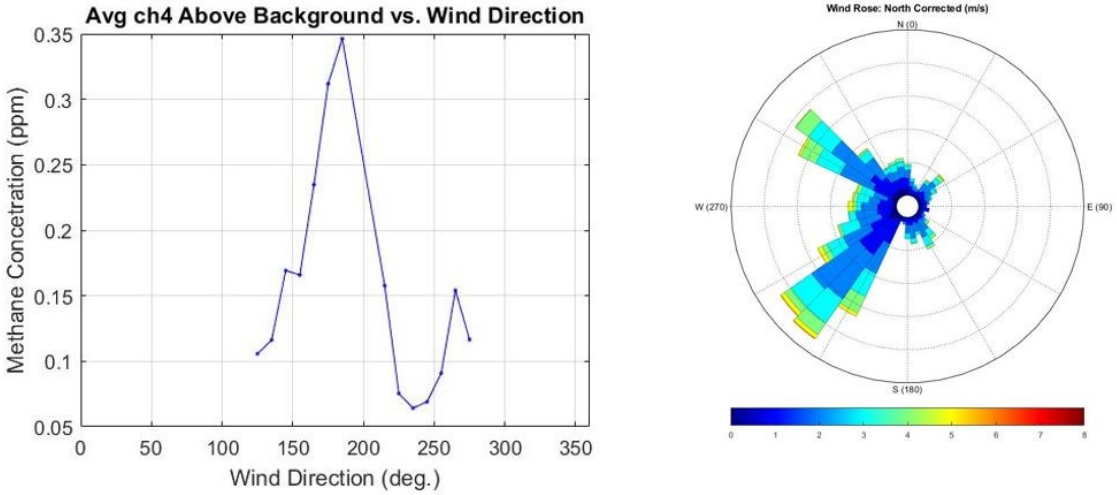

Figure 5.4: Peak downwind enhancement at location B1.

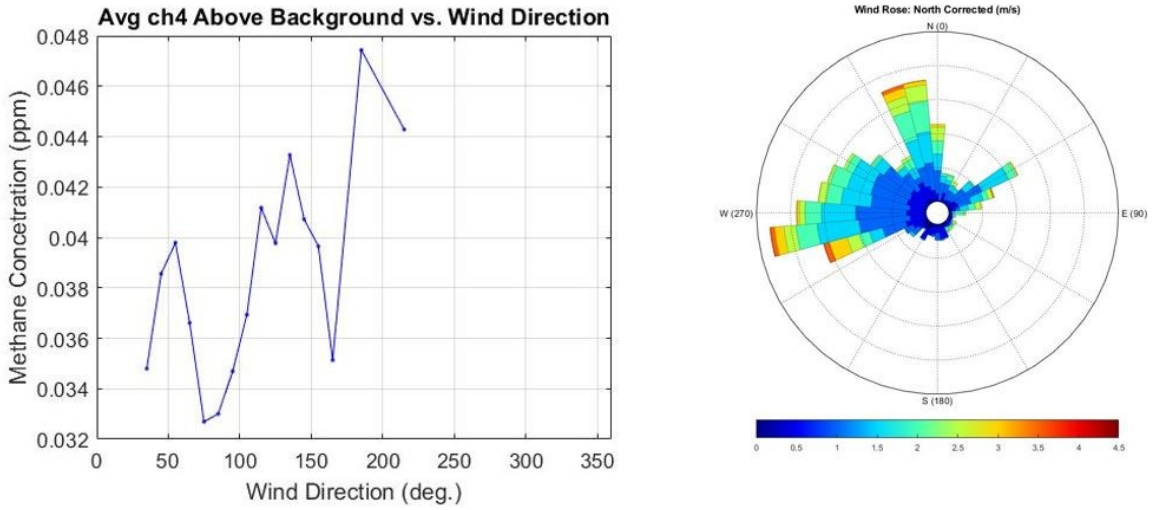

Figure 5.5: Methane enhancements at location B2.

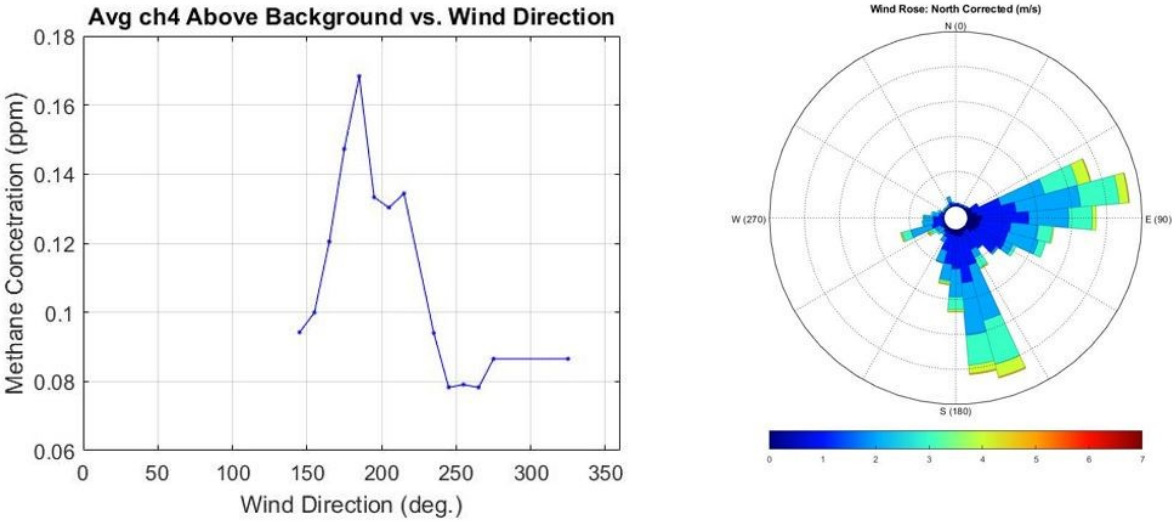

Figure 5.6: Methane enhancements at location B3.

Products

No new products at this time.

Plan for Next Quarter

- Finalize temporal emissions paper.
- Finalize design and procurement of the solar power system
- Develop remote data logging system.
- Install basic components on utility pole.
- Complete Audit 7 including upwind and downwind data.

Topic 6 – Water Treatment

Approach

This effort is focused on characterizing the chemical and biological factors that influence radium accumulation in sludge from produced water. This research could lead to the development of low cost treatments for produced water that prevent the accumulation or radioactive sludge. This work is in service of Milestone 33: Results of techniques for low cost treatment of flowback waters. To accomplish this milestone, the team is performing a series of laboratory microcosm experiments. Produced water is incubated for 21 days in the laboratory with or without additions of sulfate (200 or 2000mg/L) and nutrients (carbon, nitrogen and phosphorus). The addition of nutrients is intended to stimulate the activity of microorganisms to immobilize sulfate and prevent it from precipitating with radium. Tests thus far have utilized produced water from the 3H.

Results & Discussion

Over the last quarter, the team completed one additional laboratory microcosm experiment and completed water chemistry analysis from previous incubations. Preliminary results suggest that sulfate is below detection in the produced water from well 3H. Sulfate additions (2000 mg/L) dramatically increased the precipitation of Ra226 from well 3H (Figure 6.1), this result was seen in two separate water samples (3 and 4) collected in the spring and summer. Nutrients did not reduce the precipitation of Ra 226 by sulfate as the Sulfate(2000)_CNP was similar to the Sulfate(2000) treatment. This suggests that microorganisms cannot immobilize sulfate before it reacts with Ra 226.

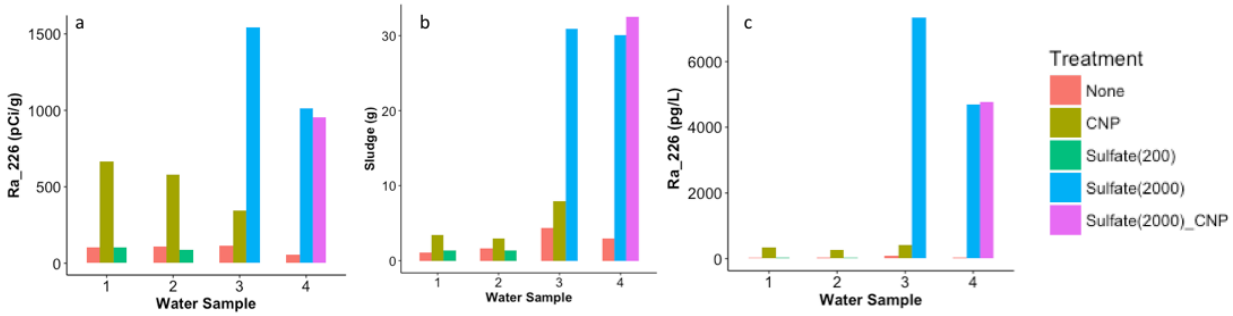

Figure 6.1: Radium 226 precipitation from produced water into solid sludge. Concentrations of Ra 226 (a), g of sludge produced from 6.5 L (b), and the total Ra 226 precipiated per liter of produced water (c). Data are shown for separate water samples collected from well 3H between December 2017 and May 2018.

Researchers also completed DNA extraction from each of the sludge samples, DNA has been successfully amplified in the laboratory and is ready for sequencing.

Products

Pending sample analysis, this work will be submitted for publication.

Plan for Next Quarter

The team will complete sample analysis for the microcosm experiment conducted in August. Further, within the next reporting period, the team plans to send DNA samples to an analytical facility for sequencing to characterize the microbial communities in the produced water samples and solids. Once data for the august incubation has been received, researchers will begin final statistical analyses to address milestones.

Topic 7 – Database Development

Approach

All MSEEL data is now online and available to researchers (Figure 7.1 and 7.2). The website has been updated with the latest production beyond the end of the quarter (Figure 7.3). Work continues

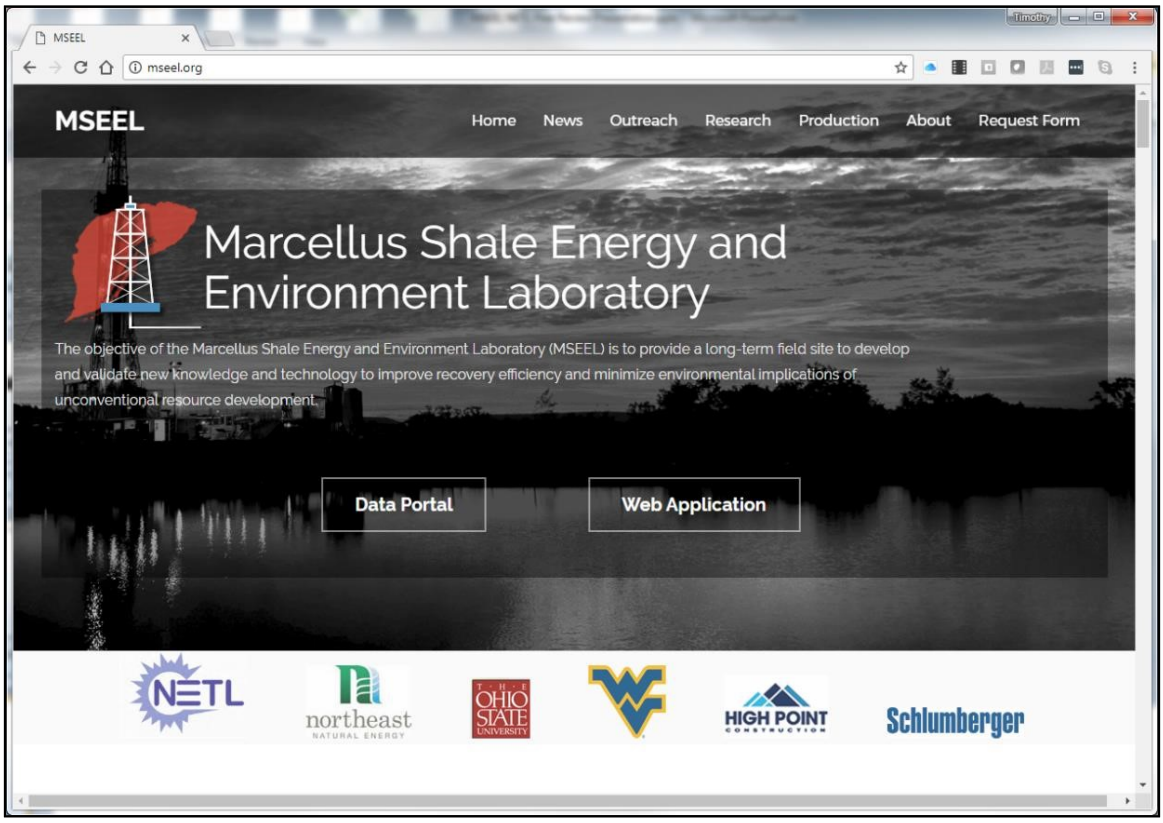

Figure 7.1: MSEEL website at http://mseel.org/.

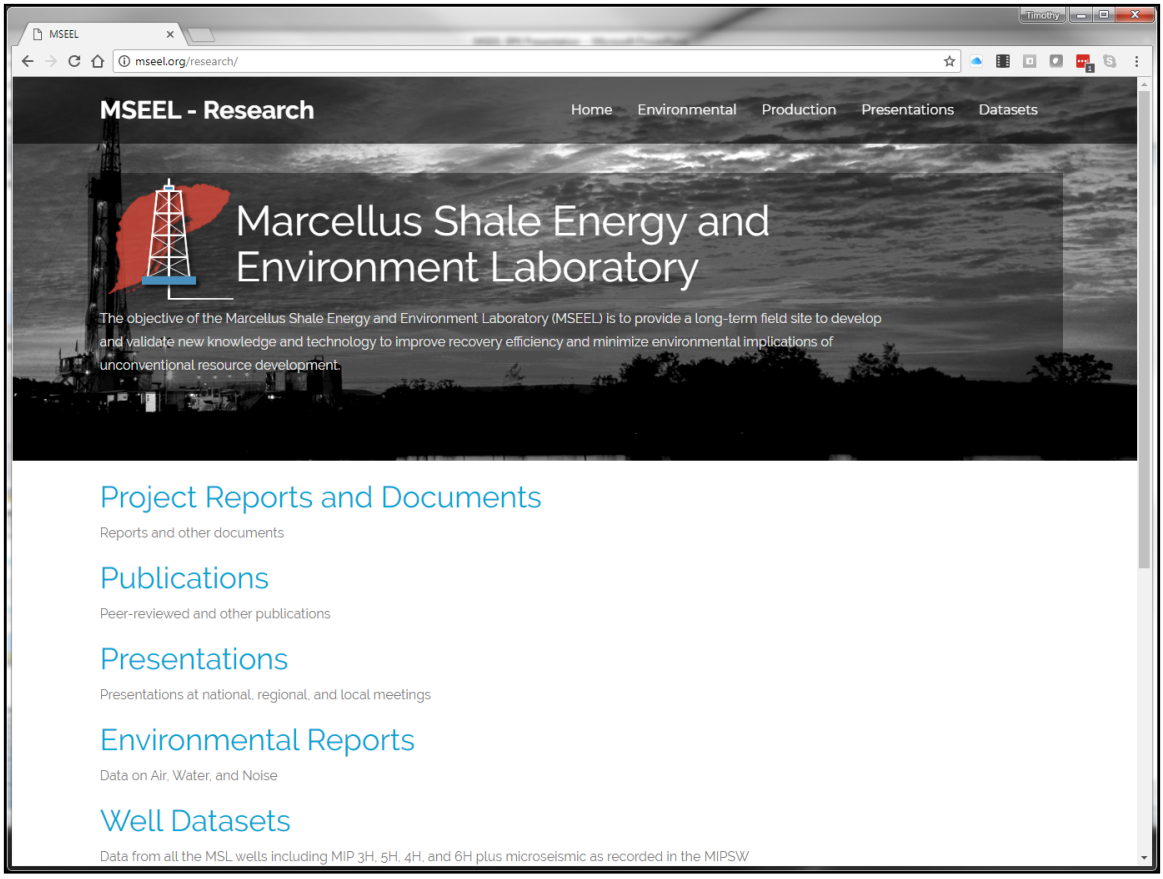

Figure 7.2: All data generated by the MSEEL project is available for download at http://mseel.org/.

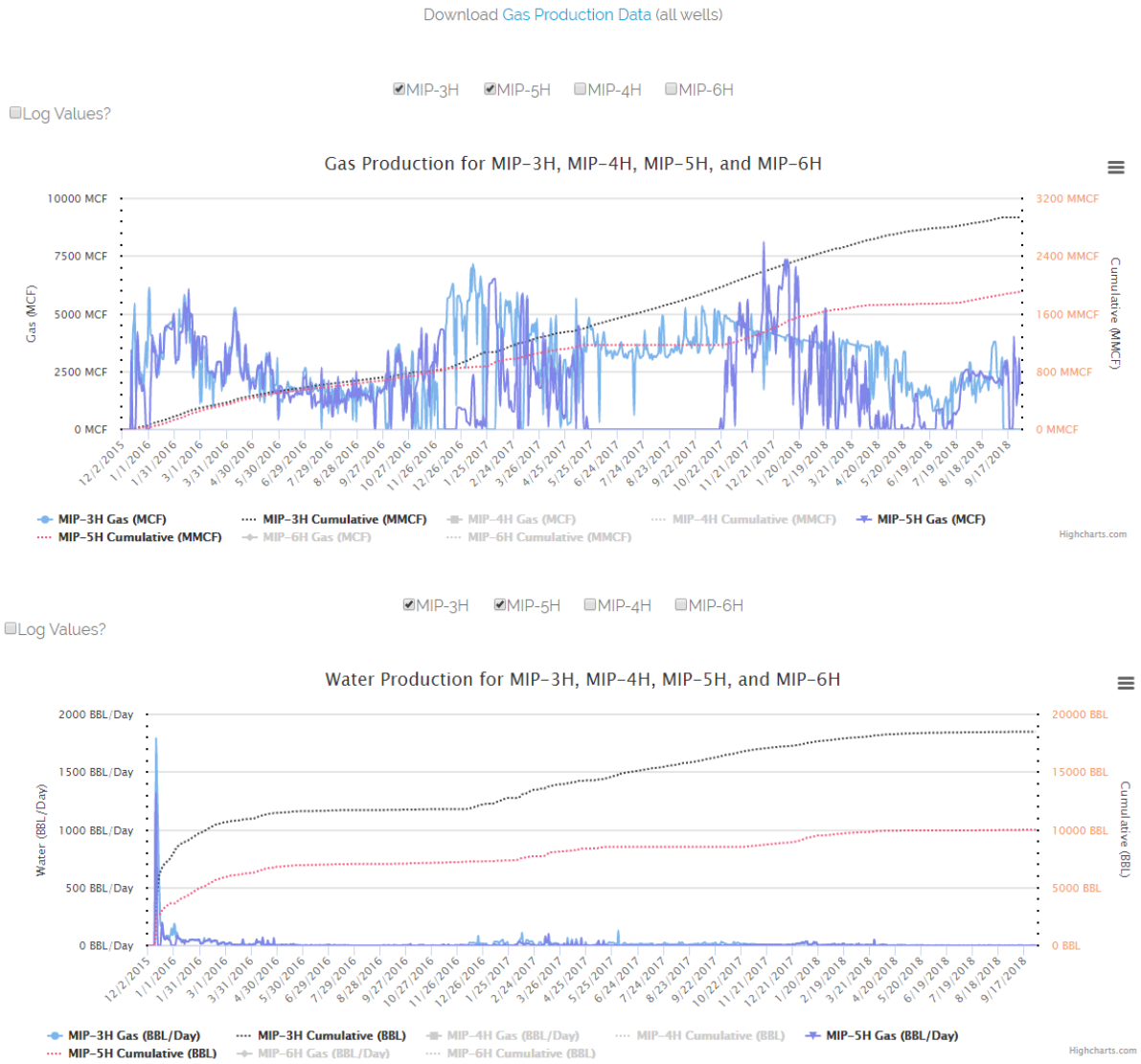

Figure 7.3: Gas and water production have been updated through the end of the quarter and are available at http://mseel.org/.

Results & Discussion

Data and publications are now available at http://mseel.org/.

Products

Web site enhanced and updated.

Plan for Next Quarter

Working to develop interactive programs to display user selected well logs and geochemical data. A mock-up of the type of display is shown in Figure 7.4.

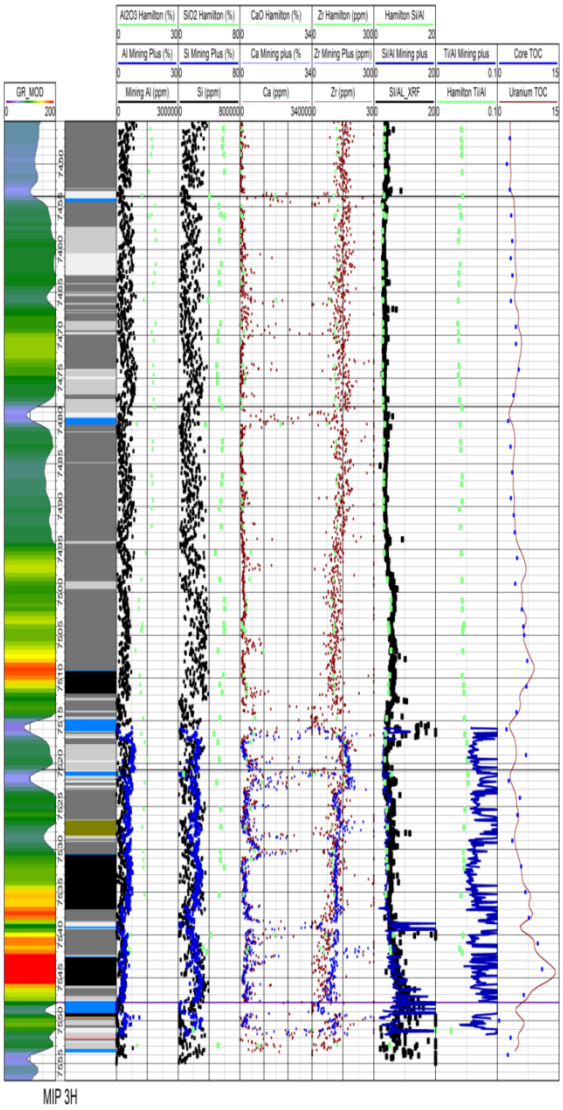

Figure 7.4: Display of log and geochemical data for the MIP 3H pilot hole on the MSEEL.ORG site. The user will be able to select the type of data and scale of displays.

Topic 8 – Economic and Societal

<u>This task is complete and will not be updated in future reports.</u>

Appendix 1

SPE-194814-18ERM-MS

A New Algorithm for Processing Distributed Temperature Sensing (DTS)

2018 SPE Eastern Regional Meeting

Timothy Carr and Payam Kavousi Ghahfarokhi, West Virginia University; BJ Carney and Jay Hewit, Northeast Natural Energy, LLC; and Robert Vagnetti, National Energy Technology Laboratory, US Department of Energy

Abstract

Distributed temperature sensing (DTS) was used to record temperature from early 2016 to present for a Marcellus Shale horizontal dry gas well, MIP-3H, located in Monongalia County, West Virginia. In addition, after wellbore clean-out with water and nitrogen a flow scanner production log was conveyed on March 02, 2017. The flow scanner provides one day of gas and water production from each of the 28 stages in MIP-3H and from each of the clusters. The DTS data provides an opportunity to inspect the reservoir for Joule-Thompson (JT) effect, a phenomenon that describes cooling of an non-ideal gas as it expands from high pressure to low pressure, and obtain a relative production attribute along the lateral of the MIP-3H. The original fiber-optic DTS data shows the temperature along the lateral; however, due to the geometry of the well with toe up and the presence of a small fault and minor water production at Stage 10 relative gas production of each stage cannot be directly determined from the raw DTS data. We present two methods to generate DTS attributes that can be used to better reveal relative gas and water production through time from each perforation cluster and each stage of the MIP-3H. The first attribute deals with the deviations of the DTS measurements from the calculated geothermal temperature, while the second attribute calculated the difference between DTS temperature and the average daily DTS temperature along the lateral of the MIP-3H. We show that the latter DTS attribute provides a more robust image of temperature variations regime along the lateral than the former attribute. Negative values of the DTS attributes reveals JT cooling, resulting from stages of the MIP-3H with higher natural gas production. A correlation analysis of the production log with the calculated DTS attributes suggests that the production log is not representative of the entire production life of MIP-3H well. Temporal correlation with the DTS attributes is highest close to the production

log recording day (March 2, 2017) decrease rapidly and the weak correlation switches from positive to negative.

Introduction

Background:

The multidisciplinary and multi-institutional team of the Marcellus Shale Energy and Environmental Laboratory (MSEEL) works on geoscience, engineering, and environmental research in collaboration with Northeast Natural Energy LLC, several industrial partners, and the National Energy Technology Laboratory of the US Department of Energy. The MIP-3H well is located in the core play area of the Marcellus Shale, in Monongalia County, West Virginia. The lateral of the MIP-3H landed and stayed in the target zone just above the Cherry Valley Limestone in the Marcellus Shale (Figure 11).

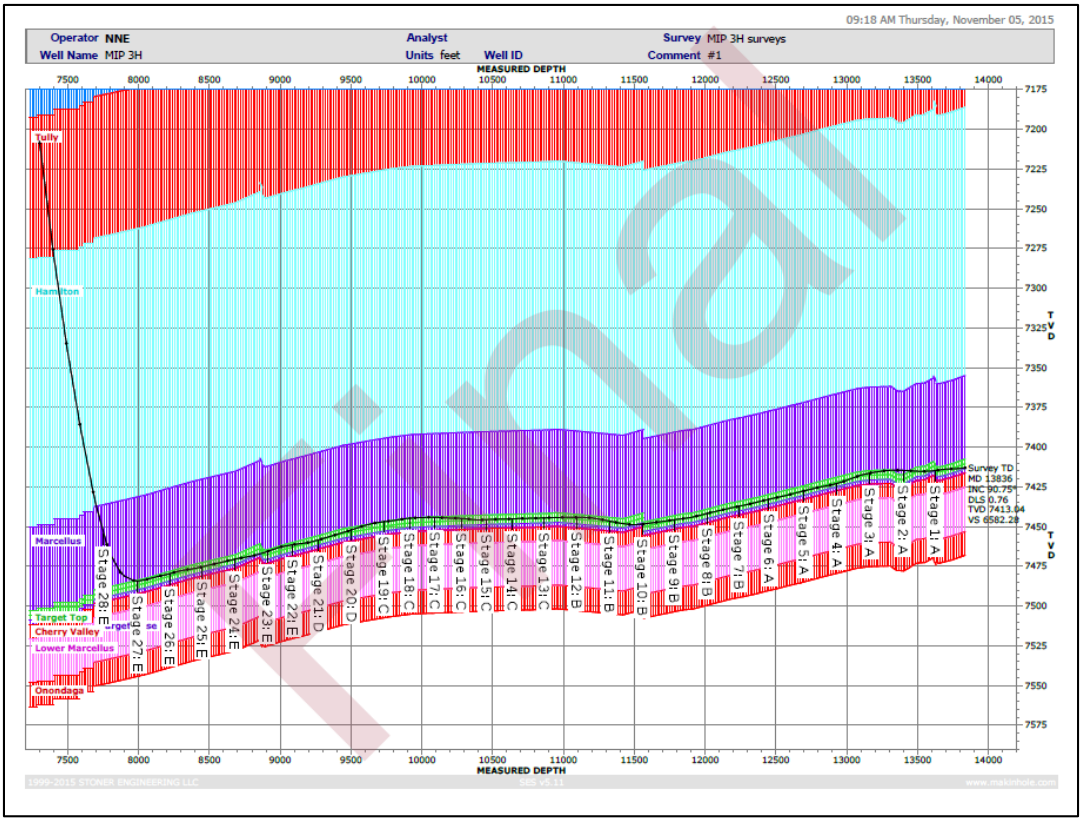

Figure 11: The MIP-3H well trajectory. Due to the geometry of the formation the toe of the well is approximately 60ft TVD (18m) structurally higher than the heel of the well.

The MIP-3H stimulation over 28 stages involved injection at high pressure, averaging 8500 psi (58.6 MPa), to fracture the formation and establish a complex network of propped permeable fracture pathways. A permanent fiber-optic cable was attached along the outer part of the casing to record acoustic vibrations during completion. Distributed acoustic sensing (DAS) provides a measure of relative strain and injection energy. Distributed temperature sensing (DTS) was also recorded during stimulation and at intervals of several times per day during the subsequent production period.

Each stage is approximately 200 feet (60m) long and has 4 to 5 perforation clusters, each consisting of 4-5 shots/foot. The spacing between stages varies between 20 to 50 feet (6-15m) with

an average of 24 feet (7m) between plug depths to the nearest cluster in the previous stage. Clusters within each stage are spaced at 30-50 feet (9-15m) intervals. The MIP-3H well is a dry gas well, and after initial production and outside of the clean-up associated with the production logging, produces less than 10 barrels of water per day. Daily gas and produced water production is updated monthly and is available on the MSEEL website (http://www.mseel.org).

Analysis of microseismic, core and log data coupled with with DAS and DTS fiber-optic monitoring during completion in the Marcellus Shale shows the influence and interaction of both the present stress regime and the preexisting healed and calcite cemented small faults and numerous clusters of fractures oriented approximately east-west (Carr et al. 2017; Kavousi et al. 2017). Many of these preexisting factures led to uneven stimulation between clusters, and where faults and fractures are relatively more concentrated, allowed DAS attributes to detect communication of stimulation fluids between stages (Kavousi et al. 2018).

This study deals with the DTS data recorded during a production interval from May 5, 2016 to May 1, 2018. The two years of DTS data along with a flow scanner log on March 2, 2017 provides the opportunity to monitor production behavior with time.

DTS Basics:

DTS technology utilizes a fiber-optic cable to measure temperature around the cable. A fiber-optic cable is composed of a core, which is the light carrying element, and cladding, which provides the lower refractive index for total internal light reflection throughout the cable (Nath et al., 2005, 2006). A fiber-optic system sends laser pulses at 10-ns or less down the length of the optical fiber. Incident lights collide with the molecular and lattice structure of the fiber medium and photons get scattered from the fiber-medium. The majority of photons that collide with the atoms in the fiber-medium are elastically scattered and have the same frequency and wavelength as the incident light. This energy preserved scattering, which is the strongest signal, is called a Rayleigh scattering. Brillouin scattering is an inelastic scattering that takes place when acoustic waves vibrate the fiber lattice at the molecular level and change the local refractive index of the optical fiber. In addition, a part of incident photons are scattered through the inelastic Raman Effect, in which the energy of the scattered photon might be higher or lower that the incident photon (Brown, 2006). The scattered photon could gain energy from displacing the fiber molecules to a lower vibrational energy state (anti-Stokes scattering), or lose energy to the fiber-medium molecules and raise them to a higher vibrational energy state (Stokes scattering). The energy of a photon is inversely proportional to its wavelength: higher energy anti-Stokes scattered photons have shorter wavelength than lower energy Stokes scattering. The intensity of the anti-Stokes scattering is strongly dependent on the temperature, while the longer wavelength Stokes signal is less temperature dependent. The ratio of these intensities is directly proportional to the temperature of the optical fiber at the point where backscattering takes place. In a DTS system, backscattered lights are filtered to remove the Rayleigh and Brillouin backscatters, to evaluate the intensity ratio of Stoke and anti-Stoke Raman waves. The velocity of light in the optical fiber is usually less than the speed of light and can be calculated as:

$$v = \frac{c}{n} \qquad Eq.1$$

Where c is the speed of the light and n is the fiber refractive index, which is usually between 1.5 and 1.7 (Smolen and van der Spek, 2003). Thus, a 10-ns long laser will correspond to approximately a 2 meter segment of the fiber, with a refractive index of 1.5. This will turn the optical fiber into a multi-point temperature sensor in the subsurface. This superiority over single point temperature measurement gauges has made the DTS a widely used and efficient temperature measurement tool.

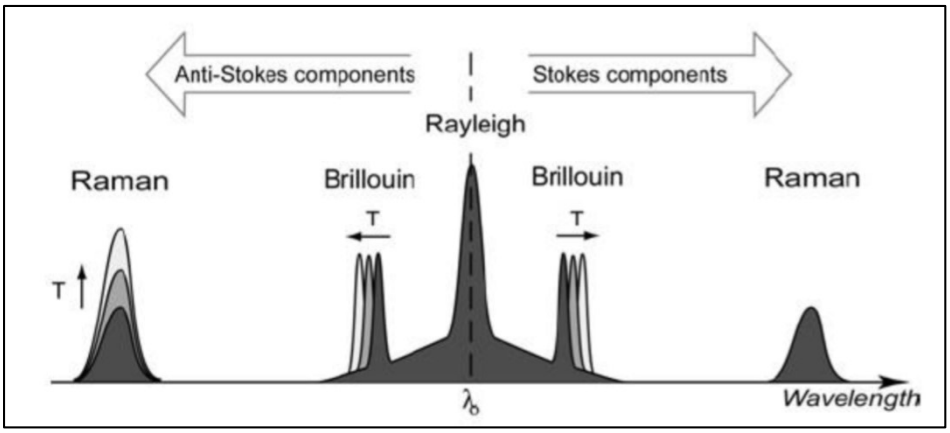

Figure 12: The incident laser is backscattered in different wavelength Raman and Brillouin waves; however, a majority of the incident laser is backscattered with the same wavelength as the incident laser through Rayleigh scattering. An increase in temperature (T) results in movement of the Brillouin waves and an increase in the Anti-Stokes components of Raman waves (Courtesy of Mishra et al., 2017).

Application of DTS:

Various industries using temperature change in DTS systems as an indication of abnormal behavior or an imminent failure of a system such as a pipeline, pressure vessel, fire detection in tunnels, etc. (Peck and Seebacher , 2000; Barber et al., 1999; Walker and Carr, 2003; Mishra et al., 2017). The oil and gas industry has used DTS technology in various places around the globe for different field development applications. Companies have used DTS to monitor steam flood enhanced oil recovery operations in a downhole environment where temperature exceeds 400 degrees Fahrenheit (Karaman et al., 1996; Gonzales et al., 2018; Carnahan et al., 1999). DTS has also been used to infer production profiles from horizontal and vertical wells (Lanier and Adams, 2003; Tolan et al., 2001; Wang 2012; Nath et al., 2007; Saputelli et al., 1999; Ouyang and Belanger, 2006; Kabir et al., 2008; Johnson et al., 2006). DTS can provide valuable information about the geothermal gradient if used as a well log. Liquid or gas production can affect the DTS readings and provide information about the point of entries for hydrocarbons. Gas production in horizontal wells is associated with a drop in pressure and change in volume, which is therefore accompanied by a change in temperature. The Joule-Thompson effect describes the temperature change for a real gas or liquid when it is forced through a porous plug (throttling) in an adiabatic process (Roy 2002). This temperature variation is governed by the Joule-Thompson coefficient (JTC or μ_{JT}) as:

$$\mu_{JT} = (\frac{\partial T}{\partial P})_h \qquad Eq.2$$

where T is Temperature, P is pressure and h is specific enthalpy (Cengel and Boles, 2008). The equation shows the rate of change of temperature versus pressure, at constant enthalpy. During a sudden pressure drop, the sign of the μ_{JT} describes the temperature change as:

$\mu_{JT} < 0$, temperature increase

$\mu_{JT} = 0$, temperature remains constant

$\mu_{JT} > 0$, temperature decreases.

Pinto et al. (2012) undertook a linear mixing approach to predict μ_{JT} for a natural gas, which has methane as the major component, at various pressures and temperatures. Natural gas showed a positive μ_{JT} for pressure ranges from 72.5psi to 3625.9psi at temperatures of -9.4°F, 35.6°F, 80.6°F, and 170.6°F. The temperature usually decreases when gas enters the wellbore and increases when oil or water enters the wellbore (Brown et al., 2006). Brown et al., (2006) carried out DTS data analysis for a horizontal well in offshore peninsular Malaysia, in the South China Sea, to diagnose the oil production drop. They showed that a gas cap expansion, detected by a temperature drop through DTS, limited liquid 0production from the reservoir. Wang et al., (2008) proposed a flow-profiling model using DTS data for oil and gas wells. They showed, through analytical and numerical modeling, that the Joule-Thompson (JT) effect usually happens in gas wells except in very high bottom hole pressures around 8000psi where a warming effect might occur. Tight gas reservoirs, such as Marcellus Shale, have considerable pressure draw-downs close to the horizontal wellbore and so the JT effect should be observed. The cooling effect for gas can vary between 2 to >20 °F per 1000psi pressure drawdown; in contrast, water produces a warming effect of around 3°F/1000psi (Johnson et al., 2006).

DTS can also reveal cross-stage flow communication in unconventional oil and gas reservoirs during hydraulic fracturing (Ghahfarokhi et al., 2018; Amini et al., 2017). Leakage through plugs during hydraulic fracturing was also observed as abnormal DTS measurements during stimulation of a horizontal well in the Eagle Ford Shale (Wheaton et al., 2016).

We evaluated two years of DTS data during production from the MIP-3H well in the Marcellus Shale to reveal temperature variations during time that could be related to Joule-Thompson effect.

Discussion and Results

The DTS data from May 2016 to May 2018 along the horizontal section of the MIP-3H was compiled in a matrix with 950,000 measurements and was visualized in a waterfall plot (Figure 13). The DTS temperature shows that the toe of the well is relatively cooler than the heel of the well. Moreover, local cooler perforations can be observed from 9,500 to 10,500ft. However, the raw DTS data appears to be dominated by high temperature bands that are persistent along the well, especially during days with high production. Note that the MIP 3H supplies the City of

Morgantown and along with the other three MIP wells is directly tied to seasonal and even daily variations in consumption due changes in demand due primarily to weather.

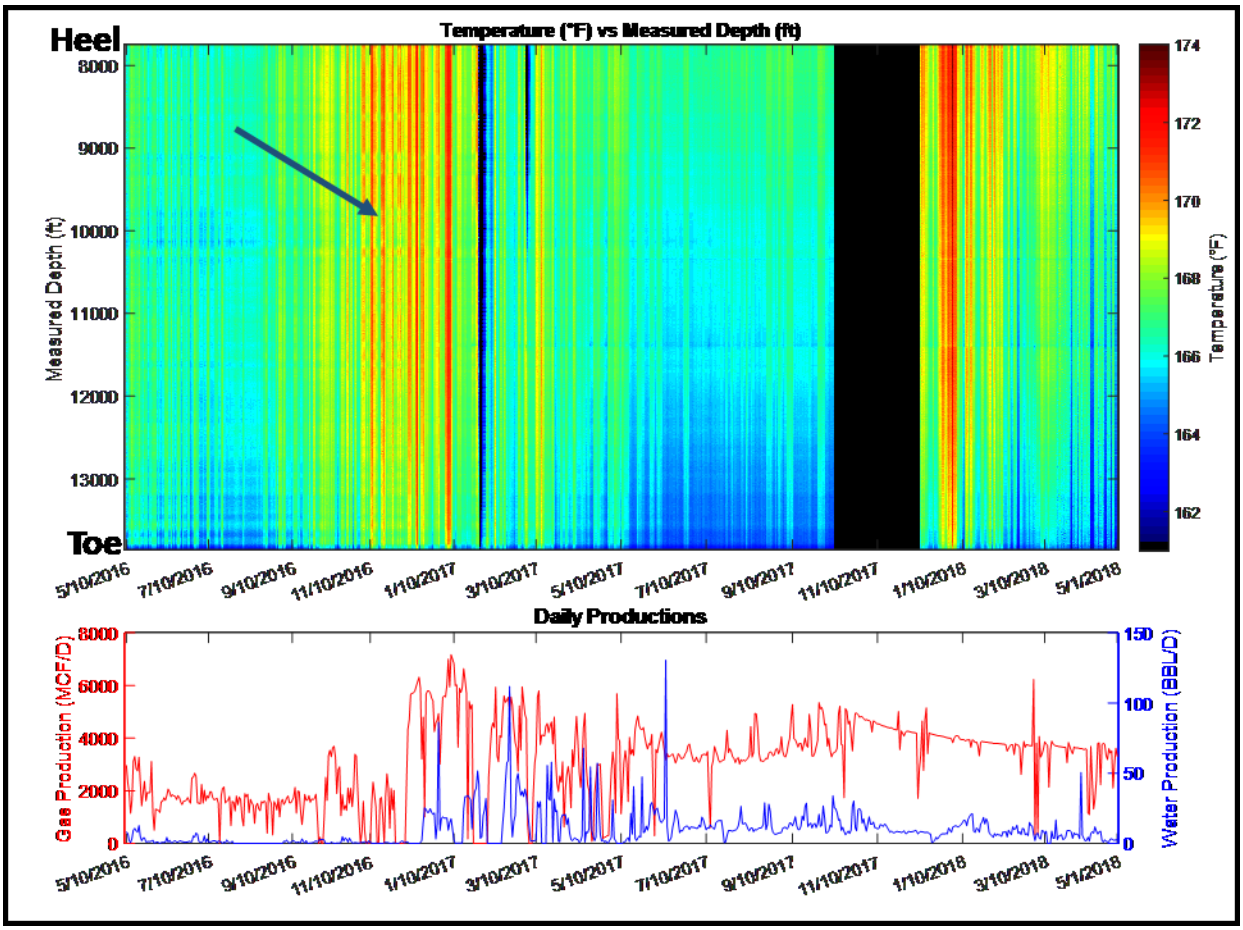

Figure 13: Upper plot shows the measured DTS from May 2016 to May 2018 from the heel (lower measured depth) to the toe (greater measured depth) of the lateral MIP-3H displayed as a waterfall plot. Gas and water production is shown in the lower graph. The large black section corresponds to missing data as a result of equipment issues. The arrow shows one of the high temperature bands during a period of high gas production.

The average daily temperature from the DTS data along the lateral follows the gas production trend from the well (Figure 4). The MIP-3H well is nearly horizontal, the elevation difference between toe and heel is approximately 60 feet (18m) TVD. This elevation difference is considered in this study to ensure an accurate estimation of geothermal temperature.

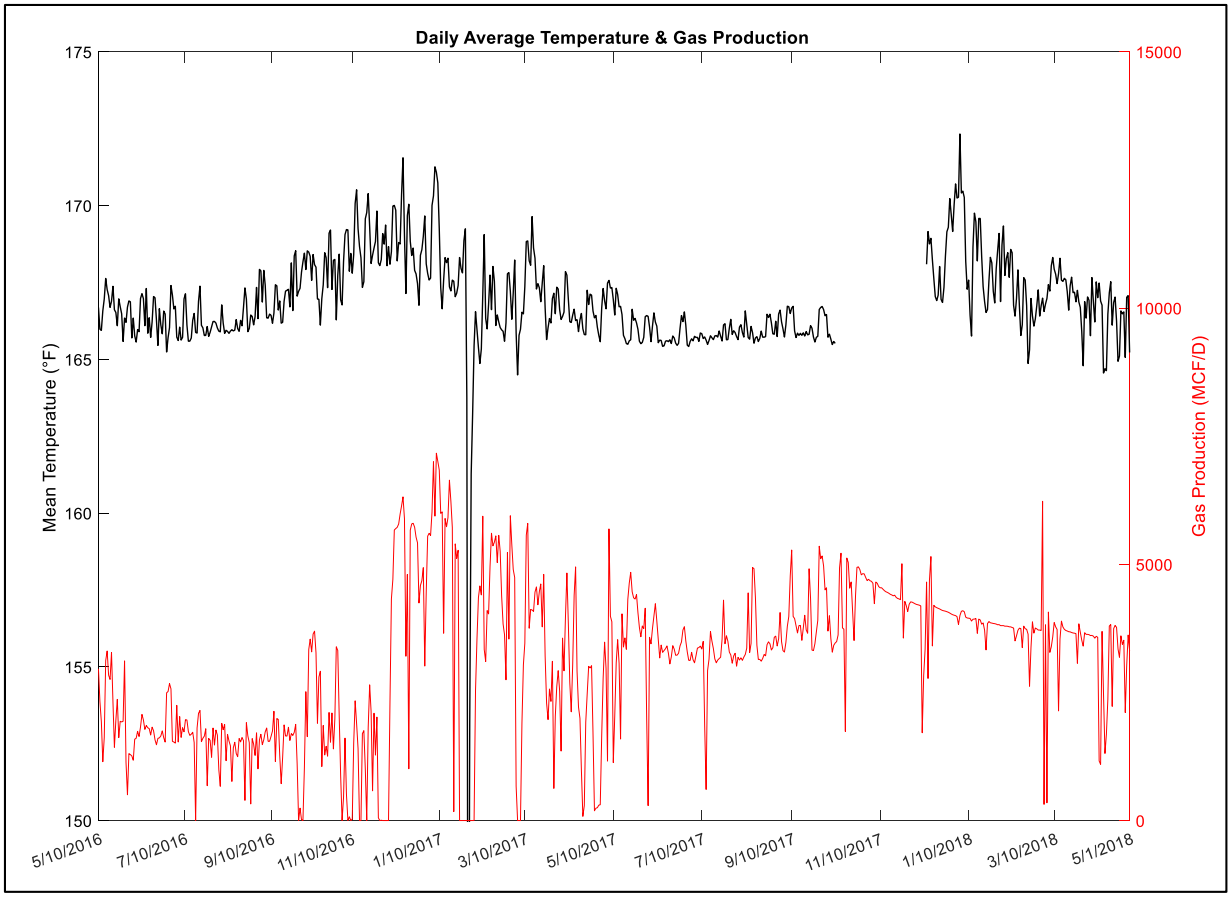

Figure 14: Average daily DTS temperature along the well is shown with gas production for the entire dataset. Note that DTS was not available for several months in late 2017.

We undertook two approaches to evaluate the Joule-Thompson (JT) effect for the MIP-3H. First, a conventional approach of temperature deviation from the geothermal temperature was assessed for JT effect. A 158°F bottom hole temperature (BHT) from well logging and an annual mean surface temperature of 52°F yielded a geothermal gradient of 1.35°F/100ft. BHT values are usually underestimated because of cooling effect of circulating mud in wells prior to logging. Deighton et al., (2014) suggested that BHT might be underestimated by 5-10°C (up to 30°C in some basins) due to varying heat conductivity of overlying formations. Frone et al., (2015) assessed the geothermal gradient for the Appalachian basin in West Virginia. They noted that BHT data from deeper than 1,000 meters is usually underestimated because of drilling fluid circulation. An equation was suggested to correct the BHT measurements between 1 Km (3280.84ft) and 3.9 Km (12795.27ft) as:

$$\Delta T = -16.51 + 0.018z - 2.34 \times 10^{-6} z^2 \qquad Eq.3$$

where z is the depth in meters, and T is the temperature in Celsius (Frone et al., 2015). The vertical pilot well for the MIP-3H recorded a BHT of 158°F at a depth of 7,834 feet, during well logging operations. Applying **Error! Reference source not found.** results in a BHT of 172°F that c orresponds to a geothermal gradient of 1.53°F/100ft, which falls within the expected range of 25° to 30° C/km (1.36° to 1.64°F/100ft; Fridleifsson et al., 2008). This gradient was utilized to evaluate the JT cooling effect for the MIP-3H. Because the MIP-3H trajectory is almost horizontal, Figure

5 has a very similar trend to the measured temperatures in Figure 3. However, the well has more cooling toward the toe and more warming toward the heel. Geothermal temperature can be predicted using the geothermal gradient and the trajectory of the well. Then, we subtracted the predicted geothermal temperature from the DTS measured temperature profile in Figure 3. A negative deviation from the geothermal temperature might suggest gas production (Figure 5). However, this temperature deviation attribute has uncertainties associated with variations in production of water along the lateral, the geothermal gradient, annual mean surface temperature, BHT measurement, and the assumption that layers above the Marcellus Shale are horizontal. A thermal-coupled fluid flow simulation such as Wang (2012) might shed light on reservoir properties. However, such a model will be a stochastic model due to uncertainties associated with geothermal gradient and reservoir properties.

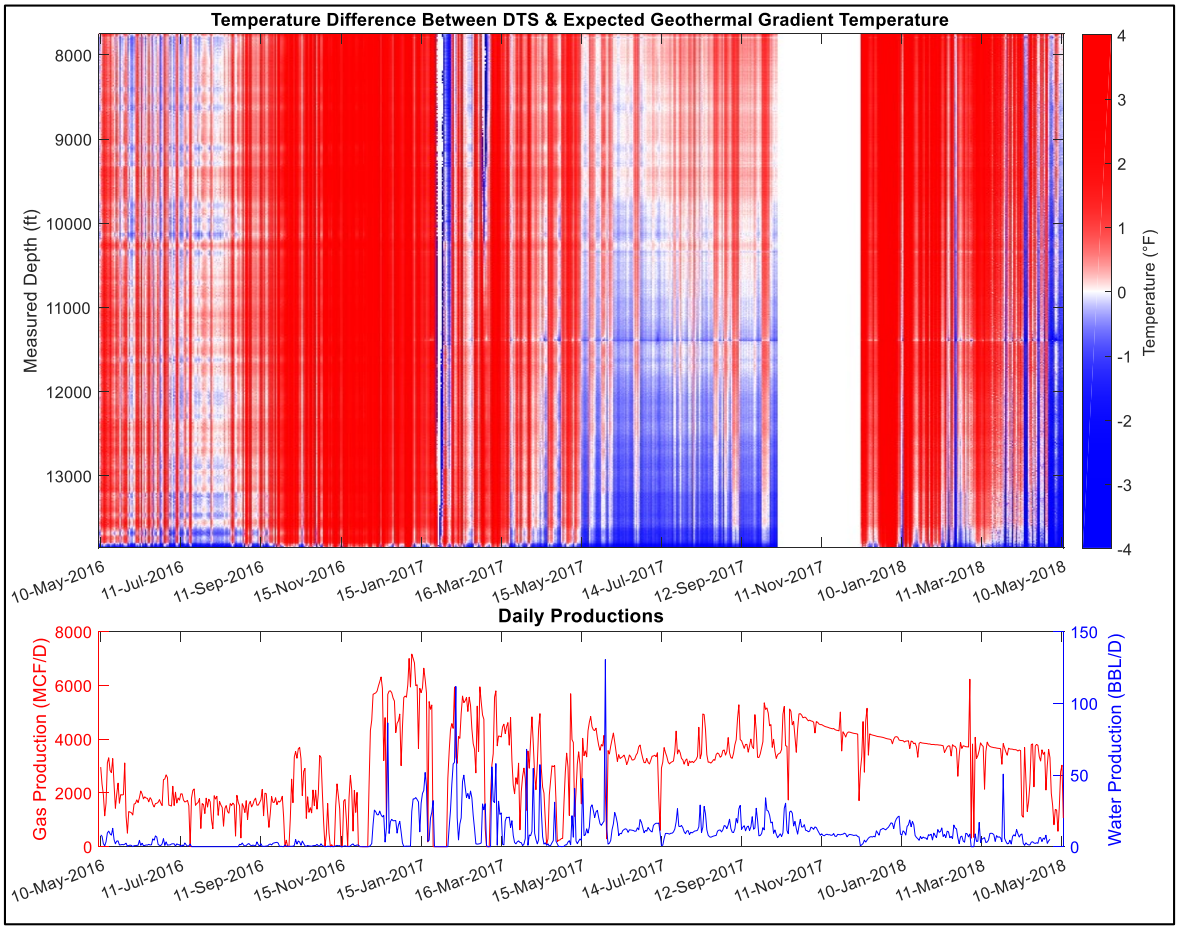

Figure 15: The difference each day between DTS measurements and calculated geothermal temperature is shown along the lateral of the well from the heel to the toe. Although dominated by vertical positive deviations due to changes in production, note the horizontal streaks that define individual perforations.

In another approach, we removed the trend of the DTS data introduced by the daily gas production. The average daily DTS temperature along the lateral is not a constant number and varies directly with the production rate from the well (Figure 4). Thus, DTS temperature deviations from the daily average temperature of the lateral were calculated. The de-trended DTS data also shows that cooling is more prevalent closer to the toe than the heel (Figure 6). In comparison to Figure 5,

which shows temperature deviations from the expected geothermal temperature, the second approach provides a smoother image of the subsurface temperature variation. Moreover, it is independent from the variations in seasonal and daily gas production, geothermal gradient, surface temperature, and overlying stratigraphy.

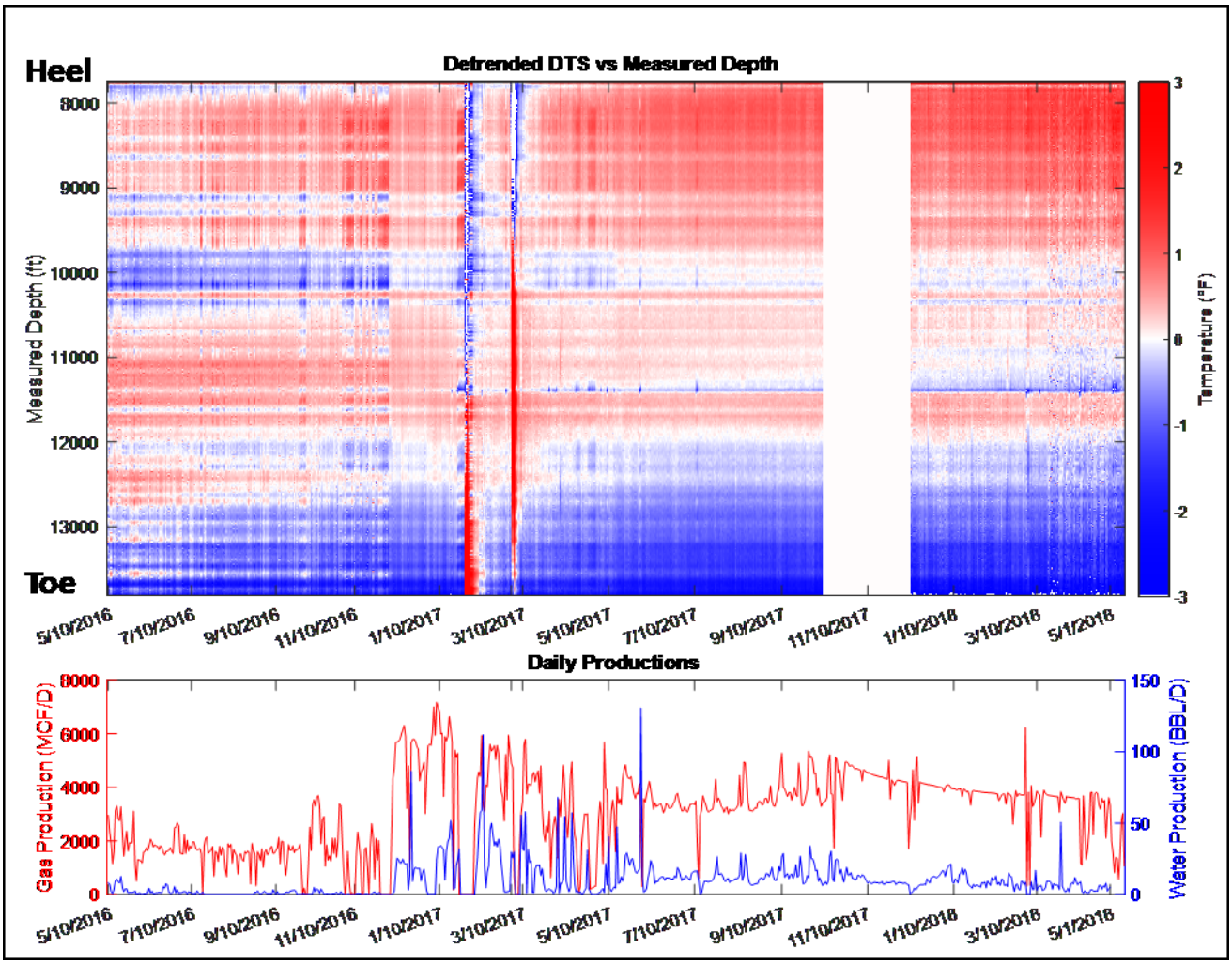

Figure 16: The de-trended DTS measurements show cooling close to the toe than the heel. Note that perforations are better defined in the de-trended DTS than DTS deviation attribute in Figure 5.

The de-trended DTS attribute can be upscaled to the stages scale (28 stages) to illustrate temperature variations for each stage relative to daily average temperature of each stage along the well (Figure 7).

On the production de-trended DTS attribute, general cooling from the heel to the toe is still observable, but some stages such as 10 and 11 and 20-21 and 23-28 are relatively warmer. Also standing out are the cooler stages 17-19. By integration of image logs, DAS and DTS data, and DAS attributes, a fracture swarm and small fault were observed in Stage 10 that resulted in a non-optimum stimulation and communication with the previous stages (Carr et al. 2007; Amini et al. 2007 and Ghahfarokhi et al. 2018). MIP-3H also has a production log (PLT) that was recorded on March 2, 2017. The production log from the MIP 3H shows the interpreted entry of produced water at stage 10 and flow downward toward the heel (Figure 8). While temperature usually decreases

when gas enters the wellbore and the entry of fluid in this case the entry of water will result in an increase in temperature (Brown et al., 2006). This increase in relative temperature has persisted through the entire production interval sampled. Many of the stages that were engineered with selective positioning of clusters (stages 13-19) show relative cooling. While stages 23-28 near the heel show increases in the relative temperature attribute. These stages at the lowest part of the well may be affected by pooling of relative warmer water, and the toe stages producing more gas relative to the heel stages (figures 7 and 8).

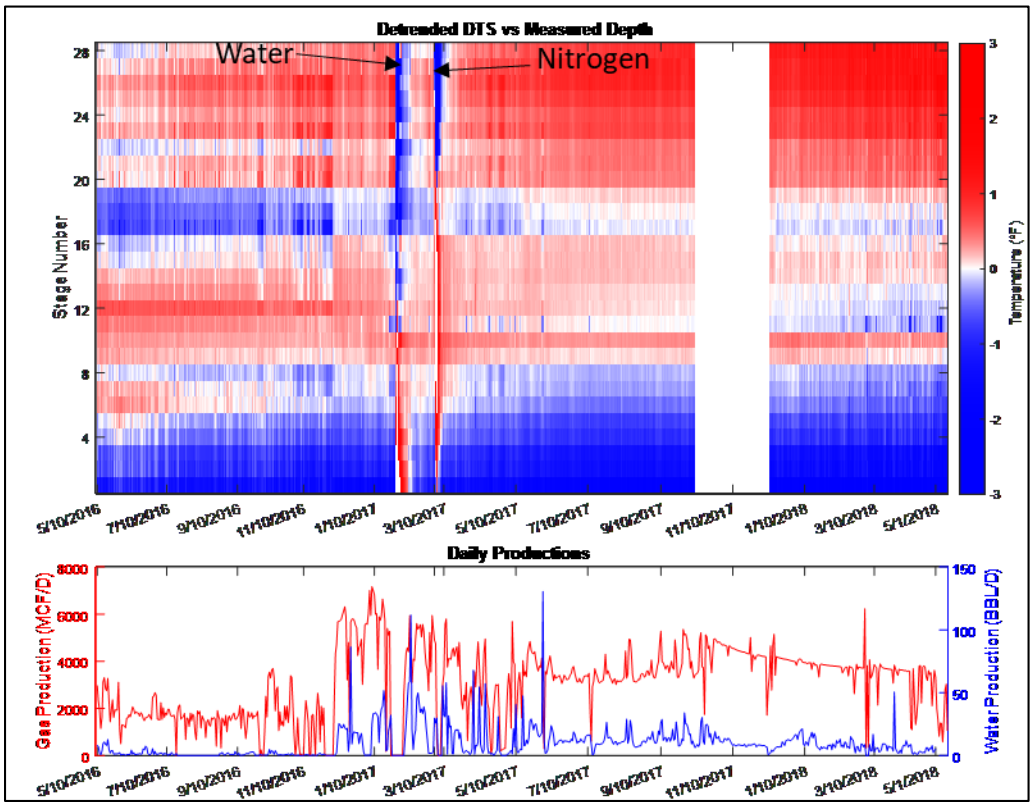

Figure 7: The de-trended DTS attribute is averaged to the stage scale. The arrows show the time that MIP-3H was washed with water and then with nitrogen foam prior to production logging.

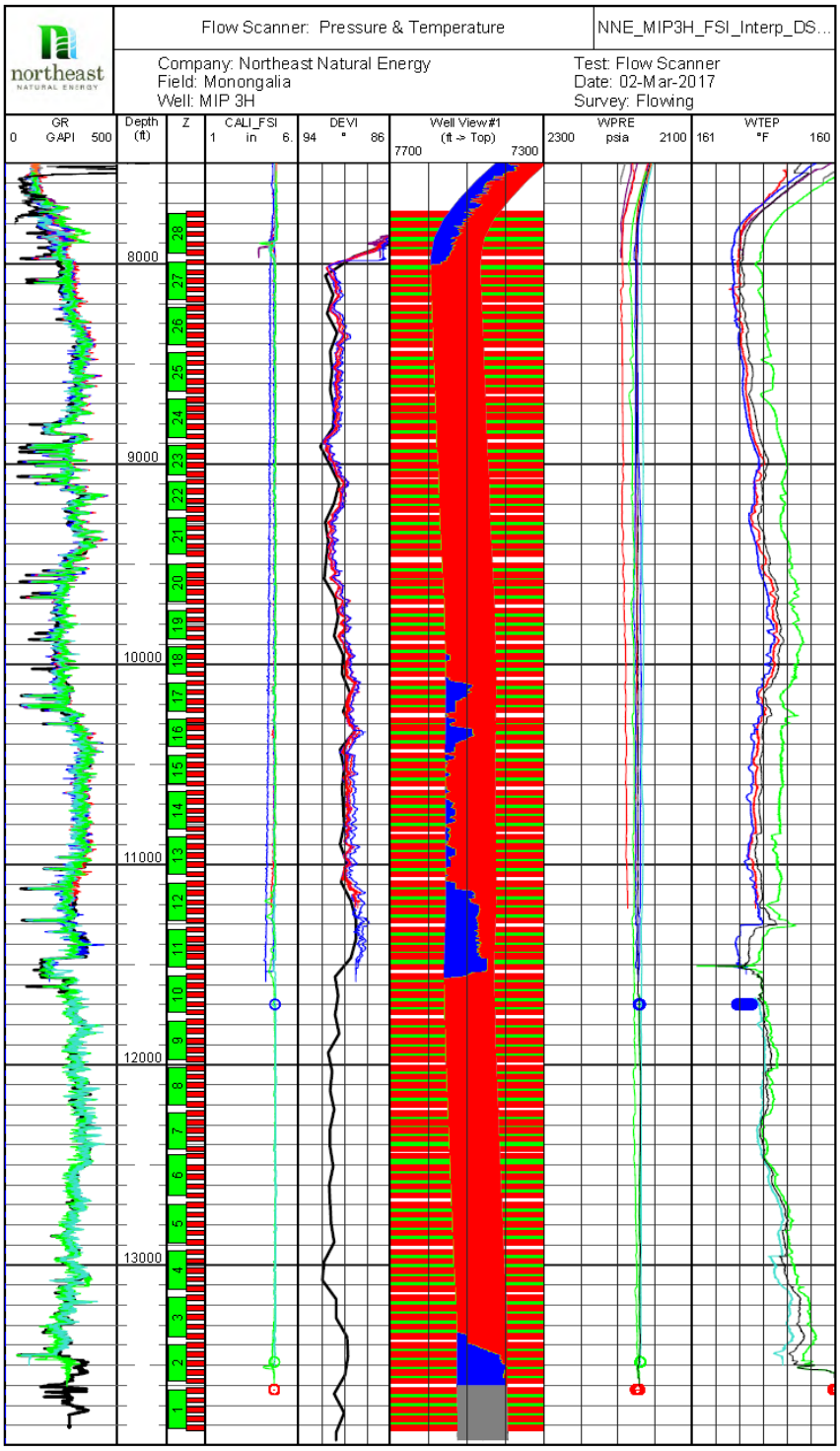

Figure 8: Production log for the MIP 3H showing 4 individual attempts, only one of which reached to near the toe of the lateral. Deepest log data was recorded at 13,530 ft. MD. The deviation track (Track 5) shows that on average the MIP 3H heel is deeper than the toe, but that relatively low spots exist from stages 4 to 10 and 23 to 27. The Wellview track (Track 6) shows the measured gas holdup (red) and water holdup (blue) directly related to trajectory; water (heavy phase) collects in low spots (deviation < 90 degrees) and immediately after Stage 10 while gas (light

phase) collects on the high-side. The entry of water at Stage 10 results in a change in the temperature curves (Track 8). It is believed that water entry at stage 10 is related to fracture swarms and a small fault and flows toward the heel.

The de-trended DTS data shows that clusters underwent changes after washing the well with water and later by nitrogen foam. The gas production rate is significantly increased in late 2016 (almost 3 times that of previous trend). As reservoir pressure depletes, gas volume expands in the reservoir. Consequently, a higher gas rate within the fractures is expected, which increases the drag force around the proppants. That might mobilize proppants and pinch out some portion of the fractures. This could damage near wellbore conductivity and hence lowers the gas production later during the life of the reservoir. The washing procedures affected the temperature variations just for a limited time. The major factor appears to be the gas rate from the reservoir that resulted in lower gas productivity in some perforations. Recent DTS data from 2018 suggests that an unconstrained stabilized production is causing a general cooling effect for the entire well but is more pronounced close to the toe, water is being produced at Stage 10, and that water is increasing to collect in the relative low area near the heel.

Stage 10 in Figure consistently shows warming during the length of this study. This stage was previously studied by several researchers and has been shown to have several pre-existing faults and around 160 identified fractures. Ghahfarokhi et al., (2018) showed evidence of these faults and fractures reactivations from microseismic and distributed acoustic sensing (DAS) data. We suggest that high concentration of faults and fractures contributed to an ineffective hydraulic stimulation, and subsequent higher water production.

We calculated the correlation coefficients between each perforation's production from the PLT and the two temperature deviation attributes proposed in this study (Figure 9). The de-trended DTS shows a higher correlation with the PLT especially on the day of production logging. The correlation coefficients decrease rapidly away from this event and turns from positive to negative correlations. This could be due to our observations that stages close to the toe are getting colder and stages close to the heel are getting warmer. Production logging was carried out after washing with water and nitrogen, as shown in Figure 7. Washing the well significantly changed the downhole temperature and created temporal temperature anomaly in days close to the production logging. The poor correlation between the PLT log and the rest of the DTS data could cast doubt on the one day PLT results directly representing the earlier and later life of the reservoir. However, the PLT log provides critical insight into using the DTS to interpret gas and water production along the lateral and among stages.

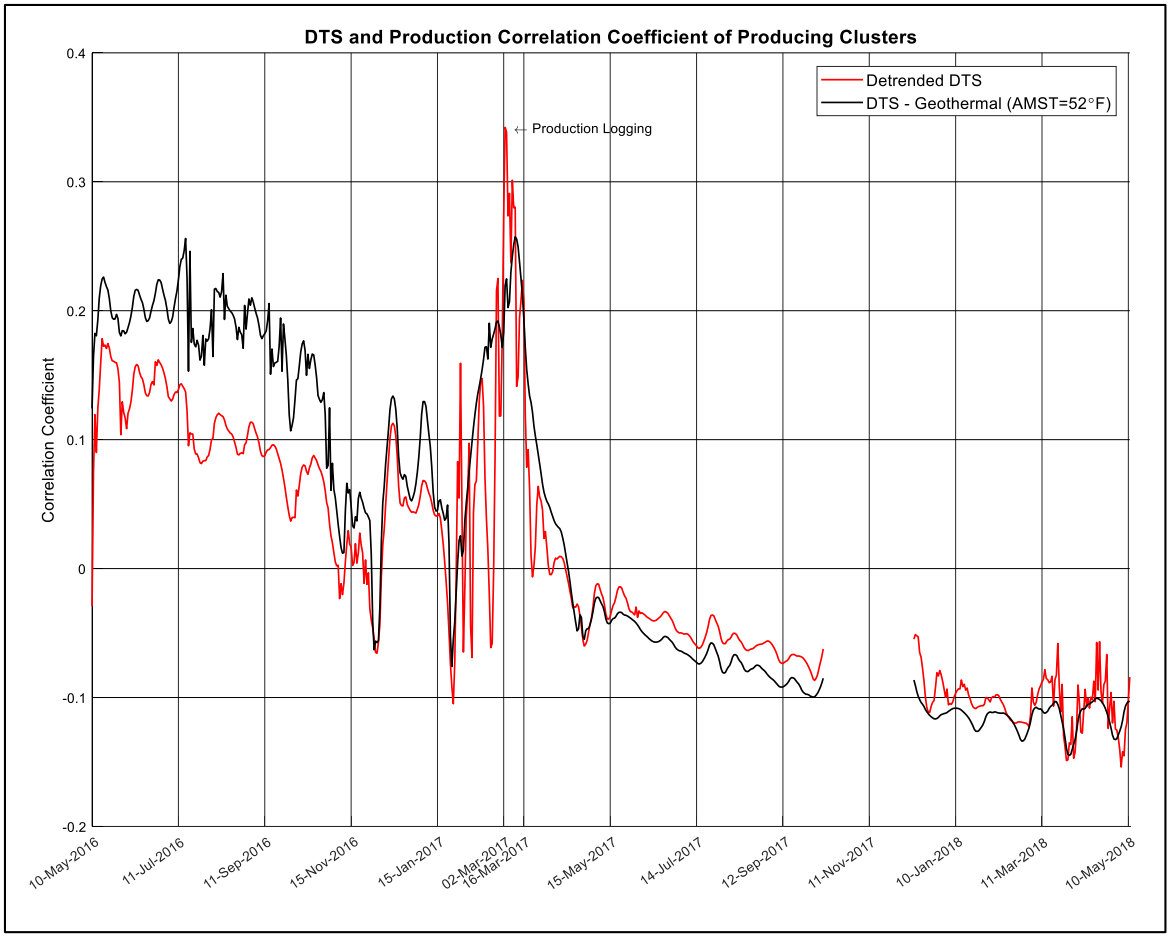

Figure 9: The correlation coefficients between two DTS attributes and the production log are presented. The de-trended DTS shows relative higher correlation with the production log than the DTS geothermal deviation attribute at and after the production logging event. All correlation coefficients are relatively small. Note the reversal in correlation coefficient sign from positive to the negative before and after the production logging event.

Conclusions

Two DTS temperature attributes are presented in this paper. Both attributes suggest that cooling is more dominant closer to the toe of the MIP-3H but varies by stage and through the production history. The decrease of DTS temperature attribute across the toe and engineered stages (stages 13-19) s are suggestive of the Joule-Thompson cooling effect as a result of relatively higher gas production. The increased DTS temperature attribute at Stage 10 and near the heel is suggestive of water production and may affect gas production. We show that the DTS geothermal deviation attribute is affected by the geothermal gradient of overlying formations. This brings uncertainties to interpreting the resulted DTS deviation attribute. A second approach was presented that de-trends the daily DTS data by removing variations in daily gas production for the entire lateral. This de-trended DTS attribute is independent from the temperature gradient of the overlying formations and changes in production.

We showed that the correlation between production logging measurements and DTS attributes is highest on the production logging day and decreases rapidly and changes its sign from

positive to negative. We suggest that the de-trended DTS attributes, when integrated with other petrophysical and geophysical data and tied to a single one day production log is a valuable attribute that can provide a temporal and spatial perspective to better understand relative production in the subsurface.

Acknowledgements

This research is funded through the U.S.DOE National Energy Technology Lab part of their Marcellus Shale Energy and Environmental Laboratory (MSEEL) (DOE Award No.: DE-FE0024297). We appreciate Northeast Natural Energy LLC. for providing data and technical support. Schlumberger is to be complimented for providing good robust data in the face of multiple technical challenges.

References

1. Amini, S., Kavousi, P. and Carr, T.R., 2017. Application of Fiber-optic Temperature Data Analysis in Hydraulic Fracturing Evaluation--A Case Study in Marcellus Shale: Unconventional Resources Technology Conference (URTEC), doi: 10.15530/URTEC-2017-2686732vb
2. Barber, K., Jansen, M., Nokes, G. and Gatland, R., 1999, Fibre optic monitoring takes the heat off cables: Modern Power Systems, **19**(12), pp.35-37.
3. Brown, G.A., 2006, Monitoring Multilayered Reservoir Pressures and GOR Changes Over Time Using Permanently Installed Distributed Temperature Measurements: In SPE Annual Technical Conference and Exhibition. Society of Petroleum Engineers, SPE 101886. doi: 10.2118/101886-MS
4. Carr, T. R., Thomas H. Wilson, T. H., Payam Kavousi, P., Amini, S., Sharma, S., Hewitt, J., Costello, I., Carney, B.J., Jordon, E., Yates, M., MacPhail, K., Uschner, N., Thomas, M., Akin, S., Magbagbeola, O., Morales, A., Johansen, A., Hogarth, L., Anifowoshe, O., Naseem, K., Hammack, R., Kumar, A., Zorn, E., Vagnetti, R. and Dustin Crandall, D., 2017, Insights from the Marcellus Shale Energy and Environment Laboratory (MSEEL), Proceedings, Unconventional Resources Technology Conference (URTeC) DOI 10.15530-urtec-2017-2670437, p. 1130-1142. https://library.seg.org/doi/abs/10.15530/urtec-2017-2670437
5. Carnahan, B.D., Clanton, R.W., Koehler, K.D., Harkins, G.O. and Williams, G.R., 1999, Fiber optic temperature monitoring technology: In SPE Western Regional Meeting. Society of Petroleum Engineers, SPE 54599. doi: 10.2118/54599-MS
6. Cengel, Y.A. and Boles, M.A., 2002, Thermodynamics: an engineering approach: Sea, 1000, p.8862.
7. Deighton, I., Tibocha, E. and TGS, P.D., 2014, MaxG Basin Temperature Modelling Using Bottom Hole Temperature Datasets: In SPE/AAPG/SEG Unconventional Resources Technology Conference. doi: 10.15530/URTEC-2014-1920520Fridleifsson, I.B., Bertani, R., Huenges, E., Lund, J.W., Ragnarsson, A., and Rybach, L., 2008, The possible role and contribution of geothermal energy to the mitigation of climate change, *in* Hohmeyer, O., and Trittin, T., eds., 2008, IPCC scoping meeting on renewable energy sources: Proceedings, Intergovernmental Panel on Climate Change, Lübeck, Germany: World Meteorological Organization, United Nations Environmental Programme, p. 59–80
8. Frone, Z.S., Blackwell, D.D., Richards, M.C. and Hornbach, M.J., 2015, Heat flow and thermal modeling of the Appalachian Basin, West Virginia: Geosphere, **11**(5), pp.1279-

1290. doi: 10.1130/GES01155.1
9. Ghahfarokhi, P.K., Carr, T., Song, L., Shukla, P. and Pankaj, P., 2018, Seismic Attributes Application for the Distributed Acoustic Szensing Data for the Marcellus Shale: New Insights to Cross-Stage Flow Communication: In SPE Hydraulic Fracturing Technology Conference and Exhibition. Society of Petroleum Engineers, SPE 189888. doi: 10.2118/189888-MS
10. Gonzalez, S., Al Rashidi, H., Pandey, D.C., Al-Mula, Y., Safar, A., Al-Kandari, J., Abdalla, W.A., Gorgi, S. and Patel, D., 2018, Real-Time Fiber-Optics Monitoring of Steam Injection in Unconsolidated High Viscous Formation: In SPE EOR Conference at Oil and Gas West Asia. Society of Petroleum Engineers, SPE 190362. doi: 10.2118/190362-MS
11. Johnson, D.O., Sierra, J.R., Kaura, J.D. and Gualtieri, D., 2006, Successful flow profiling of gas wells using distributed temperature sensing data: In SPE Annual Technical Conference and Exhibition. Society of Petroleum Engineers, SPE 103097. doi: 10.2118/103097-MS
12. Kabir, C.S., Izgec, B., Hasan, A.R., Wang, X. and Lee, J., 2008, Real-time estimation of total flow rate and flow profiling in dts-instrumented wells: In International Petroleum Technology Conference. International Petroleum Technology Conference. doi: 10.2523/IPTC-12343-MS
13. Karaman, O.S., Kutlik, R.L. and Kluth, E.L., 1996, A field trial to test fiber optic sensors for downhole temperature and pressure measurements, West Coalinga field, California: In SPE Western Regional Meeting. Society of Petroleum Engineers, SPE 35685. doi: 10.2118/35685-MS
14. Kavousi, P., Carr, T. R., Wilson, T., Amini, S., Wilson, C., Thomas, M., MacPhail, K., Crandall, D., Carney, BJ., Costello, I., and Hewitt J., 2017, Correlating distributed acoustic sensing (DAS) to natural fracture intensity for the Marcellus Shale. SEG Technical Program Expanded Abstracts 2017: pp. 5386-5390. https://doi.org/10.1190/segam2017-17675576.1
15. Lanier, G.H., Brown, G. and Adams, L., 2003, Brunei Field Trial of a Fibre Optic Distributed Temperature Sensor (DTS) System in a 1,000 m Open Hole Horizontal Oil Producer: In SPE Annual Technical Conference and Exhibition. Society of Petroleum Engineers, SPE 84324. doi: 10.2118/84324-MS
16. Mishra, A., Al Gabani, S.H. and Jumaa Al Hosany, A., 2017, Pipeline Leakage Detection Using Fiber Optics Distributed Temperature Sensing DTS: In SPE Abu Dhabi International Petroleum Exhibition & Conference. Society of Petroleum Engineers, SPE 188407. doi: 10.2118/188407-MS
17. Nath, D.K., Sugianto, R. and Finley, D., 2005, Fiber-optic distributed temperature sensing technology used for reservoir monitoring in an Indonesia steam flood: In SPE International Thermal Operations and Heavy Oil Symposium. Society of Petroleum Engineers, SPE 97912. doi: 10.2118/97912-MS
18. Nath, D.K., Finley, D.B. and Kaura, J.D., 2006, Real-Time Fiber-Optic Distributed Temperature Sensing (DTS)-New Applications in the Oilfield: In SPE Annual Technical Conference and Exhibition. Society of Petroleum Engineers, SPE 103069. doi: 10.2118/103069-MS
19. Ouyang, L.B. and Belanger, D., 2004, Flow Profiling via Distributed Temperature Sensor (DTS) System-Expectation and Reality: In SPE Annual Technical Conference and Exhibition. Society of Petroleum Engineers, SPED 90541 doi: 10.2118/90541-MS
20. Peck, D. and Seebacher, P., 2000, Distributed Temperature Sensing using Fibre-Optics (DTS Systems): Presented to Electricity Engineers's Association Annual Conference,

Auckland, New Zealand.
21. Pinto, M.C., Karale, C. and Das, P., 2013, A simple and reliable approach for the estimation of the Joule-Thomson coefficient of reservoir gas at bottomhole conditions: SPE Journal, **18**(05), pp.960-968, SPE 158116. doi: 10.2118/158116-PA
22. Roy, B.N., 2002, Fundamentals of classical and statistical thermodynamics: John Wiley & Sons.
23. Saputelli, L., Mendoza, H., Finol, J., Rojas, L., Lopez, E., Bravo, H. and Buitriago, S., 1999, Monitoring steamflood performance through fiber optic temperature sensing: In International Thermal Operations/Heavy Oil Symposium. Society of Petroleum Engineers, SPE 54104. doi: 10.2118/54104-MS
24. Smolen, J.J. and van der Spek, A., 2003, Distributed Temperature Sensing: A primer for Oil and Gas Production. Shell.
25. Tolan, M., Boyle, M. and Williams, G., 2001, The use of fiber-optic distributed temperature sensing and remote hydraulically operated interval control valves for the management of water production in the Douglas field: In SPE Annual Technical Conference and Exhibition. Society of Petroleum Engineers, SPE 71676. doi: 10.2118/71676-MS
26. Walker, I. and Carr, D., 2003, Fibre Optic Leak Detection: In Offshore Technology Conference. Offshore Technology Conference. doi: 10.4043/15360-MS
27. Wang, X., Lee, J., Thigpen, B., Vachon, G.P., Poland, S.H. and Norton, D., 2008, Modeling flow profile using distributed temperature sensor (DTS) system: In Intelligent Energy Conference and Exhibition. Society of Petroleum Engineers, SPE 111790. doi: 10.2118/111790-MS
28. Wang, Z., 2012, The uses of distributed temperature survey (DTS) data (Doctoral dissertation, Stanford University).
29. Wheaton, B., Haustveit, K., Deeg, W., Miskimins, J. and Barree, R., 2016, A case study of completion effectiveness in the eagle ford shale using DAS/DTS observations and hydraulic fracture modeling: In SPE Hydraulic Fracturing Technology Conference. Society of Petroleum Engineers, SPE 179149. doi: 10.2118/179149-MS

UNCONVENTIONAL RESOURCES TECHNOLOGY CONFERENCE
FUELED BY SPE • AAPG • SEG

Appendix 2

URTeC: 2902641

A Fiber-optic Assisted Multilayer Perceptron Reservoir Production Modeling: A Machine Learning Approach in Prediction of Gas Production from the Marcellus Shale

Payam Kavousi Ghahfarokhi*[1], Timothy Carr[1], Shuvajit Bhattacharya[2], Justin Elliott [1], Alireza Shahkarami [3]; Keithan Martin[1]:1. West Virginia University, 2. University of Alaska Anchorage, 3. Saint Francis University.

Copyright 2018, Unconventional Resources Technology Conference (URTeC) **DOI 10.15530/urtec-2018-2902641**

This paper was prepared for presentation at the Unconventional Resources Technology Conference held in Houston, Texas, USA, 23-25 July 2018.

The URTeC Technical Program Committee accepted this presentation on the basis of information contained in an abstract submitted by the author(s). The contents of this paper have not been reviewed by URTeC and URTeC does not warrant the accuracy, reliability, or timeliness of any information herein. All information is the responsibility of, and, is subject to corrections by the author(s). Any person or entity that relies on any information obtained from this paper does so at their own risk. The information herein does not necessarily reflect any position of URTeC. Any reproduction, distribution, or storage of any part of this paper by anyone other than the author without the written consent of URTeC is prohibited.

Abstract

This study utilized the recorded data of a distributed temperature sensing (DTS) and distributed acoustic sensing (DAS) fiber-optic system from a gas producing horizontal well in the Marcellus Shale, in Northern West Virginia. A predictive data-driven model was developed to understand the well's performance and forecast the gas production using DTS data and daily flowing time as dynamic inputs, from May 2016 to May 2018. We used 1320 DTS measurements along the lateral of the well MIP-3H for each day and upscaled to a stage scale by an averaging method. A multi-layer perceptron neural network (MLPNN) was trained with stage-based daily DTS data, and daily flowing time to predict gas production for the next day. We carried out a sensitivity analysis by removing each stage DTS attribute from the input dataset to identify the most influential stages in predicting gas production. The sensitivity analysis (SA) shows that several stages carry higher weights in predicting gas production, while several stages have less impact on prediction accuracy. In contrast to DTS, DAS data was only recorded during hydraulic fracturing of the well. DAS energy variance attribute, which could be inversely related to stage stimulation efficiency, was computed for each stage and compared with the results of the neural network SA. Stages with higher variance in DAS energy (less efficient stimulation) have less effect on neural network accuracy. This relationship is more significant for stages that are completed with limited entry approach in zones with similar minimum horizontal stress. The results of the sensitivity analysis was also compared with flow scanner production logging data. Results suggests that DAS data is more correlated with sensitivity analysis results than production logging data.

Introduction

Well MIP-3H near Morgantown, West Virginia was studied for the prediction of the daily gas production from the Marcellus Shale through use of an artificial neural network (Figure 1). The 28-stage horizontal MIP-3H well, drilled as a part of the Marcellus Shale Energy & Environment Laboratory (MSEEL) project, has multi-scale and multi-sensor-based spatio-temporal data, such as DTS, DAS, production log from flow scanner production log, geomechanical logs, surface pressure, and surface temperature. DAS and DTS are recorded by a fiber-optic cable attached to the outer part of the production casing, and has recorded the temperature around the fiber to date. However, the DAS data (strain) is only available for the stimulation process and cannot be used as a dynamic input for reservoir modeling.

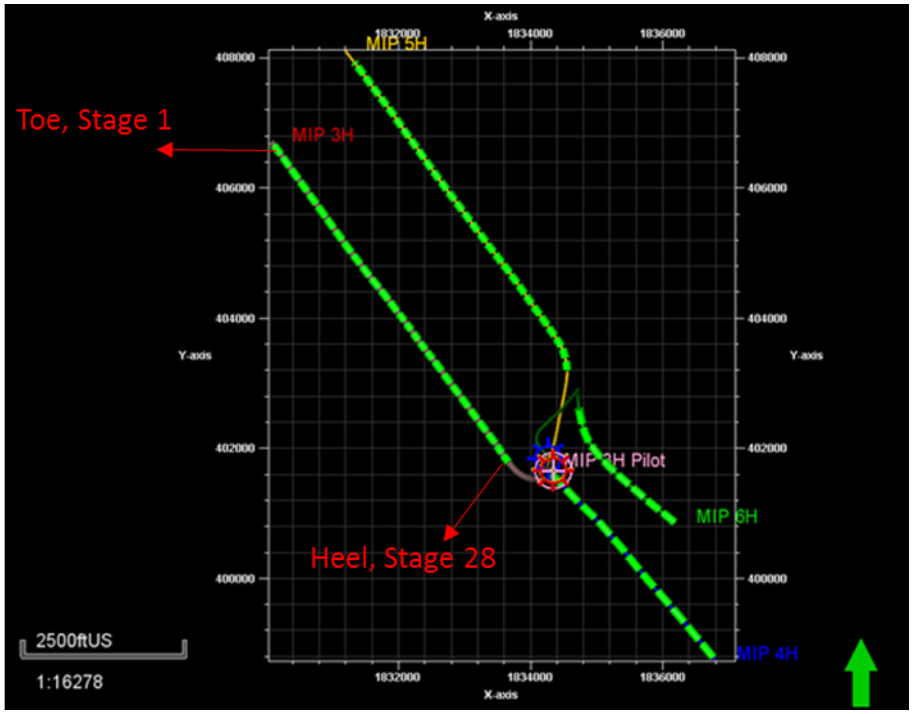

Figure 17: MSEEL project consists of 4 horizontal well in the Marcellus Shale. Well MIP-3H is the only well with the fiber-optic data

DTS has provided continuous multi-point reservoir temperature monitoring along the lateral of the MIP-3H to date. This unique dataset can be analyzed by artificial intelligence algorithms such as neural network to predict gas production from the MIP-3H. Artificial neural networks (ANN) have been of increasing popularity because of their capabilities in efficiently recognizing extremely complex patterns without making any assumptions about the data being studied (Keshavarzi et al., 2010, Zheng et al., 2014). ANNs provide a flexible way to handle regression and classification problems without explicitly stating the relationship between input and output parameters (Mishra and Datta-Gupta, 2017). Neural networks have a large range of applications as they have been used in varying fields of study. Specifically, in engineering and geology, they have been shown to have the capability to increase the performance of reservoir simulation by using enhancing sparse data (Isaiah et al., 2013). Application of artificial intelligence for unconventional oil and gas resources has also been conducted by various researchers. Mohaghegh et al., (2011) carried out data mining techniques to evaluate shale production. More recently, Anderson et al., (2016) showed the application of the machine learning in classifying hydraulic fractures in the Marcellus Shale. The reservoir production forecast has also been implemented for several unconventional Shales (Gaurav, 2017; Cao et al., 2016). However, usage of fiber-optic data as a valuable downhole dynamic input for the neural network has not been undertaken.

Fiber optic is an advanced non-invasive hydraulic fracture stimulation monitoring tool, which can record temperature and strain around the well. Fiber-optic systems works based on optical time-domain reflectometry (OTDR). A transmitter sends a light pulse into the fiber; inherent impurities in the glass core, scatter back the light toward the detector. The power and the wavelength of the backscattered light enables the detector to estimate the temperature, strain, or the vibro-acoustic on the fiber (Tanimola and Hill, 2009). DTS technology measures the “Stokes” and “Anti-Stokes” components of the backscattered spectrum (Figure 2). The “Anti-Stokes” component is sensitive to the temperature, while the Stoke component is temperature independent. Thus, a ratio of “Anti-Stokes” and “Stokes” power provides a measure of temperature (Molenaar et al., 2012). The frequency of the Brillion stokes and anti-stokes changes as a function of temperature and strain. Thus, the axial strain of the fiber can also be recorded during the hydraulic fracturing. Distributed acoustic sensing (DAS) measures the axial strain of the fiber; however, DAS data are usually available only for the stimulation time and not for subsequent reservoir production. In contrast, DTS data is more common to be recorded during the reservoir production. Unlike SEGY format DAS data, DTS data can be extracted as ASCII or CSV format without further processing.

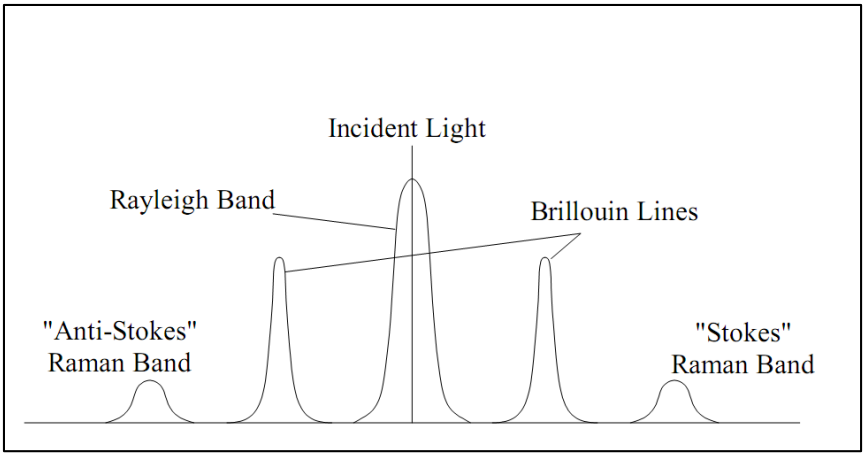

Figure 2: The backscattered light spectrum has Rayleigh Band, Brillouin bans, and Raman bands. Rayleigh and Brillouin bands are sensitive to strain while Raman bands are sensitive to the temperature around the fiber (courtesy Carnahan et al., 1999).

Discussions and Results

Ghahfarokhi et al., (2018) used the DAS and DTS data to show hydraulic connections between several stages in the MIP-3H well. The sum of DAS traces squared amplitudes can be used to calculate DAS energy attribute (Kavousi et al., 2018). The energy attribute indicates that a more uniform hydraulic fracturing was implemented for Stage 18 and Stage 17 than Stage 10 (Figure 3).

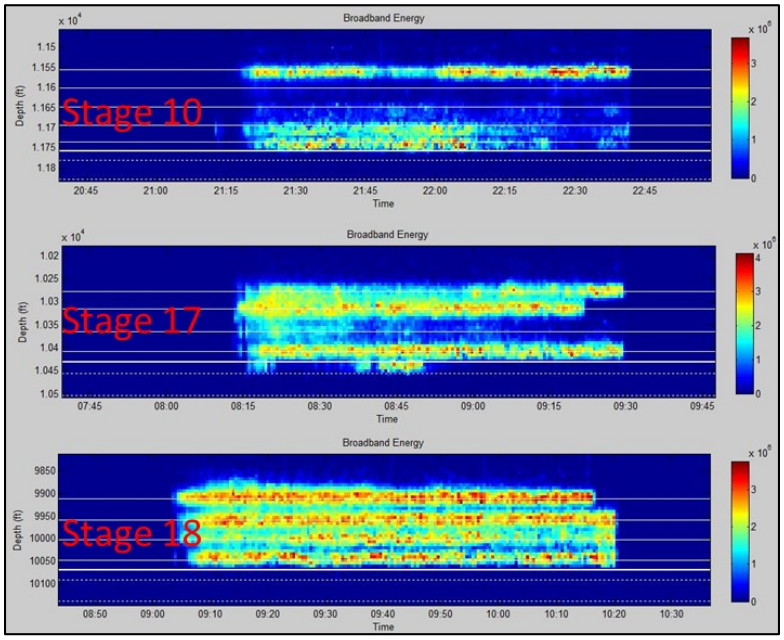

Figure 3: DAS energy attributes of three stages of the MIP-3H are shown. Note that DAS energy attribute has no unit.

The MIP-3H well in the Marcellus Shale continues to record DTS data along the lateral, to date. The raw DTS data can be visualized in a waterfall plot (Figure 4). Fiber-optic DTS system has recorded temperature at more than 1320 points with spacing of 2-3ft (0.6-0.9 m) along the lateral of the well for past two years; yielding almost 1 million DTS data points for two years. This amount of data provides the opportunity to use a neural network algorithm for predicting gas production from MIP-3H. MIP-3H gas production was constrained until late 2017, and well was producing for only several hours per day due to limited market demand. The hours of production of each day is equivalent to the

daily flowing time throughout this paper. In addition to DTS, we used flowing time as an auxiliary input for neural network to predict gas production for the next day.

We upscaled the DTS measurements to stage scale by averaging the DTS data between top and bottom of each stage (Figure 5). The waterfall plot shown in Figure 5 shows that the well is cooler in the toe than the heel. Also, stages 17, 18, and 19 are consistently cooler that the adjacent stages. These results could be related to Joule-Thompson cooling effect, which occurs as natural gas expands from the higher-pressure reservoir into the lower pressure production casing.

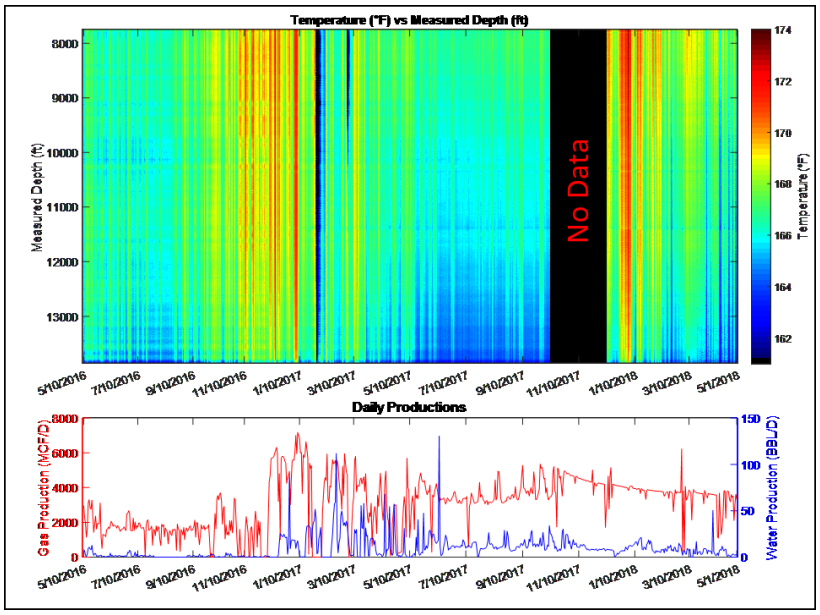

Figure 4: DTS data until May 2018 are compiled in a waterfall plot. The toe of the well is cooler than the heel of the well.

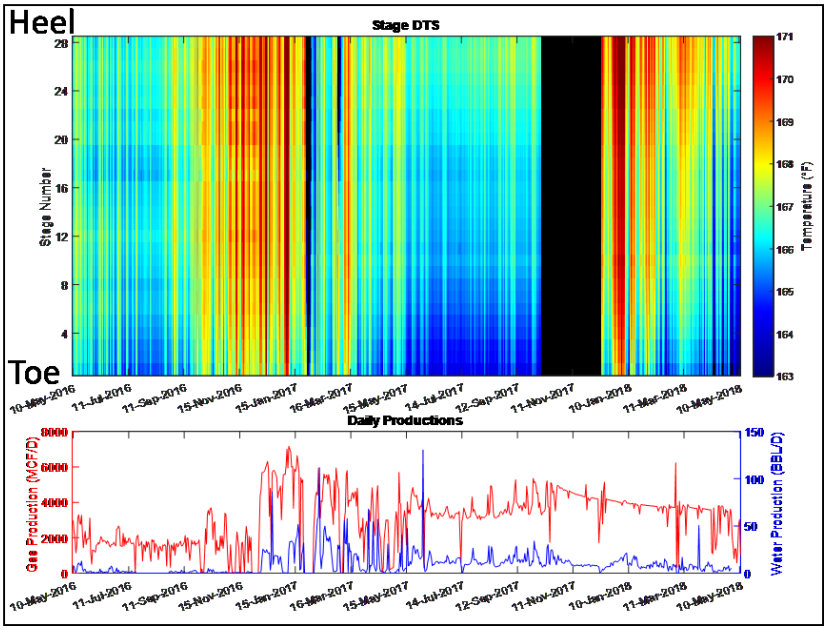

Figure 5: The DTS data in figure 4 are upscaled to the stage scale.

The upscaled DTS attribute is used as an input for a multi-layer perceptron ANN algorithm with 3 hidden layers (Figure 6). We optimized learning rate, momentum, and epoch (number of iterations) for enhanced learning of data

pattern and testing it. The training, validation, and testing errors were carefully inspected to avoid ANN overfitting. The optimal values from numerous experiment give a learning rate, momentum, and epoch as 0.05, 0.11, and 500, respectively.

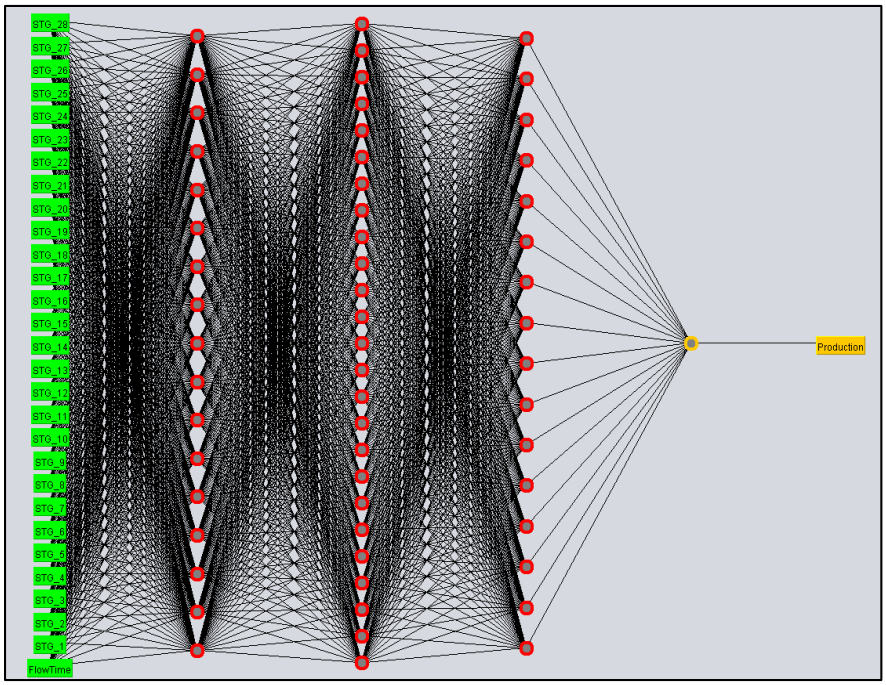

Figure 6: ANN structure with three hidden layers used for daily gas production prediction in this study. Note that input parameters are from previous days of the predicted productions.

The designed neural network uses dynamic inputs as shown in Table 1 to predict gas production of the next day. Constrained production from the well prior to late 2017 has caused the well to not show a typical declining daily production. Although the flow time input helps the neural network to learn the constraint on gas production, training is not still very accurate for sudden very high or very low productions (Figure 7). The trained neural network is then applied to 102 days of the test data (Figure 8).

Table 2: The dynamic inputs for the neural network. Note that daily gas rate is predicted from input data of its previous day.

Inputs	Output
Upscaled DTS (t-1) for stage 1 to 28	**Gas production (t)**
Flowing time (t-1)	

A neural network sensitivity analysis was then carried out by removing each input from the network and evaluating changes in the mean absolute error of the network (Figure 9). The neural network sensitivity analysis of DTS data suggests that the more influential stages such as 17, 18, 19, 20, and 28 would result in a higher mean absolute error (MAE) in network predictions if removed from the input dataset. In contrast, Stage 1 removal will decrease MAE of the neural network. Production logging was carried out on March 02, 2017 to assess the gas production share of each stage. Figure 4 and Figure 5 shows that downhole reservoir temperature is very sensitive to water and gas production and the observed stage temperature varies by time. Hence, a production log might have limited capability to be a contemporary indication of individual stage production.

We compare production log data and DAS variance attribute with the neural network sensitivity results to evaluate whether there are any relationships between these variables (Table 2). Results show that DAS variance attribute is

inversely related to MAE of neural network. A smaller DAS variance for a stage could suggests a more uniform hydraulic fracturing in all clusters while a higher DAS variance implies that not all the clusters are hydraulically fractured (Figure 3). Thus, a stage with a lower DAS variance could cause a higher neural network MAE when removed from the predictions (Figure 10a). Stage 13 to 19, known as the engineered stages, are stimulated by a limited entry approach in zones with similar minimum horizontal stress. The inverse relationship between DAS variance and neural network MAE is more pronounced in engineered stages (Figure 10b). One the other hand, the production log does not show any significant relationships with neural network MAE (Figure 11a and 11b).

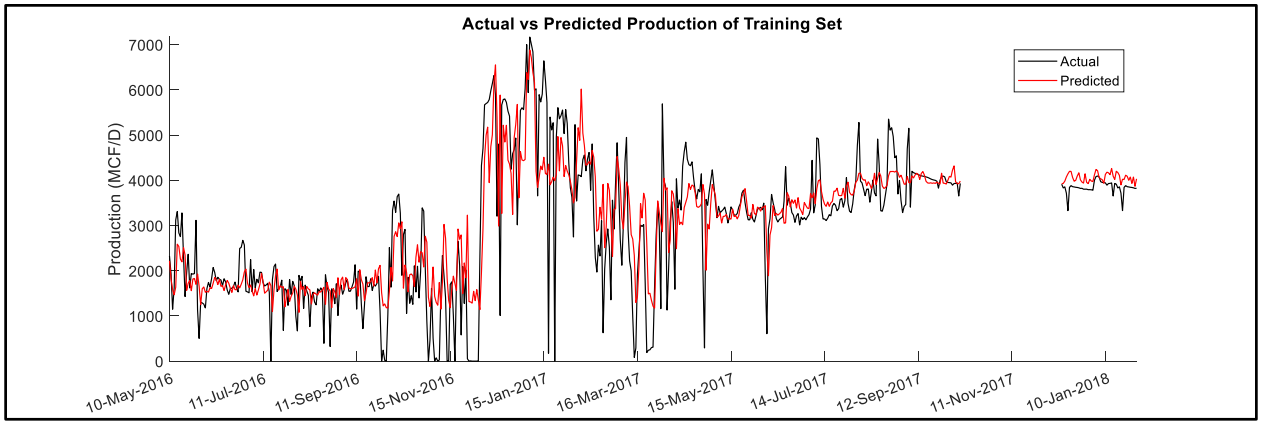

Figure 7: The network is trained for 508 days using dynamic input data.

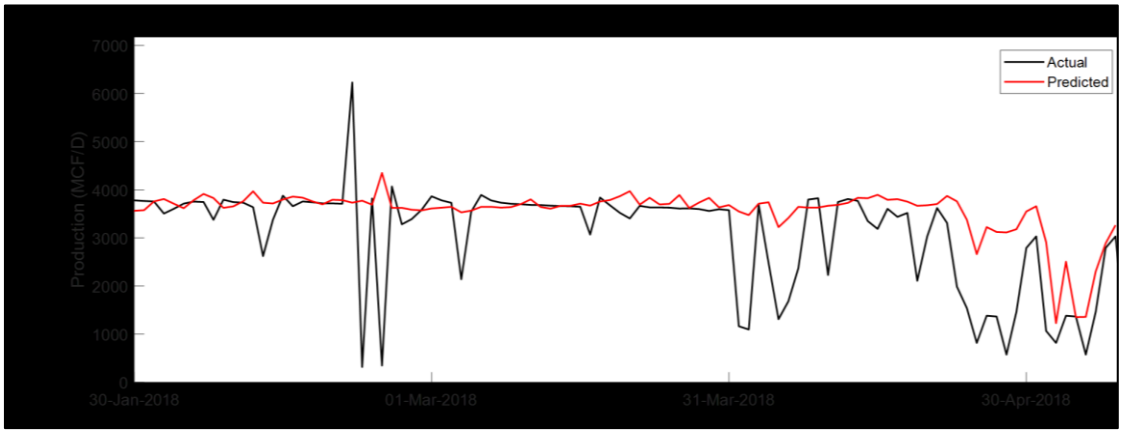

Figure 8: The test data for 102 days of the well daily gas production.

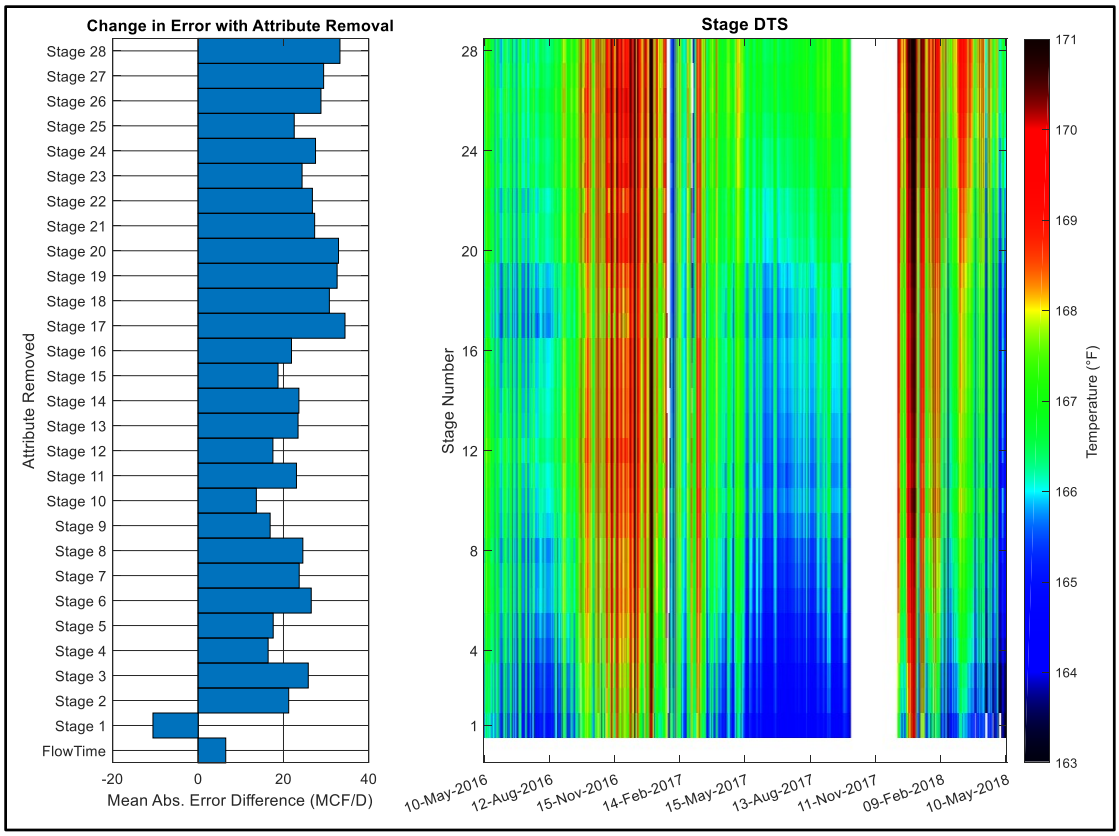

Figure 9: A sensitivity analysis for dynamic inputs suggest that casing pressure and tubing head pressure are amongst the most important factors for predicting gas production.

Table 3: The sensitivity analysis results are shown with DAS variance and production log data for all 28 stages.

Stage number	Sensitivity analysis error difference	DAS variance	Production log (MCF/d)
28	33.2344	0.084507042	50
27	29.4075	0.481690141	84
26	28.782	0.430985915	67
25	22.5155	0.346478873	158
24	27.5071	0.295774648	192
23	24.355	0.43943662	272
22	26.774	0.346478873	389
21	27.304	0.194366197	198
20	32.8965	0.566197183	99
19	32.5699	0.21971831	119
18	30.7536	0.109859155	231
17	34.4187	0.016901408	250
16	21.8756	0.38028169	378
15	18.7224	0.464788732	59
14	23.611	0.236619718	203
13	23.4141	0.185915493	268
12	17.5225	0.785915493	242
11	23.0408	0.549295775	316
10	13.6376	0.667605634	190
9	16.8706	0.228169014	167
8	24.5391	0.684507042	153
7	23.6815	0.473239437	142
6	26.5018	0.718309859	256
5	17.5871	0.709859155	310
4	16.3985	0.709859155	75
3	25.8073	0.43943662	58
2	21.2219	0.532394366	256
1	-10.5889	0.701408451	251

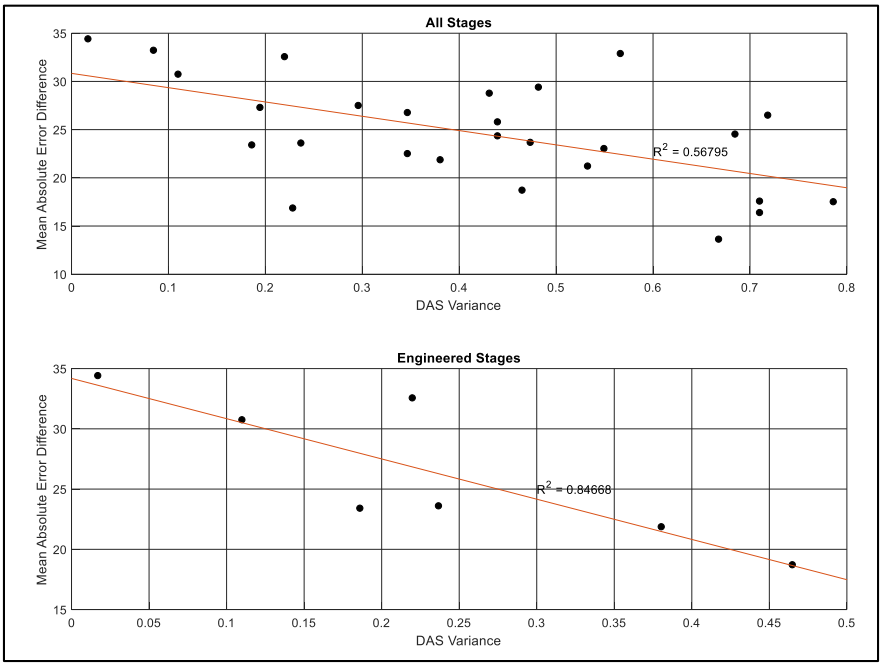

Figure 10: a) The DAS variance of each stage vs. MAE variations of the neural network if the stage is removed from the input dataset. b) The correlation for engineered stage show a significant negative relationship between DAS variance and MAE variations.

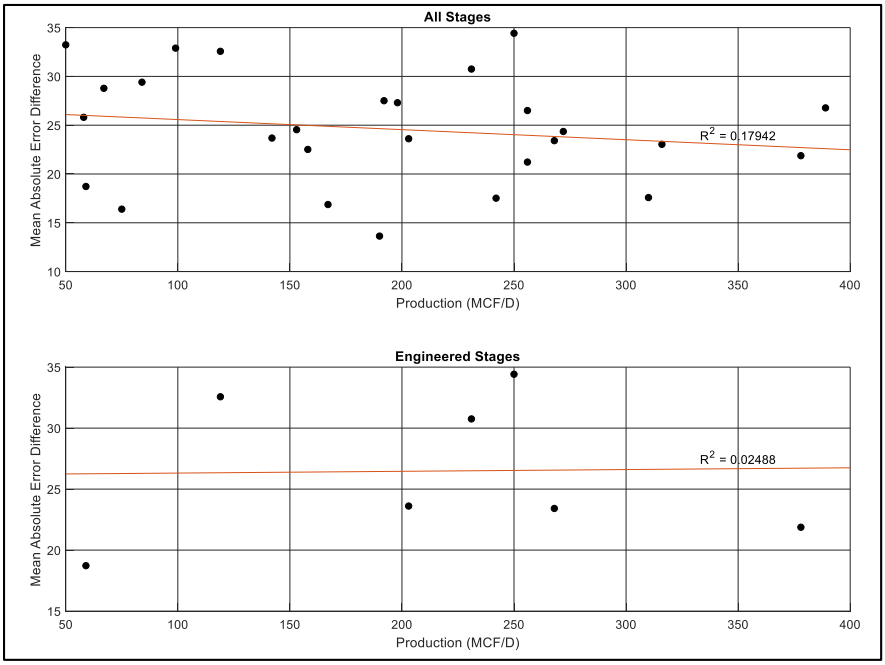

Figure 11: a) The production log data of each stage vs. MAE variations of the neural network if the stage is removed from the input dataset. b) The correlation for engineered stage does not show a significant negative relationship between production log results and MAE variations.

Conclusions

Key conclusions from this study can be summarized as following:

1. The study shows that continuous stream of fiber optic data (DTS) can be used to predict gas production of an unconventional shale reservoir.
2. Sensitivity analysis reveals the importance of several stages. A higher MAE when the stage is removed from the network suggest more importance of the removed stage.
3. DAS energy variance attribute is inversely correlated with the stage importance from the sensitivity analysis. This finding is more noticeable in engineered stages.
4. DTS data until May 2018 show that downhole temperature is dynamic parameter and fluctuate with production within any stage. A single day production logging is not a contemporary indication of stages productions.
5. Production log did not show a significant correlation with stage importance from the sensitivity analysis. This ratifies the idea that production log is a sample of production distribution in time rather than a constant share of production throughout the life of the reservoir.

Acknowledgments

This research is funded through the U.S.DOE National Energy Technology Lab part of their Marcellus Shale Energy and Environmental Laboratory (MSEEL) (DOE Award No.: DE-FE0024297). We appreciate the Northeast Natural Energy LLC. For providing data and technical support and Schlumberger for access to the fiber-optic data. We thank Machine Learning Group at the University of Waikato for providing Weka software. We also appreciate license for Mathwork MATLAB software.

References

Anderson, R.N., Xie, B., Wu, L., Kressner, A.A., Frantz Jr, J.H., Ockree, M.A., Brown, K.G., Carragher, P. and McLane, M.A., 2016. Using Machine Learning to Identify the Highest Wet Gas Producing Mix of Hydraulic Fracture Classes and Technology Improvements in the Marcellus Shale. Unconventional Resources Technology Conference (URTEC).

Cao, Q., Banerjee, R., Gupta, S., Li, J., Zhou, W. and Jeyachandra, B., 2016, June. Data driven production forecasting using machine learning. In SPE Argentina Exploration and Production of Unconventional Resources Symposium. Society of Petroleum Engineers.

Carnahan, B.D., Clanton, R.W., Koehler, K.D., Harkins, G.O. and Williams, G.R., 1999, January. Fiber Optic Temperature Monitoring Technology. In SPE Western Regional Meeting. Society of Petroleum Engineers.

Gaurav, A., 2017, September. Horizontal Shale Well EUR Determination Integrating Geology, Machine Learning, Pattern Recognition and Multivariate Statistics Focused on the Permian Basin. In SPE Liquids-Rich Basins Conference-North America. Society of Petroleum Engineers.

Ghahfarokhi, P.K., Carr, T., Song, L., Shukla, P. and Pankaj, P., 2018, January. Seismic Attributes Application for the Distributed Acoustic Sensing Data for the Marcellus Shale: New Insights to Cross-Stage Flow Communication. In SPE Hydraulic Fracturing Technology Conference and Exhibition. Society of Petroleum Engineers.

Isaiah, J., Schrader, S., Reichhardt, D. and Link, C., 2013, March. Performing Reservoir Simulation with Neural Network Enhanced Data. In SPE Digital Energy Conference. Society of Petroleum Engineers.

Kavousi, P., Carr, T., Wilson, T., Amini, S., Wilson, C., Thomas, M., MacPhail, K., Crandall, D., Carney, B.J., Costello, I. and Hewitt, J., 2017. Correlating distributed acoustic sensing (DAS) to natural fracture intensity for the Marcellus Shale. In SEG Technical Program Expanded Abstracts 2017 (pp. 5386-5390). Society of Exploration Geophysicists.

Keshavarzi, R., Jahanbakhshi, R., Nadgaran, H. and Aliyari, M., 2010, January. A Neural Network Approach for Predicting the Penetration Depth During Laser Perforation In Limestone. In 44th US Rock Mechanics Symposium and 5th US-Canada Rock Mechanics Symposium. American Rock Mechanics Association.

Mishra, S., Datta-Gupta, A., 2017. Applied Statistical Modeling and Data Analytics, Elsevier, 237.

Mohaghegh, S., D., Grujic, O., Zargari, S., et al. 2011. Modeling, History Matching, Forecasting, and Analysis of Shale- Reservoir Performance Using Artificial Intelligence. Presented at the SPE Digital Energy Conference and Exhibition, The Woodlands, Texas, USA, 19–21 April. SPE-143875-MS. https://doi.org/10.2118/143875-MS.

Molenaar, M.M., Hill, D., Webster, P., Fidan, E. and Birch, B., 2012. First downhole application of distributed acoustic sensing for hydraulic-fracturing monitoring and diagnostics. SPE Drilling & Completion, 27(01), pp.32-38.

Rickman, R., Mullen, M.J., Petre, J.E., Grieser, W.V. and Kundert, D., 2008, January. A practical use of shale petrophysics for stimulation design optimization: All shale plays are not clones of the Barnett Shale. In SPE Annual Technical Conference and Exhibition. Society of Petroleum Engineers.

Tanimola, F. and Hill, D., 2009. Distributed fibre optic sensors for pipeline protection. Journal of Natural Gas Science and Engineering, 1(4), pp.134-143.

Zheng, Z.H., Kavousi, P. and Di, H.B., 2014. Multi-attributes and neural network-based fault detection in 3D seismic interpretation. In Advanced Materials Research (Vol. 838, pp. 1497-1502). Trans Tech Publications.

Appendix 3

Manuscript submitted to the Journal Interpretation.

Integrating Distributed Acoustic Sensing (DAS) and Borehole 3C Geophone Array Data to Identify Long-Period Long-Duration Seismic Events during Stimulation of a Marcellus Shale Gas Reservoir

Payam Kavousi Ghahfarokhi, West Virginia University, Morgantown, WV
(pkavousi@mail.wvu.edu)
Thomas Wilson, Morgantown, WV
(tom.wilson@mail.wvu.edu)
Timothy Carr, West Virginia University, Morgantown, WV
(tim.carr@mail.wvu.edu)
Abhash Kummar, NETL DOE, Pittsburgh, PA
(Abhash.Kumar@netl.doe.gov)
Richard Hammack, NETL DOE, Pittsburgh, PA
(Richard.Hammack@netl.doe.gov)
Haibin Di, Georgia Tech University, Atlanta, GA
(haibin.di@ece.gatech.edu)

ABSTRACT

Microseismic monitoring, fiber-optic distributed acoustic sensing (DAS), and distributed temperature sensing (DTS) observations were made during the hydraulic fracture stimulation of the MIP-3H well in the Marcellus Shale in northern West Virginia. DAS and DTS data measure strain and temperature, respectively, along a fiber optic cable located behind the casing of the well. The presence of long-period long-duration (LPLD) events, similar in appearance to tectonic tremors, is documented in the borehole geophone data of one of the stimulated stages in the MIP-3H. In addition, low frequency events were recorded by the surface seismograms. LPLD events are generally overlooked during the conventional processing of microseismic data, but they represent significant non-brittle deformation produced during hydraulic fracture stimulation. 160 pre-existing fractures and two faults of suboptimal orientation are noted in the image logs of the studied stage. We identified two low-frequency events of large time duration (several hundred seconds) by comparing the borehole geophone data and DAS amplitude spectra of one of the stages at MIP-3H. These low frequency events have low amplitudes, lack of clear impulsive arrivals, and noise-like characteristics and are interpreted as LPLD events. The spatial and temporal similarities of these events indicate that DAS data could be used to identify LPLD events during hydraulic fracture stimulation.

INTRODUCTION

Hydraulic fracturing of unconventional shale reservoirs is necessary to enhance the reservoir permeability. Hydraulic fracturing has been undertaken by various operators since 1940s (Montgomery and Smith, 2010). Companies carry out a multi-stage perforation followed by high pressure fluid/proppant slurry injection to create long hydraulic fractures within low permeability

reservoirs. These hydraulic fractures combined with significant stimulation of the bounding natural fracture network increase the stimulated reservoir volume and subsequent reservoir production. The present-day stress orientation within the reservoir exerts the greatest influence on the direction of hydraulic fracture growth. However, the density, orientation, and openness of natural fractures/faults can also affect the direction and complexity of hydraulic fracture propagation.

Brittle failure along pre-existing fractures generates small magnitude microseismic events (MSE) as high frequency seismic waveforms with clear P and S arrivals. These microseismic events are interpreted to result from shear slip on pre-existing fractures and faults in vicinity of induced hydraulic fractures (Das and Zoback, 2013a; Rutledge and Philips, 2003; Warpinski et al., 2004). Although microseismicity is used as a direct measure to calculate stimulated reservoir volume, however, this correlation with stimulated volume (SRV) or cumulative production is debatable (Sicking et al., 2012; Wilson et al., 2016). Energy balance between microseismic events and injection energy has been compared in several researches (Kavousi et al., 2017; Kumar et al., 2017b; Warpinski et al., 2012; Boroumand and Eaton, 2012). Results show that the energy released in the form of microseismic events is only a small portion of the energy supplied to the reservoir during hydraulic fracture stimulation as estimated from treatment pressure and injection volume. This deficit in the energy budget estimate suggests an alternate deformation mechanism that likely consumes energy during hydraulic fracturing. Recently, LPLD events are considered to be a potential source for energy consumption by slow shear slip on relatively large faults (Das and Zoback, 2011, 2013a; Mitchell et al., 2013; Kwietniak, 2015). Das and Zoback, (2013a) showed that LPLD events release one to two orders of magnitude more energy than picked microseismic events and potentially affect the stimulation of the reservoirs much more than microearthquakes. Zoback et al., (2012) showed that fault orientation relative to the present-day SH_{max} could determine the slip behavior. They proposed through modeling that misaligned faults undergo slow slip while well-oriented faults immediately slip when triggered by increased fluid pressure. The reason might be that fluid pressure propagates faster along well-oriented faults than misaligned faults and triggers a rapid slip. Das and Zoback (2013a) suggested that LPLD events result from slow shear slip on pre-existing faults that are unfavorably oriented in the present-day stress field or have high clay content.

Das and Zoback (2011) analyzed borehole seismic data from hydraulic fracturing in the Barnett Shale. They interpreted the LPLD events as low frequency energy release (between 10Hz to 80HZ) that lasts from tens of seconds to minutes. The long-period long-duration events are usually characterized by low amplitude arrivals, with highly emergent waveform characteristics, making the phase picking very difficult (Das and Zoback, 2011; Eaton et al, 2013). LPLD seismic events have similarities with observed tectonic tremors in subduction zones and transform faults (Caffagni et al., 2015). Tectonic tremors are assumed to be accompanied by slow shear slip of plates in transform faults or subduction zones (Obara, 2002; Shelly et al., 2006; Nadeau and Guilhem, 2009). Das and Zoback (2011) suggested that similar phenomena could happen during hydraulic fracturing when there is slow slip on pre-existing faults of sub-optimal orientation. They proposed that this non-brittle deformation process could contribute to reservoir production by significant permeability enhancement. Mitchell et al., (2013) analyzed the seismic waveforms from surface and downhole geophone arrays during hydraulic fracturing of a horizontal well in the West Texas Cline Shale to detect LPLDs. The spectrogram of the stacked waveforms from the downhole array revealed the presence of several LPLDs; however, no LPLDs were detected in the surface recordings, most likely because of low signal strength. Eaton et al. (2013) studied seismic waveforms recorded during the hydraulic fracturing of a well in a Montney gas reservoir in British Colombia and identified several LPLD events. They observed LPLD events at frequencies less than 10 HZ and proposed that complexity of pre-existing natural fractures could affect the spectral

frequency of LPLD events. Even with all these leading evidences of LPLD occurrence at various hydraulic fracturing sites, it is critical to rule out the possibility of mispicking non-fracturing related seismicity as LPLD events. Recently, Cafagni et al. (2015) and Zecevic et al. (2016) pointed out regional seismicity as a potential pitfall in the identification and characterization of LPLD events due to their similar waveform characteristics, overlapping frequency content, and apparent velocity. For regional earthquakes, codas of P- and S-waves that are multiply reflected and scattered seismic wave may also produce the effect of long duration signals with ambiguous arrival time similar to LPLD events (Aki, 1969; Aki and Chouet, 1975). In the recent past, Kumar et al., (2017a) identified several LPLDs in the surface seismic data recorded during hydraulic fracturing of Marcellus Shale wells at the current study site in Monongalia County, West Virginia. To avoid any misinterpretation between LPLD event and known or unknown regional earthquakes, Kumar et al. (2017a) analyzed seismic waveforms from the nearest stations of the USArray and cross checked regional earthquakes. Kumar et al. (2017a) found no temporal correlation between the LPLD events detected from surface broadband stations and known catalog events, suggesting a local source of deformation as the cause of LPLD events.

Toward this end, we examined the ability of DAS (Distributed Acoustic Sensing) and DTS (Distributed Temperature sensing) instruments to record LPLD events during hydraulic fracturing of a horizontal Marcellus Shale well in Monongalia County of West Virginia. Fiber-optic DAS and DTS data record strain or strain rate and temperature around the wellbore, respectively. Fiber-optic sensing technology has been used by the oil and gas companies since 1990s to monitor steam injection, injection profiling, acid injection profiling, and hydraulic fracture diagnostics (Karaman et al., 1996; Rahman et al., 2011; Glasbergen et al., 2010; Sierra et al., 2008; Holly and Kalia, 2015). DAS is sensitive to the vibrations in the local environment around the fiber and provides a measure of the relative axial strain or strain rate of the optical fiber (Tanimola and Hill, 2009).

The frequency content of DAS data has been studied by several researchers. Ghahfarokhi et al., (2018) showed that seismic attributes such as instantaneous frequency, dominant frequency, and energy could be applied to DAS data to better monitor hydraulic fracturing. Jin and Roy (2017) showed that low frequency (<0.05 HZ) strain rate DAS signals could reveal information about the stress shadow, fracture length, density, and width. However, low frequency DAS data can be significantly affected by temperature variations around the fiber during cross-stage flow communications. This requires the fiber cable to be installed in a separate monitoring well rather than the stimulated well.

DAS fiber-optic data have also been used to detect microseismic events with high accuracy (Webster et al., 2016). Karrenbach et al. (2017) used DAS data to locate microseismic events and found similar event detection ability as sensors deployed in the monitoring well. A field trial of vertical seismic profiling (VSP) by DAS fiber-optic was conducted at the Aquistore site in Saskatchewan, Canada. Olofsson and Martinez (2017) showed that the VSPs from processed DAS fiber-optic data of three different vendors are similar to VSP data recorded by conventional geophone arrays.

In this study, we use borehole geophone data and DAS data collected during stimulation of the MIP-3H well close to Morgantown, WV (Figure 1). The DAS data were recorded in fiber deployed along the length of the MIP-3H horizontal well and the borehole seismic data were recorded by geophones deployed in a vertical monitoring well MIP-SW (Figure 1). We propose that a Fourier transform of fiber-optic DAS data could show LPLD events concurrently with microseismic activity. Moreover, a temperature variation might be observed simultaneously with LPLD events on distributed temperature sensing (DTS) data because of the hydraulic connections through fractures and faults. It is very unlikely that regional earthquakes can alter the temperature

around the fiber. So, the combined analysis of fiber-optic DAS and DTS can be used to differentiate LPLD events produced by stimulation and those produced by regional earthquakes.

Figure 18: Marcellus Shale Energy and Environment Laboratory (MSEEL) just outside Morgantown, West Virginia, USA. The MSEEL site consists of four horizontal production wells operated by Northeast Natural Energy LLC. (MIP-3H, MIP-4H, MIP-5H, MIP-6H), two pilot holes (MIP-3 and MIP-4), a micro-seismic observation well (MIP-SW), and a grid of five surface seismometers (triangles).

DATASETS AND METHODOLOGY

In 2015 two horizontal wells, MIP-3H and MIP-5H, were hydraulically fractured in the Marcellus Shale close to Morgantown (Figure 1), West Virginia in the eastern United States. The lateral of the MIP-3H well is drilled just above the Cherry Valley Limestone in the Upper Marcellus Shale. A permanent fiber optic cable was deployed in the MIP-3H well to acquire DAS and DTS data throughout the stimulation of all 28 stages along this well. A total of 493 DAS channels recorded vibrations along the lateral with a spacing of ~16.74ft (5.1m) and a gauge length of 64ft. DTS data was recorded with a higher resolution of ~1ft (30.48cm) during hydraulic fracture stimulation. In addition, microseismic activity during hydraulic fracturing was monitored

by the vertical MIP-SW well, which has twelve 3C geophones separated by 100ft interval (Figure 2). The total vertical aperture of the geophone array was 1100ft (335.28m). The focus of this study is to integrate DAS, DTS, and borehole seismic data from the MIP-3H well stimulation and inspect theses data for potential LPLD events. We compute the spectrogram of geophone channels deployed in the vertical well and compare them with the spectrogram of the DAS channels for stage 10 to detect LPLD events. The stage 10 is chosen for this study because it has the most pre-existing fractures and faults amongst the 28 stages.

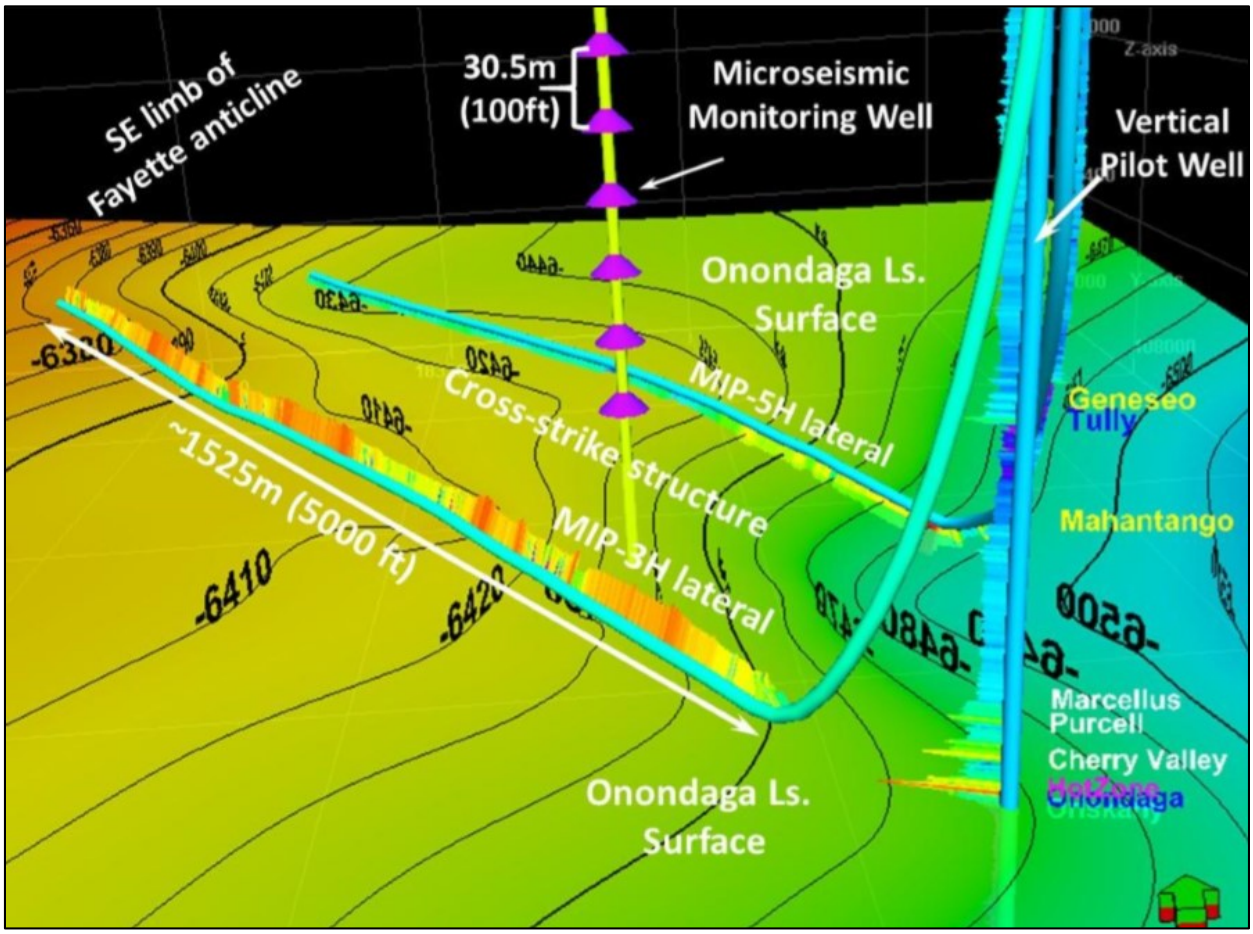

Figure 19: 3D view of wells located in the study area. DAS data were collected in the MIP-3H. Contours on the top of the Onondaga Limestone (Base of Marcellus Shale) are in feet subsea. Gamma ray log responses are shown in the vertical pilot well and the two horizontal wells. Geophone locations are shown in the lower part of the microseismic monitoring well.

Stage 10 with two faults and 160 pre-existing fractures was observed to have the most fractures and faults from the formation image logs of the MIP-3H. We believe that the presence of faults and fractures along the stage 10, complimented by high clay content of the Marcellus Shale could facilitate the generation of LPLD events through slow-slip. We evaluate the DAS, DTS, and microseismic data of stage 10 stimulation to detect LPLD events.

Ghahfarokhi et al., (2018) evaluated the DTS (figure 3a) and DAS data of the Stage 10 stimulation for Well 3H to unravel low frequency time intervals in the DAS data. The instantaneous frequency attribute (Figure 3b) was calculated from a Hilbert transform of the DAS signals from stage 10 stimulation. They proposed that the temperature rise in Stage 9 (Figure 3a) is because of the fluid communication from Stage 10 through pre-existing faults and fractures that are misaligned with the present-day stress regime. This abnormal temperature rise in Stage 9 is also corresponding to low frequency time intervals on instantaneous frequency attribute of the DAS data (showed by arrows in Figure 3b). Jin and Roy (2017) suggested that temperature variations could affect the low frequency components of DAS data. The low frequency time intervals in Figure 3b are also concurrent with increased microseismic events recorded at the downhole geophones in the monitoring well (Figure 3c). Microseismic events were also recorded during the leakoff period and are concurrent with low instantaneous frequency in the DAS data.

Interpretation of the Formation Image Log shows two faults and 160 fractures for Stage 10. The major fractures are oriented at N80°E along with the faults at N30°E orientation. Wilson et al., (2018) analyzed the formation image logs of the MIP-3H well and reported a present-day SH_{max} orientation of N57°E based on the orientation of induced fractures observed in the vertical pilot well. Given this orientation of current SHmax, the fractures and faults detected in Stage 10 are roughly at 23° east of SH_{max} and 27° north of the SH_{max}, respectively. As suggested by Fisher and Guest (2011) tensile failure could happen for pre-existing natural fractures with orientation of less than or equal 10° relative to the SH_{max} direction. Natural fractures and faults that are oriented at higher angels to SH_{max} most likely experience shear failure when subjected to increased pore pressure condition (Das and Zoback, 2013b). This suggests that the suboptimal faults and fractures of Stage 10 are more prone to shear slip rather than tensile deformation during stimulation. Also, the high clay content of the Marcellus Shale would facilitate a slow shear slip on the preexisting faults and fractures during the stimulation of the associated stage. We inspect the recorded geophone data from downhole array to identify potential LPLD events during the hydraulic fracturing of Stage 10 and compared them with DAS spectrogram.

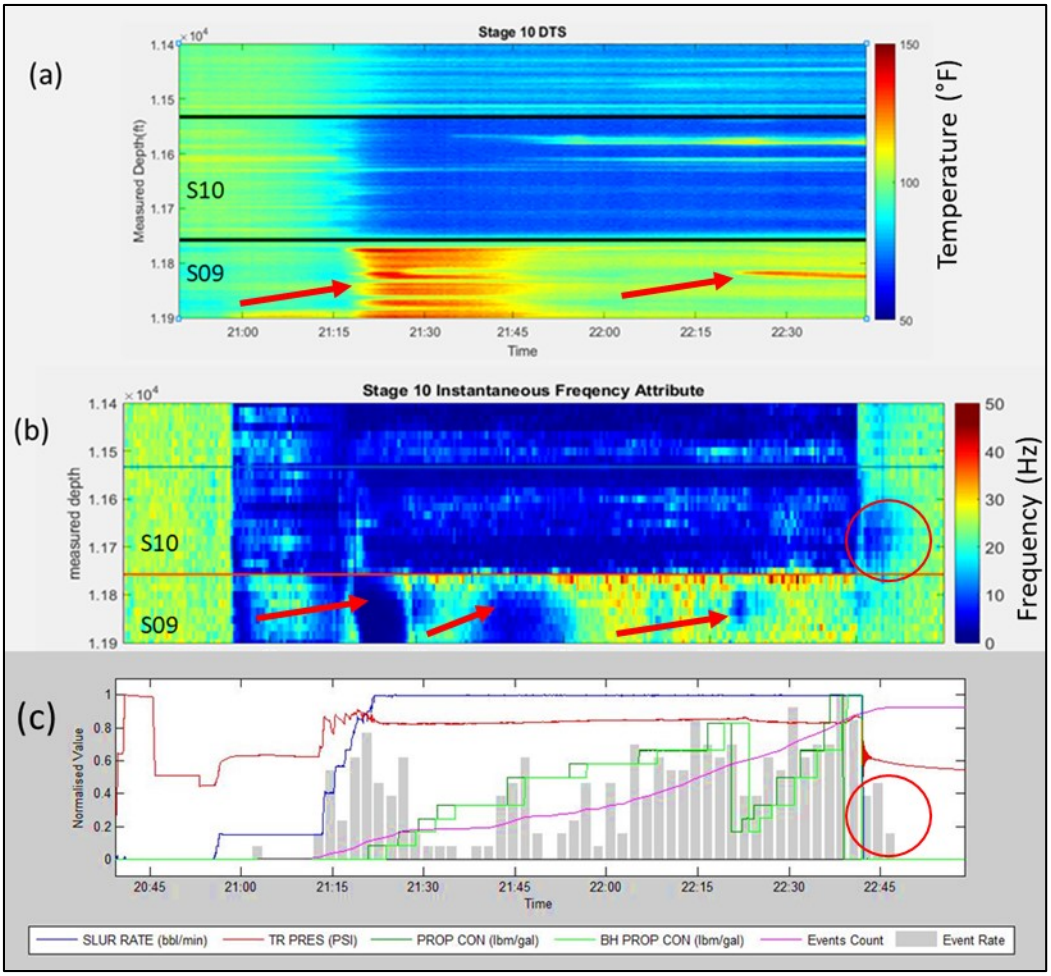

Figure 3: a) The DTS data for stimulation of stage 10. The warmer color (arrows) shows higher temperature in stage 9. b) Low frequency time intervals observed in stage 9 (S09) during stimulation of stage 10. Note the leak-off period marked by a circle. c) Normalized pumping data of stage 10 stimulation are shown. The bar histogram shows the microseismic events recorded in the borehole geophones of the monitoring well. The circle shows the microseismic activities during the leakoff period.

The spectrum of the microseismic data (Figure 4) was computed for a data set consisting of the sum of the z-component response for all 12 geophones in the monitoring well array. The 0.0005 second sample interval equals that of the DAS data. Relatively high amplitude low frequency response is observed in two time intervals that extend from approximately 2500s to 3200s and 6900s to 7300. The first low frequency interval around 3000s is simultaneous with formation breakdown. These seismic energies are within low frequency interval (10-80HZ) that continues for extended time duration of 200-300 seconds (Figure 4). We evaluated the spectrogram of X and Y geophone components to find out low frequency intervals. However, the low frequency time intervals are more significant in the z-component of geophones.

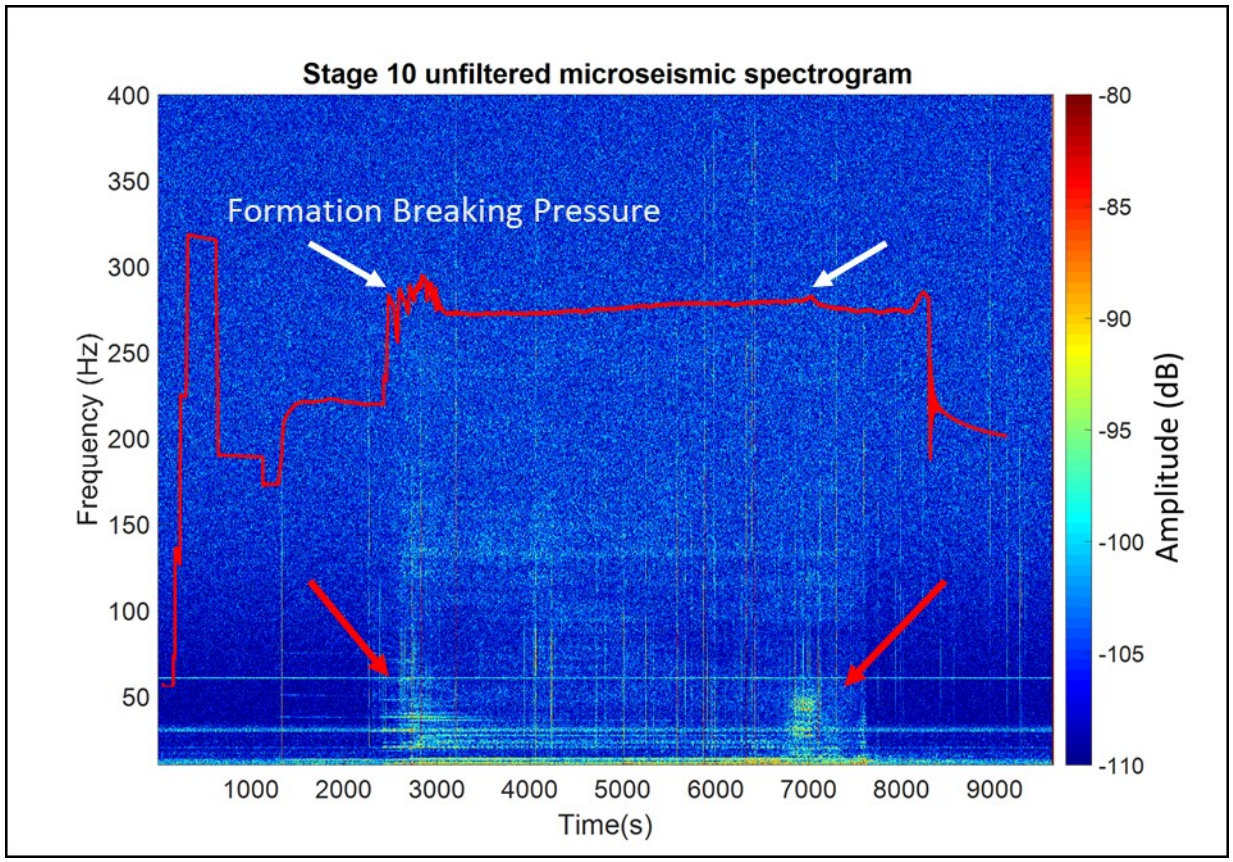

Figure 4: The raw unfiltered microseismic spectrogram of the Stage 10. The red curve shows the normalized treatment pressure. Intervals of low frequency time intervals are visible as the treatment pressure increased (white arrows).

The z-componet of geophones data are bandpassed filtered to 10-80 Hz (Figure 5). High amplitude intervals are observed around 3000s and 7000s. The feature around 3000s is more felt by deeper geophones. In contrast, the 7000sec feature exists in most geophones.

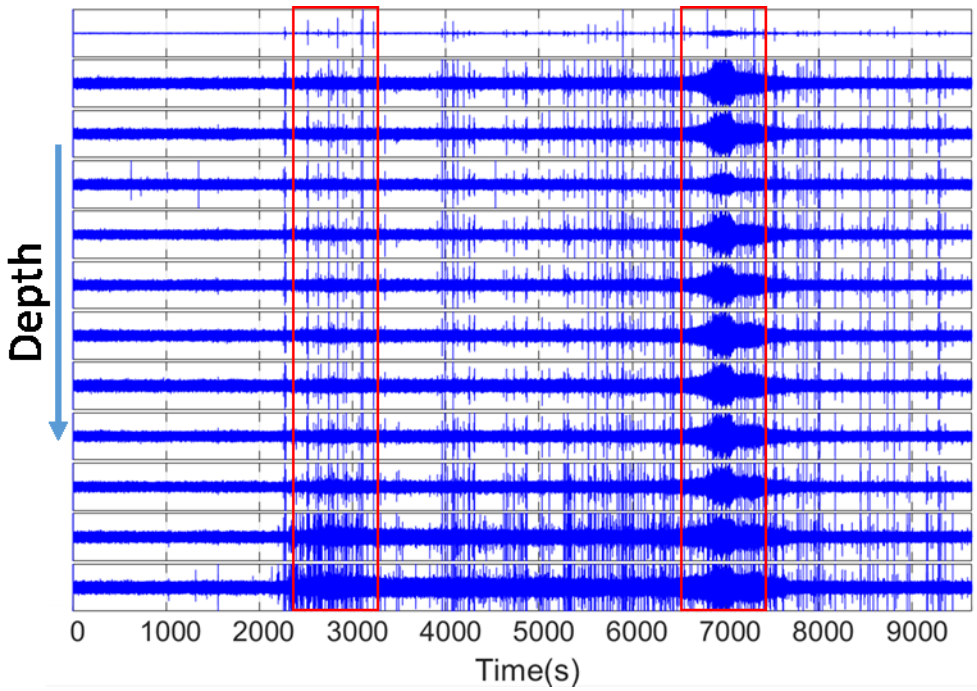

Figure 5: The 10-80Hz filtered z-components of 12 downhole geophones are shown. Note the features around 3000s and 7000sec.

We evaluated a DAS channel at 11801.49ft, which is in the top of the Stage 9, against the sum of the z-components amplitudes of the borehole geophones recorded during the stimulation of the Stage 10 (Figure 6). The DAS data are lowpass filtered at an 80Hz frequency. The filtered spectrogram of DAS channel from Stage 9 reveals low frequency intervals that are interpreted to correspond to LPLDs from the geophone data. The slow slip shear on pre-existing faults and fractures in Stage 10 and 9 is interpreted to be the most likely cause of the interpreted LPLDs in downhole geophone data. The LPLD events are concurrent with the temperature rise in the Stage 9, this could suggest a flow communication through re-activated faults and fractures that undergo slow slip shear during hydraulic fracturing. There are other low frequency time intervals in DAS data that are not visible on spectrogram of geophone data. However, the question of whether these low frequency time intervals are due to LPLD event remains unresolved (Figure 6a).

The persistent very long-duration low frequency (10 to 30Hz) tremor between 2500 and 8000 seconds on the geophones spectrogram appears to be related to coupling of pumping induced vibrations into the subsurface (Figure 6b). Eaton et al., (2013) noticed similar low frequency features that persist for an entire stage stimulation. DAS and Zoback (2013a and b) also mentioned that transport of the treatment fluids inside the pipe might induce oscillations in the formation and cause LPLD like frequency time intervals on microseismic spectrogram.

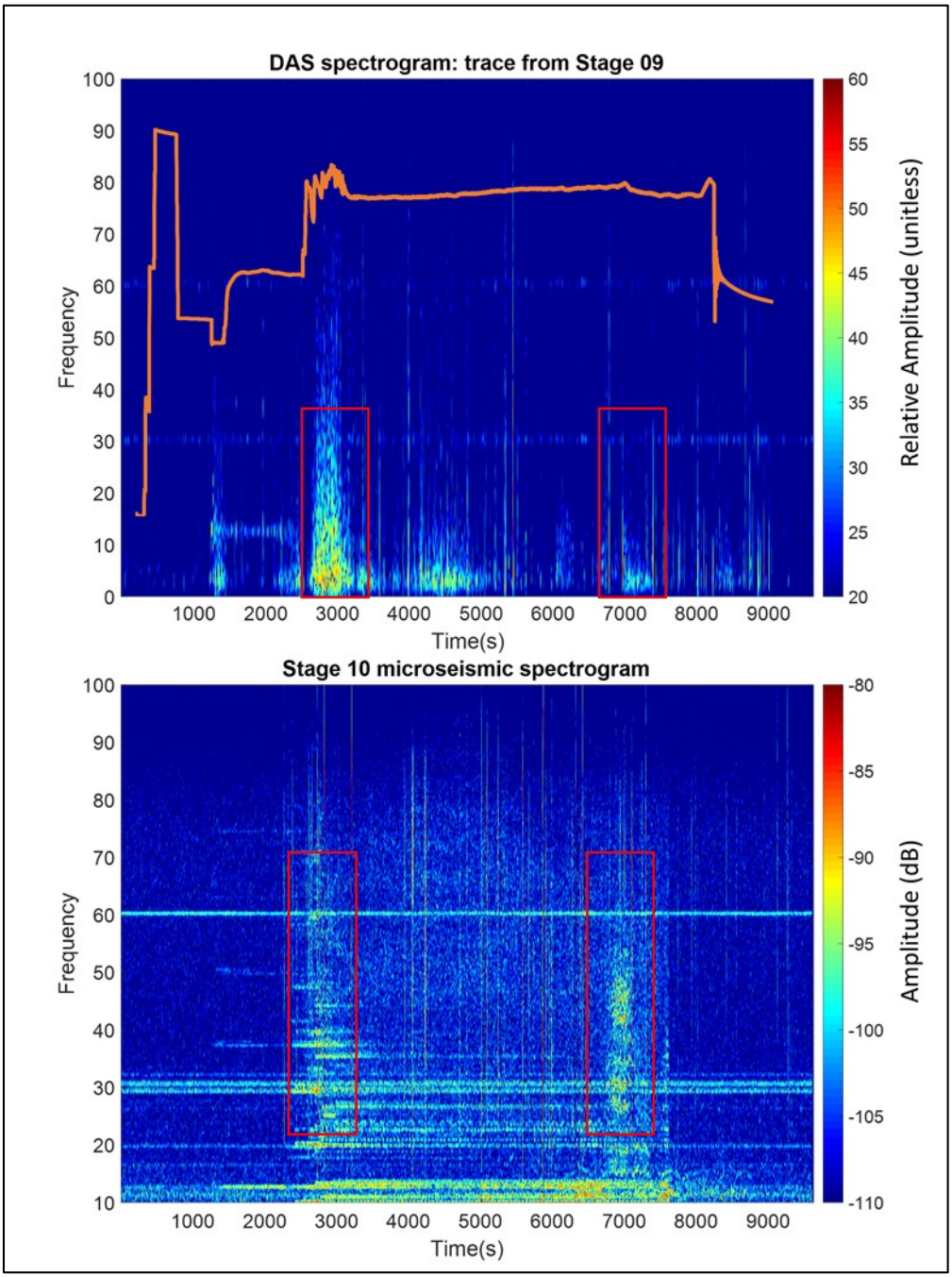

Figure 6: a) Stage 10 stimulation cause low frequency time intervals in DAS trace#371, which is in Stage 9. The orange curve shows the treatment pressure b) Spectrogram of sum of the z-components of Stage 10 microseismic. The low frequency strips around 10Hz, 30Hz and 60Hz appear to be noises picked by the interrogator at the surface.

The spectrogram of all 80Hz lowpass filtered DAS data at 2950s and 7000s shows that low frequency signals are not observed in all channels and is more concentrated at the bottom of the stage 10 (Figure 7). This excludes the possibility that the low frequency interval could be a direct interference of DAS interrogator with surface waves due to pumping machinery at the wellsite.

The filtered DAS traces from middle of stages 13 to 7 show that both features at 3000s and7000s are not instrumentation noise and cannot be observed in all channels (Figure 8).

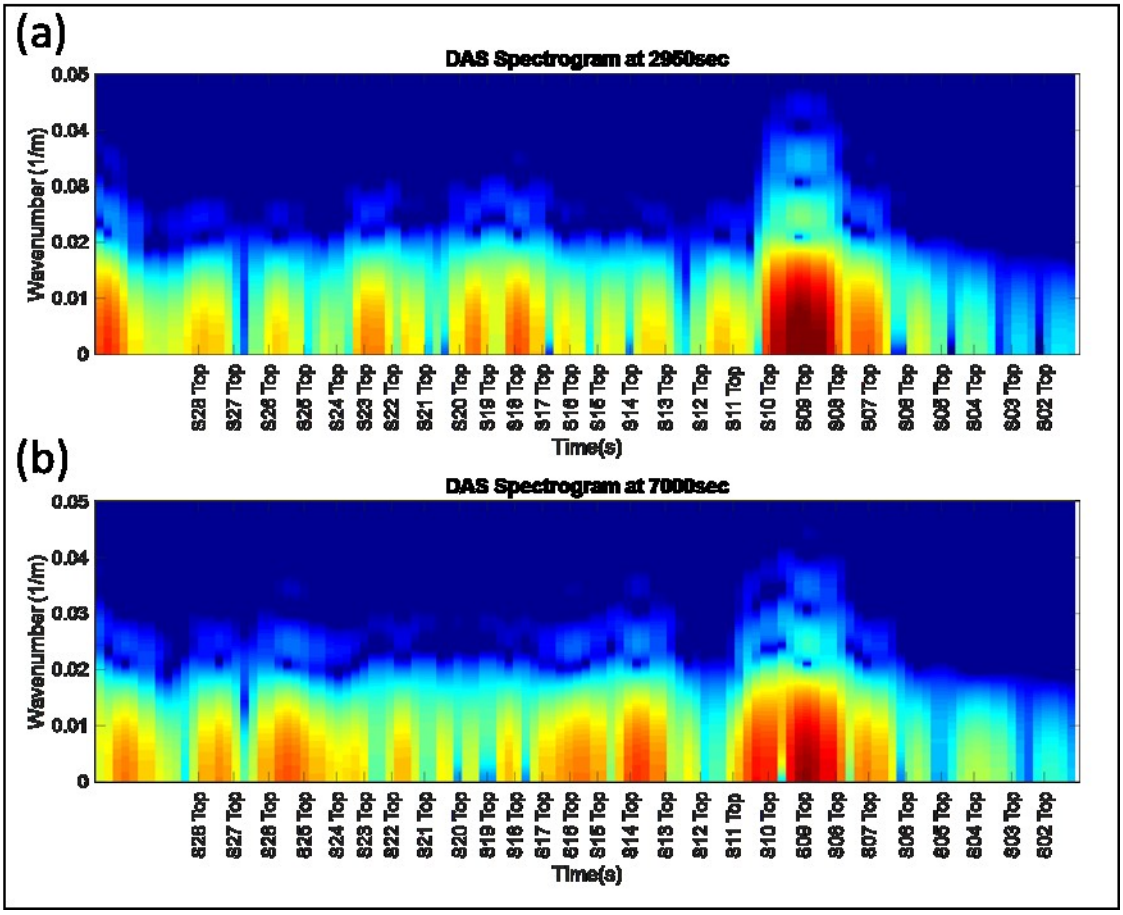

Figure 7: a) The spectrogram of DAS signal at 2000s for all the DAS channels. b) The spectrogram of DAS signal at 7000s for all DAS channels.

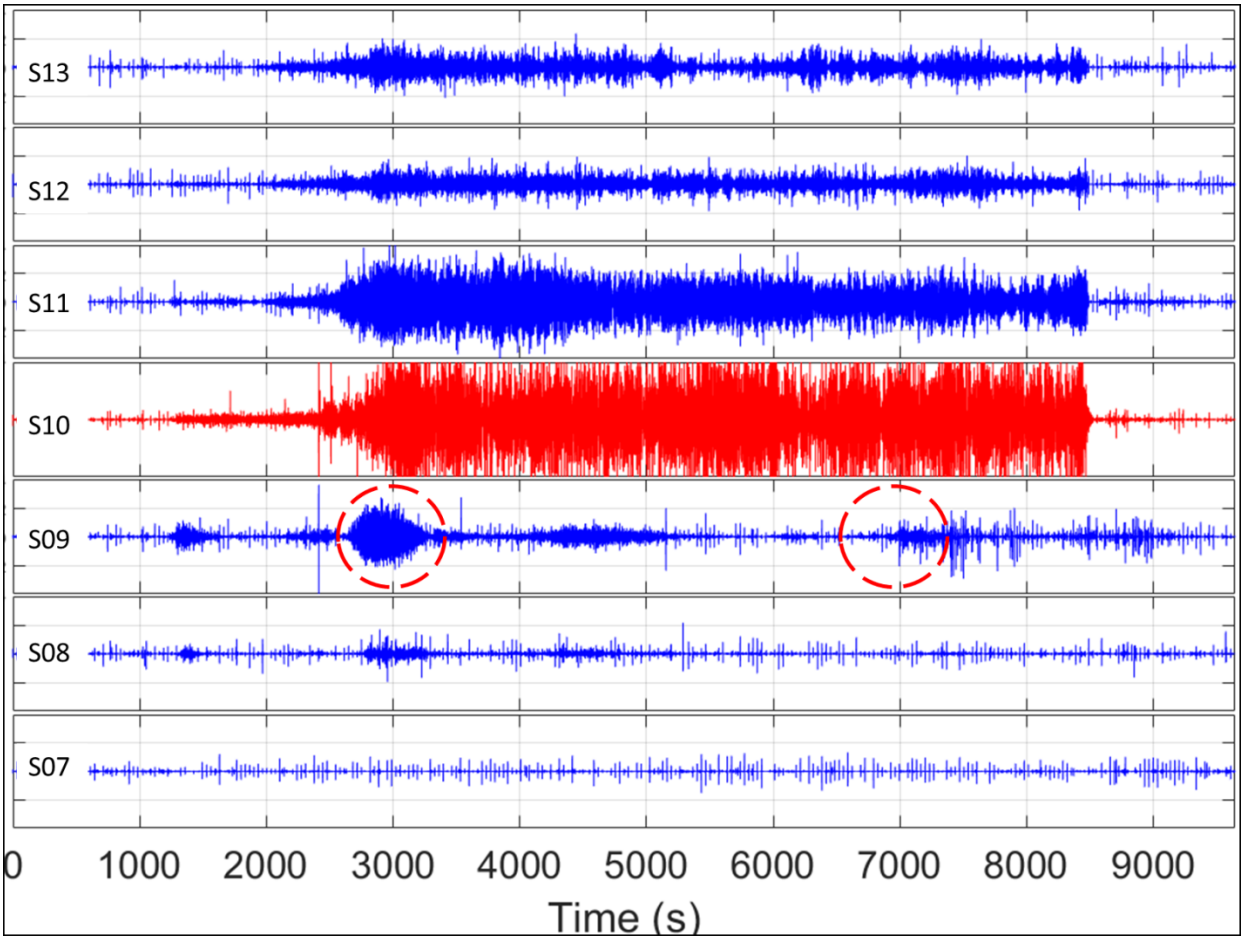

Figure 8: The filtered DAS signals from middle of stages 13 to 7 are shown. Note that stage 7,8, and 9 are separated from the stage 10 (stimulated stage) and above by a plug.

The interpreted LPLD events from borehole geophones in this study have similar frequency content to LPLDs from Barnet Shale interpreted by Das and Zoback (2013a) in the range of 10-80 Hz. Eaton et al., (2013) proposed that fracture network complexity could affect the dominant frequency content of LPLD events. They interpreted LPLD events from Montney Shale (British Columbia) with frequencies less than 10 Hz, while previous LPLD events reported by Das and Zoback (2013a and b) in the Barnett Shale (Texas) were found to have dominant energy in the frequency range of 10-80Hz. The lower observed frequency of LPLD events in Montney Formation, compared to the Barnett Shale, was attributed to less complex fracture network in the Montney Formation (A single fracture set). Fisher et al. (2005) categorized Barnett Shale as a formation with a very complex fracture network consists of two intersecting fracture set: a set in NE-SW and another set in NW-SE direction. Formation image logs of the MIP-3H vertical well reveal the presence of two fracture sets with orientations of N87°E and N57°E while those observed in the horizontal well fell mostly in a single set with average orientation of N79°E (Wilson et al., 2018). This suggest that fracture networks in the Marcellus Shale are similar in complexity to the Barnett Shale fracture network and likely responsible to generate higher frequency LPLD events.

A closer look at the features around 3000s on geophone data reveals that s-waves can be observed in all the geophones while clear p and s-arrivals can be seen on unfiltered data (Figure

9). The high frequency DAS data from the stage 9 at the same time interval does not show clear p and s-wave (Figure 10). However, a moveout can be observed later than geophone data. The DAS data in this study has gauge length of 64ft and it lacks acoustic phase coherence. Thus, the measured strain for each trace is the integration of phase shift of the backscattered signals over the a 64ft length of the fiber. This makes the current fiber-optic system not able to be as sensitive as geophone data. The 7000s feature is also can be observed in filtered and unfiltered geophone data (Figure 11). The DAS does not show a clear a p or s-wave arivals (Figure 12).

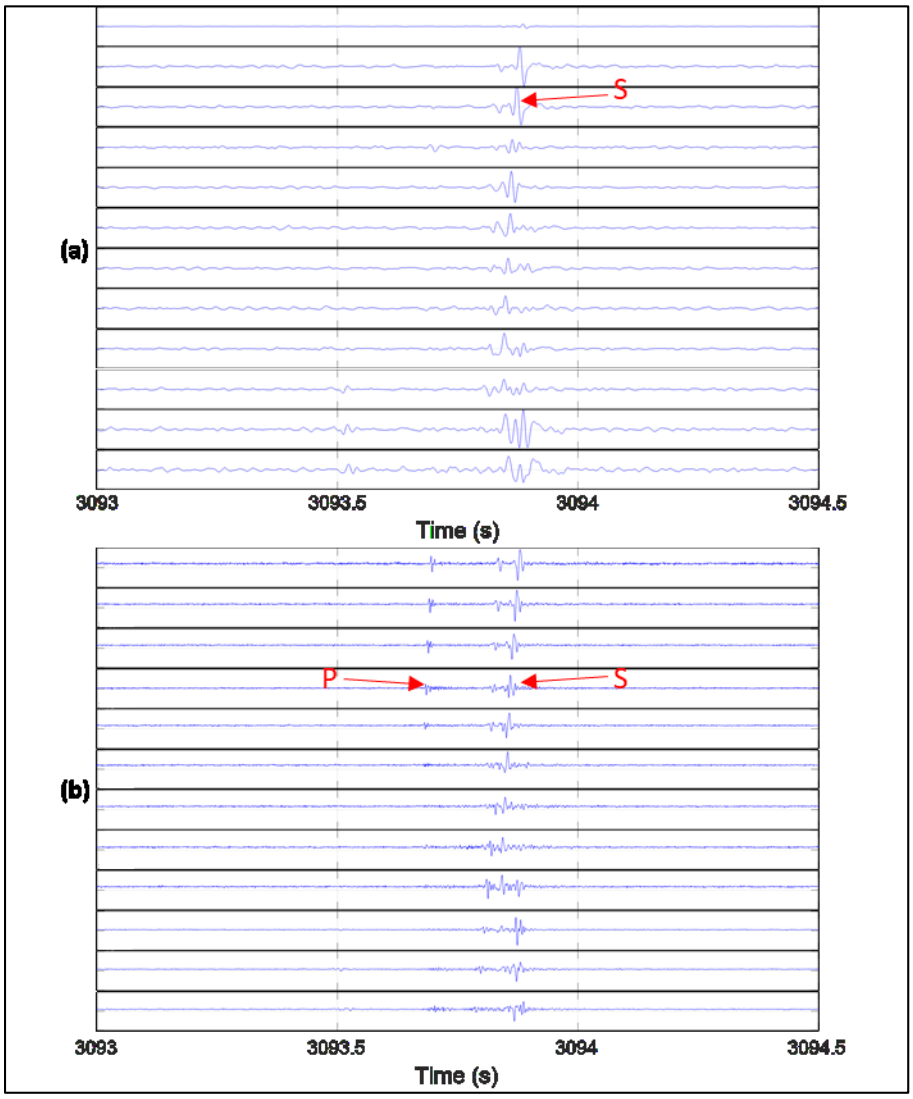

Figure 9: a) The filtered geophone data within the interpreted LPLD at 3000s. S-waves are evident in all channels. b) Raw geophone data within the interpreted LPLD at 7000s.

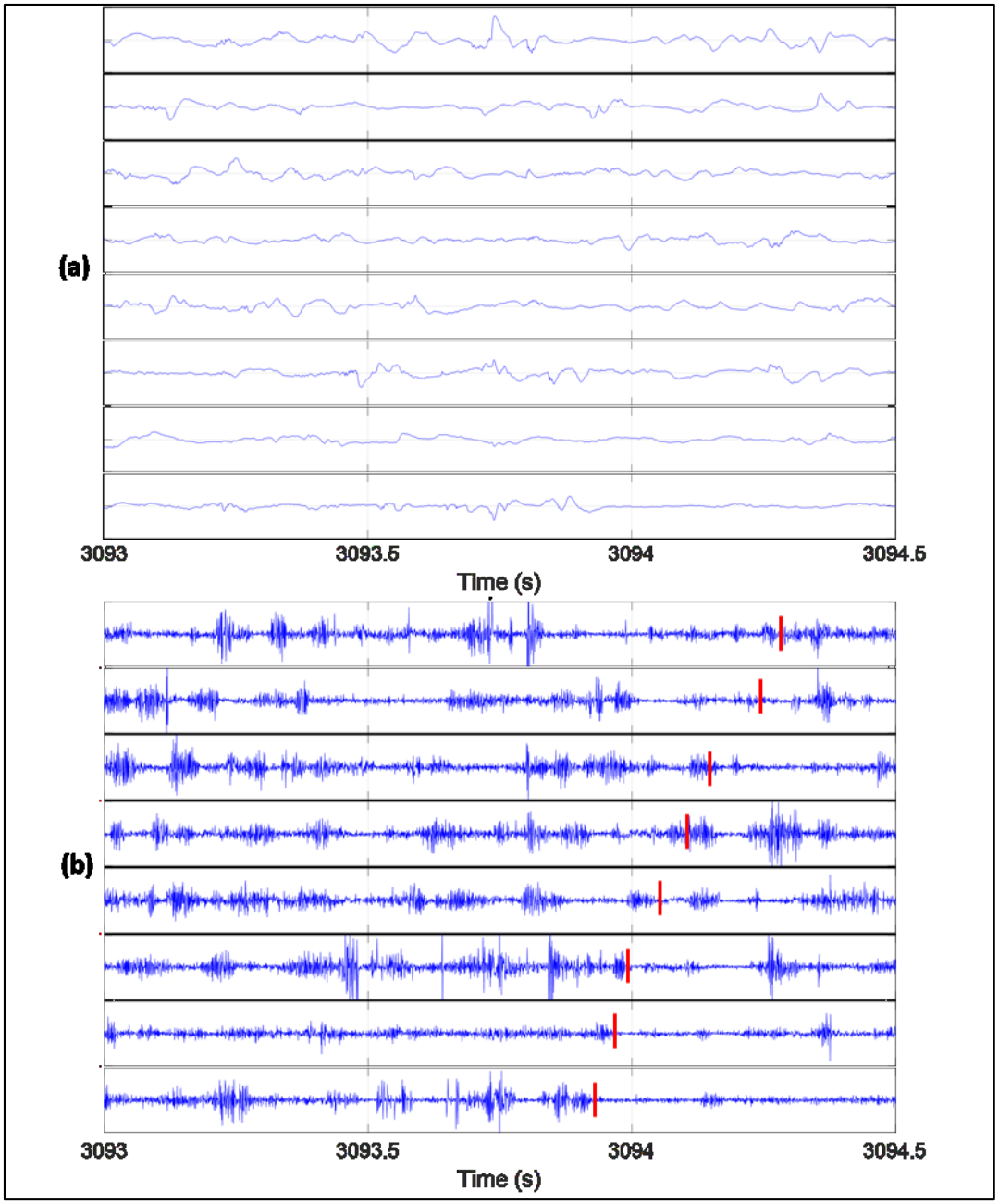

Figure 10: a) The filtered DAS data in the stage 9 while stimulating stage 10 does not show s- or p-wave arrivals. b) The high frequency DAS data. A moveout can be observed but no p- or s-wave arrivals.

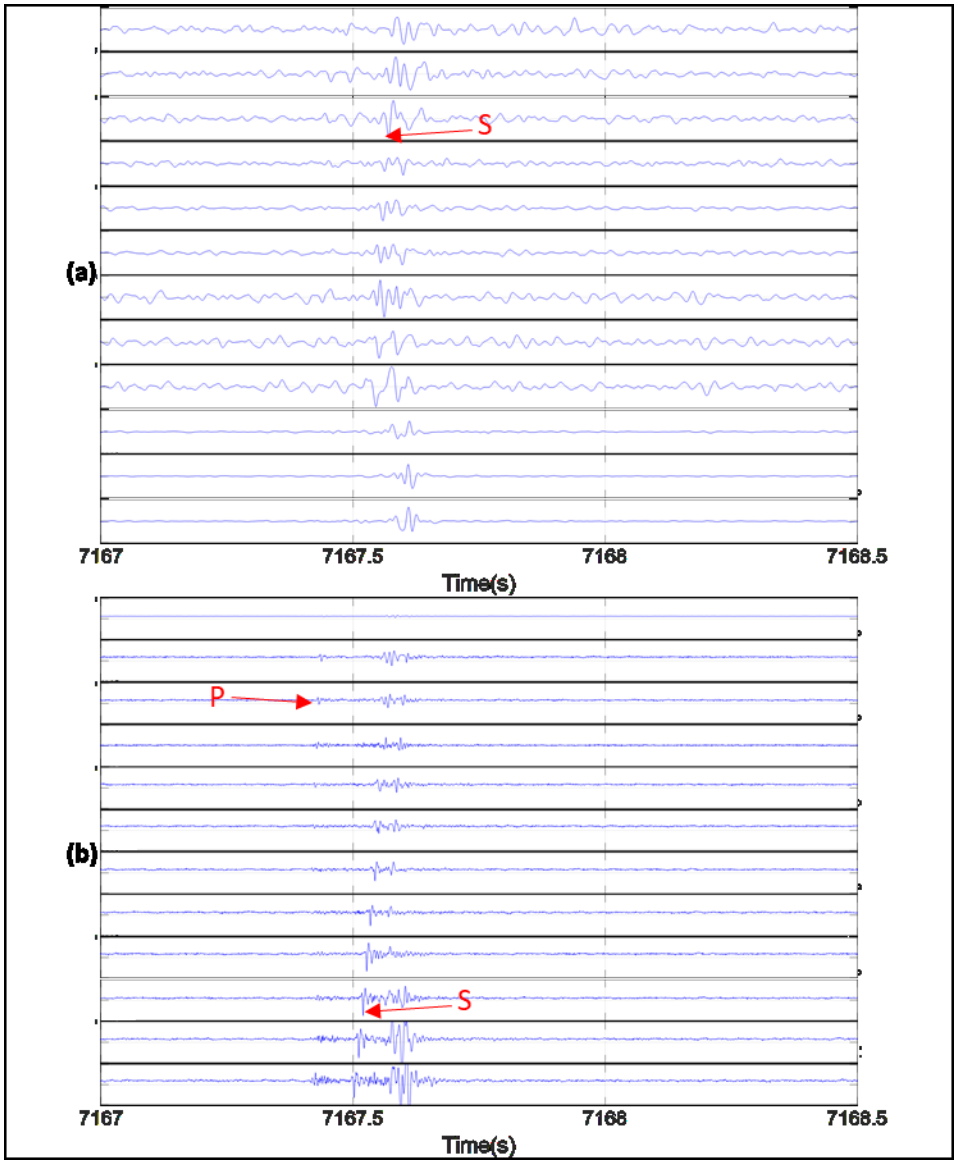

Figure 11: The filtered geophone data within the interpreted LPLD around 3000s. S-waves are evident in all channels. b) Raw geophone data within the interpreted LPLD around 7000s.

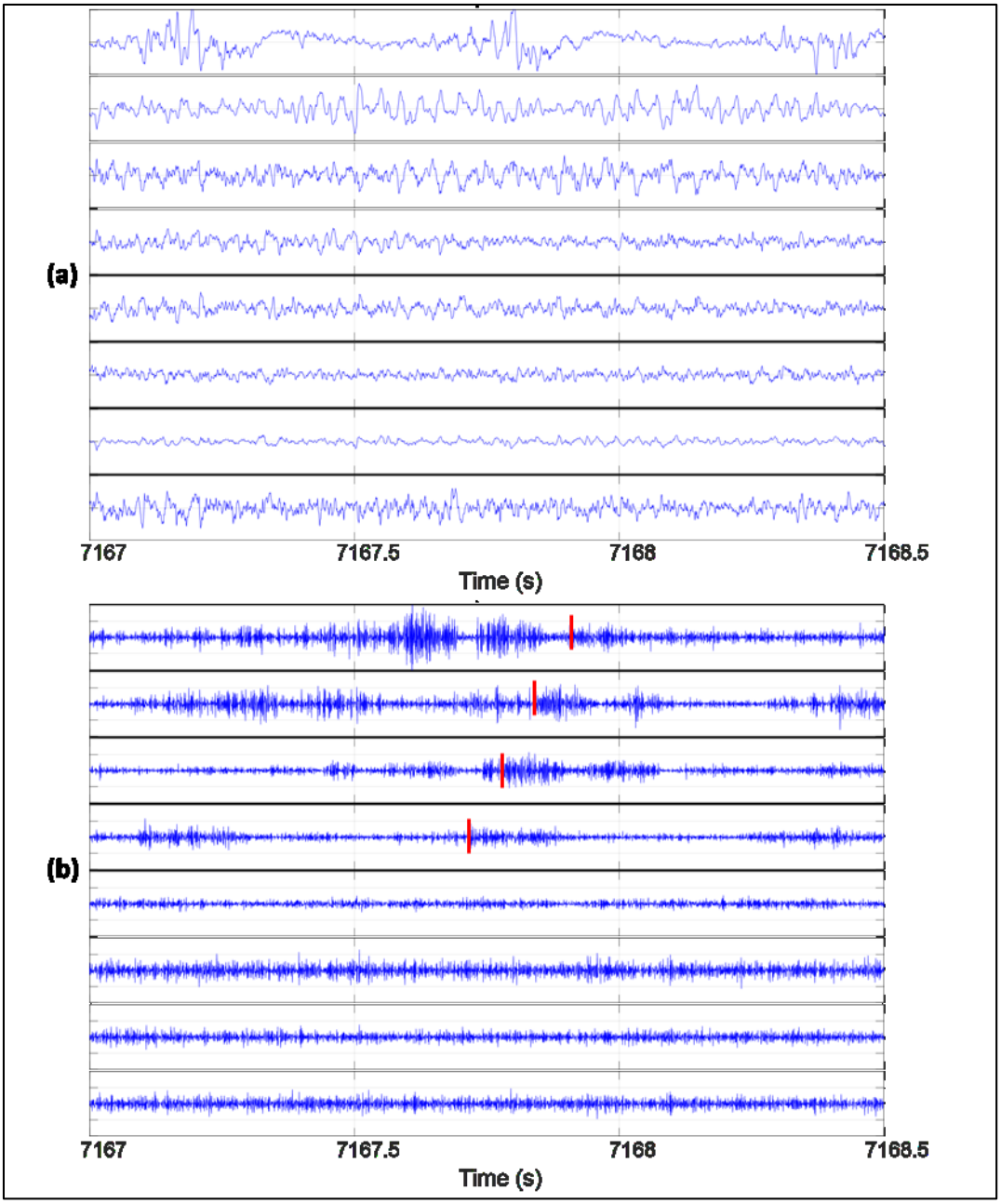

Figure 12: a) The filtered DAS data in the stage 9 does not show s- or p-wave arrivals. b) The high frequency DAS data. A moveout can be observed but no p- or s-wave arrivals.

CONCLUSIONS

Study of the spectrogram of the DAS and downhole geophone data of the Stage 10 brings the following concluding remarks:

- The distributed temperature sensing data shows a warming effect in the stage 9 while stimulating stage 10 and it temporally coincide with the LPLD events in the downhole seismic and DAS spectrogram. It likely suggests hydraulic connections between two consecutive stages, possibly due to the reactivation of preexisting fractures of suboptimal orientation that triggered LPLD events.
- Both LPLD events around 3000s and 7000s on DAS data are associated with increased microseismic activities. However, p- or s-wave arrivals could not be identified on the DAS data. This is due to the fact that DAS system in our study did not record full waveform and only recorded DAS amplitude.
- The two LPLDs on DAS data are not observed in all DAS traces. This rules out the possibility that surface machinery interfered directly with the interrogator.
- Regional earthquakes are very unlikely to have any effect on the DTS data. Thus, LPLD events observed in the current study in the DAS, microseismic, and DTS are most likely related to local deformation in the reservoir during hydraulic fracturing and not an overprint of regional earthquake in the distant area.
- Stage 10 have faults and pre-existing fractures, which are not optimally aligned with the present-day maximum horizontal stress for tensile failure. Hence, slow shear slip of suboptimal fractures during increased fluid activity and pore pressure change could be a major deformation mechanism.
- Microseismic events are observed in both LPLD events. The corresponding DAS data in the same time windows do not show a clear p- or s- wave arrivals.

ACKNOWLEDGMENTS

This research is funded through the U.S.DOE National Energy Technology Lab part of their Marcellus Shale Energy and Environmental Laboratory (MSEEL) (DOE Award No.: DE-FE0024297). We appreciate the Northeast Natural Energy LLC. For providing data and technical support.

REFERENCES

Aki, K. T., 1969, Analysis of the seismic coda of local earthquakes as scattered waves: Journal of Geophysical Research, **74**, 615–631.

Aki, K. T., and B. Chouet, 1975, Origin of the coda waves: Source attenuation and scattering effects: Journal of Geophysical Research, **80**, 3322– 3342.

Amini, S., Kavousi, P., and Timothy R. Carr, 2017, Application of Fiber-optic Temperature Data Analysis in Hydraulic Fracturing Evaluation--A Case Study in Marcellus Shale: Unconventional Resources Technology Conference, URTEC, Paper 2686732 .

Boroumand, N., and D. W. Eaton, 2012, Comparing energy calculations-hydraulic fracturing and microseismic monitoring: 74th Annual International Conference and Exhibition, EAGE, Extended Abstracts, EUROPEC 2012, https://doi.org/10.3997/2214-4609.20148187.

Caffagni, E., D. Eaton, M. van der Baan, and J. P. Jones, 2015, Regional seismicity: A potential pitfall for identification of long-period long-duration events: Geophysics, **80**, no. 1, A1–A5.

Das, I., and M. D. Zoback, 2011, Long-period, long-duration seismic events during hydraulic fracture stimulation of a shale gas reservoir: The Leading Edge, **30**, 778–786.

Das, I., and M. D. Zoback, 2013a, Long-period, long-duration seismic events during hydraulic stimulation of shale and tight-gas reservoirs — Part 1: Waveform characteristics: Geophysics, **78**, no. 6, KS97– KS108.

Das, I., and M. D. Zoback, 2013b, Long-period long-duration seismic events during hydraulic stimulation of shale and tight-gas reservoirs —Part 2: Location and mechanisms: Geophysics, **78**, no.6, KS109– KS117.

Eaton, D., van der Baan, M., Tary, J. B., Birkelo, B., Spriggs, N., Cutten, S., & Pike, K. , 2013, Broadband microseismic observations from a Montney hydraulic fracture treatment, northeastern BC, Canada: CSEG Recorder, **38**(3), 44-53.

Fisher, M. K., Wright, C. A., Davidson, B. M., Goodwin, A. K., Fielder, E. O., Buckler, W. S., and Steinsberger, N. P ., 2005, Integrating fracture-mapping technologies to improve stimulations in the Barnett Shale: SPE production & Facilities, **20**(2), 85-93..

Fisher, T., and Guest, A., 2011, Shear and tensile earthquakes caused by fluid injection: Geophysical Research Letters, **38**, L05307.

Ghahfarokhi, P. K., Carr, T., Song, L., Shukla, P., & Pankaj, P., 2018, Seismic Attributes Application for the Distributed Acoustic Sensing Data for the Marcellus Shale: New Insights to Cross-Stage Flow Communication. SPE Hydraulic Fracturing Technology Conference and Exhibition. Society of Petroleum Engineers, Paper 189888.

Glasbergen, G., Yeager, V.J., Reyes, R.P. and Everett, D.M., 2010, Fluid-diversion monitoring: the key to treatment optimization: SPE Production & Operations, **25**(03), 262-274.

Holley, E. and Kalia, N., 2015, Fiber-optic Monitoring: Stimulation Results from Unconventional Reservoirs: Unconventional Resources Technology Conference (URTEC), Paper 2151906.

Jin, G. and Roy, B., 2017, Hydraulic-fracture geometry characterization using low-frequency DAS signal: The Leading Edge, **36**(12), 975-980.

Karaman, O.S., Kutlik, R.L. and Kluth, E.L., 1996, A field trial to test fiber optic sensors for downhole temperature and pressure measurements, West Coalinga Field, California: SPE Western Regional Meeting, Paper 35685.

Karrenbach, M., Ridge, A., Cole, S., Boone, K., Kahn, D., Rich, J., Silver, K. and Langton, D., 2017, DAS microseismic monitoring and integration with strain measurements in hydraulic fracture profiling: Unconventional Resources Technology Conference, URTEC, Paper 2670716.

Kavousi, P., Carr, T., Wilson, T., Amini, S., Wilson, C., Thomas, M., … Hewitt, J., 2017, Correlating distributed acoustic sensing (DAS) to natural fracture intensity for the Marcellus Shale: SEG Technical Program Expanded Abstracts 2017, 5386-5390.

Kwietniak, A., 2015, Detection of the long period long duration (LPLD) events in time- and frequency-domain: Acta Geophysica, **63**, 201–213.

Kumar, A., Zorn, E.V., Hammack, R. and Harbert, W., 2017a, Seismic Monitoring of Hydraulic Fracturing Activity at the Marcellus Shale Energy and Environment Laboratory (MSEEL) Site, West Virginia: Unconventional Resources Technology Conference, URTEC, Paper 2670481.

Kumar, A., Zorn, E., Hammack, R., & Harbert, W., 2017b. Long-period, long-duration seismicity observed during hydraulic fracturing of the Marcellus Shale in Greene County, Pennsylvania: The Leading Edge, **36**(7), 580-587.

Mitchell, C., J. Kurpan, and P. Snelling, 2013, Detecting long-period long-duration microseismic events during hydraulic fracturing in the Cline Shale Formation, West Texas: A case study: 83rd Annual International Meeting, SEG, Expanded Abstracts, 2233–2237.

Montgomery, C. T., and M. B. Smith, 2010, Hydraulic fracturing: History of an enduring technology: Journal of Petroleum Technology, **62**, 26-40.

Nadeau, R.M., and A. Guilhem, 2009, Nonvolcanic tremor evolution and the San Simeon and Parkfield, California, earthquakes: Science, **325**, 5937, 191-193.

Obara, K., 2002, Nonvolcanic deep tremor associated with subduction in southwest Japan: Science, **296** (5573), 1679-1681.

Olofsson, B. and Martinez, A., 2017, Validation of DAS data integrity against standard geophones—DAS field test at Aquistore site: The Leading Edge, **36**(12), 981-986.

Rahman, M., Zannitto, P.J., Reed, D.A. and Allan, M.E., 2011, Application of fiber-optic distributed temperature sensing technology for monitoring injection profile in Belridge Field, diatomite reservoir: SPE Digital Energy Conference and Exhibition, SPE, Paper 144116.

Rutledge J. T. Phillips W. S., 2003, Hydraulic stimulation of natural fractures as revealed by induced microearthquakes, Carthage Cotton Valley gas field, East Texas: Geophysics , **68**, 441–452.

Shelly, D. R., Beroza, G. C., Ide, S., & Nakamula, S., 2006, Low-frequency earthquakes in Shikoku, Japan, and their relationship to episodic tremor and slip: Nature, **442**(7099), 188.

Sicking, C., Vermilye, J., Geiser, P., Lacazette, A., & Thompson, L., 2012, Permeability field imaging from microseismic: SEG Annual Meeting. Society of Exploration Geophysicists.

Sierra, J.R., Kaura, J.D., Gualtieri, D., Glasbergen, G., Sarker, D. and Johnson, D., 2008, DTS monitoring of hydraulic fracturing: experiences and lessons learned: SPE Annual Technical Conference and Exhibition, Society of Petroleum Engineers, Paper 116182.

Tanimola, F. and Hill, D., 2009, Distributed fibre optic sensors for pipeline protection: Journal of Natural Gas Science and Engineering, **1**(4), pp.134-143.

Warpinski N. R. Wolhart S. L. Wright C. A., 2004, Analysis and prediction of microseismicity induced by hydraulic fracturing: Society of Petroleum Engineers Journal, **9**, 24–33.

Warpinski, N.R., Du, J. and Zimmer, U., 2012, Measurements of hydraulic-fracture-induced seismicity in gas shales: SPE Production & Operations, **27**(03), 240-252.

Webster, P., M. Molenaar, and C. Perkins, 2016, DAS microseismic: CSEG Recorder **41**(6): 38-39.

Wilson, T.,H., Hart, A.,K., and Pete Sullivan, 2016 , Interrelationships of Marcellus Shale gas production to frac-induced microseismicity, interpreted minor faults and fractures zones, and stimulated reservoir volume, Greene County, Pennsylvania: Interpretation, **4**(1), T15-T30.

Wilson, T. H., Carr, T., Carney, B. J., Yates, M., MacPhail, K., Morales, A.,... & Thomas, M., 2018, Marcellus Shale model stimulation tests and microseismic response yield insights into mechanical properties and the reservoir discrete fracture network: Interpretation, **6**(2), T231-T243.

Zecevic, M., Daniel, G., & Jurick, D., 2016, On the nature of long-period long-duration seismic events detected during hydraulic fracturing: Geophysics, **81**(3), KS113-KS121.

Zoback, M. D., A. Kohli, I. Das, and M. McClure, 2012, The importance of slow slip on faults during hydraulic fracturing stimulation of shale gas reservoirs: Americas Unconventional Resources Conference, SPE, Paper 155476.

Cost Status

Year 1

Start: 10/01/2014 End: 09/30/2017

Baseline Reporting Quarter

	Q1 (12/31/14)	Q2 (3/30/15)	Q3 (6/30/15)	Q4 (9/30/15)
Baseline Cost Plan	(From 424A, Sec. D)			
(from SF-424A)				
Federal Share	$549,000		$3,549,000	
Non-Federal Share	$0.00		$0.00	
Total Planned (Federal and Non-Federal)	$549,000		$3,549,000	
Cumulative Baseline Costs				
Actual Incurred Costs				
Federal Share	$0.00	$14,760.39	$237,451.36	$300,925.66
Non-Federal Share	$0.00	$0.00	$0.00	$0.00
Total Incurred Costs - Quarterly (Federal and Non-Federal)	$0.00	$14,760.39	$237,451.36	$300,925.66
Cumulative Incurred Costs	$0.00	$14,760.39	$252,211.75	$553,137.41
Uncosted				
Federal Share	$549,000	$534,239.61	$3,296,788.25	$2,995,862.59
Non-Federal Share	$0.00	$0.00	$2,814,930.00	$2,814,930.00
Total Uncosted - Quarterly (Federal and Non-Federal)	$549,000	$534,239.61	$6,111,718.25	$5,810,792.59

Start: 10/01/2014 End: 09/30/2017

Baseline Reporting Quarter

	Q5 (12/31/15)	Q6 (3/30/16)	Q7 (6/30/16)	Q8 (9/30/16)
Baseline Cost Plan	(From 424A, Sec. D)			
(from SF-424A)				
Federal Share	$6,247,367		$7,297,926	
Non-Federal Share	2,814,930		$4,342,480	
Total Planned (Federal and Non-Federal)	$9,062,297	$9,062,297.00	$11,640,406	
Cumulative Baseline Costs				
Actual Incurred Costs				
Federal Share	$577,065.91	$4,480,939.42	$845,967.23	$556,511.68
Non-Federal Share	$0.00	$2,189,863.30	$2,154,120.23	$0.00
Total Incurred Costs - Quarterly (Federal and Non-Federal)	$577,065.91	$6,670,802.72	$3,000,087.46	$556,551.68
Cumulative Incurred Costs	$1,130,203.32	$7,801,006.04	$10,637,732.23	$11,194,243.91
Uncosted				
Federal Share	$5,117,163.68	$636,224.26	$1,004,177.30	$447,665.62
Non-Federal Share	$2,814,930.00	$625,066.70	($1,503.53)	($1,503.53)
Total Uncosted - Quarterly (Federal and Non-Federal)	$2,418,796.68	$1,261,290.96	$1,002,673.77	$446,162.09

Start: 10/01/2014 End: 09/30/2017

Baseline Reporting Quarter	Q9 (12/31/16)	Q10 (3/30/17)	Q11 (6/30/17)	Q12 (9/30/17)
Baseline Cost Plan	(From 424A, Sec. D)			
(from SF-424A)				
Federal Share				$9,128,731
Non-Federal Share				$4,520,922
Total Planned (Federal and Non-Federal)				$13,649,653
Cumulative Baseline Costs				
Actual Incurred Costs				
Federal Share	$113,223.71	$196,266.36	$120,801.19	$1,147,988.73
Non-Federal Share	$0.00	$0.00	$0.00	$0.00
Total Incurred Costs - Quarterly (Federal and Non-Federal)	$113,223.71	$196,266.36	$120,801.19	$1,147,988.73
Cumulative Incurred Costs	$11,307,467.62	$11,503,733.98	$11,624535.17	$12,772,523.90
Uncosted				
Federal Share	$334,441.91	$138,175.55	$17,374.36	$700,190.63
Non-Federal Share	($1,503.53)	($1,503.53)	($1,503.53)	$176,938.47
Total Uncosted - Quarterly (Federal and Non-Federal)	$332,938.38	$136,672.02	$15,870.83	$877,129.10

Start: 10/01/2014 End: 09/30/2017

Baseline Reporting Quarter	Q13 (12/31/17)	Q14 (3/30/18)	Q15 (6/30/18)	Q15 (9/30/18)
Baseline Cost Plan	(From 424A, Sec. D)			
(from SF-424A)				
Federal Share				$11,794,054
Non-Federal Share				$5,222,242
Total Planned (Federal and Non-Federal)				$17,016,296.00
Cumulative Baseline Costs				
Actual Incurred Costs				
Federal Share	$112,075.89	$349,908.08	$182,207.84	$120,550.20
Non-Federal Share	$0.00	$31,500.23	$10,262.40	$4,338.00
Total Incurred Costs - Quarterly (Federal and Non-Federal)	$112,075.89	$381,408.31	$192,470.24	$124,888.20
Cumulative Incurred Costs	$12,884,599.79	$13,266,008.10	$13,458,478.34	$13,583,366.54
Uncosted				
Federal Share	$588,114.74	$238,206.66	$55,998.82	$2,600,771.62
Non-Federal Share	$176,938.47	$145,438.24	$135,175.84	$832,157.84
Total Uncosted - Quarterly (Federal and Non-Federal)	$765,053.21	$383,644.90	$191,174.66	$3,432,929.46

National Energy Technology Laboratory

626 Cochrans Mill Road
P.O. Box 10940
Pittsburgh, PA 15236-0940

3610 Collins Ferry Road
P.O. Box 880
Morgantown, WV 26507-0880

13131 Dairy Ashford Road, Suite 225
Sugar Land, TX 77478

1450 Queen Avenue SW
Albany, OR 97321-2198

Arctic Energy Office
420 L Street, Suite 305
Anchorage, AK 99501

Visit the NETL website at:
www.netl.doe.gov

Customer Service Line:
1-800-553-7681